ISBN 978-82-471-2429-1 (printed ver.)
ISBN 978-82-471-2430-7 (electronic ver.)
ISSN 1503-8181

Knut Vågsæther
Doctoral Thesis

Doctoral theses at NTNU, 2010:221

Knut Vågsæther

Modelling of gas explosions

NTNU
Norwegian University of
Science and Technology
Thesis for the degree of
philosophiae doctor
Telemark University College
Faculty of Technology

Doctoral theses at NTNU, 2010:221
NTNU

NTNU
Norwegian University of
Science and Technology

Høgskolen i Telemark

Knut Vågsæther

Modelling of gas explosions

Thesis for the degree of philosophiae doctor

Trondheim, December 2010

Norwegian University of
Science and Technology
Telemark University College
Faculty of Technology

NTNU
Norwegian University of Science and Technology

Thesis for the degree of philosophiae doctor

Telemark University College
Faculty of Technology

ISBN 978-82-471-2429-1 (printed ver.)
ISBN 978-82-471-2430-7 (electronic ver.)
ISSN 1503-8181

Doctoral Theses at NTNU, 2010:221

Printed by Tapir Uttrykk

Modelling of gas explosions

Knut Vågsæther

Thesis submitted for the degree of Philosophiae Doctor.

Porsgrunn, October 2010.

Faculty of Technology
Telemark University College
Norway

Faculty of Engineering Science & Technology
Norwegian University of Science and Technology
Norway

Preface

The work presented in this thesis was carried out at Telemark University College between 2001 and 2010. This LaTeX template is made by Vegeir Knudsen.

Acknowledgments

I would specially like to thank Professor Dag Bjerketvedt for excelent guiding and for all of our discussions on explosions and many other things. Also a special thank you to Andre V. Gaathaug. These people deserves a big thanks: Vegeir Knudsen, Ole Kristian Sommersel, Nina Bjerkebo Brovig, Kjetil Kristoffersen, Joachim Lundberg, Morten C. Melaaen, Randi S. Holta, Talleiv Skredtveit, all of my colleges at TUC, Geraint O. Thomas, Svein O. Christensen, and a special thanks to my parents. And of course Amalie and Mia.

Porsgrunn, June 2010
Knut Vågsæther

Abstract

The content of this thesis is a study of gas explosions in complex geometries and presentation and validation of a method for simulating flame acceleration and deflagration to detonation transition. The thesis includes a description of the mechanisms of flame acceleration and DDT that need to be modeled when simulating all stages of gas explosions. These mechanisms are flame acceleration due to instabilities that occur in fluid flow and reactive systems, shock propagation, deflagration to detonation transition and propagating detonations. The method presented uses the FLIC-scheme for solving the conservation equations of mass, momentum, energy, species and a turbulence model. A reaction rate model that includes both turbulent combustion rates and chemical kinetics to handle turbulence-flame interactions and reactions due to gas compression is designed for simulations of turbulent flames and detonations. Simulation results of gas explosions shows that the presented method can simulate different flame propagation regimes in channels with repeated obstacles like fast deflagrations, quasi-detonation and CJ-detonations. The simulations show the important effects seen in experiments like detonation initiation from shock focusing and flame acceleration from fluid instabilities. Blast waves from high explosives and fuel-air explosives are simulated and results are compared with experimental data. The comparison shows that the numerical solver capture the important waves and that the method can re-produce experimental pressures and impulses with satisfying accuracy. Different tests of the method show that the most significant error sources are numerical diffusion, accuracy of the simplified chemical kinetics and thermodynamic models. The most important points of further research to improve the accuracy of the method is addressed.

Nomenclature

Roman Symbols

a	Acceleration
A, B	JWL parameters
c	Sound speed
C_p	Heat capasity, constant pressure
C_v	Heat capacity, constant volume
C_ϵ, C_ν	Turbulent model constants
C_{cfl}	Courant Friedrich Levi coefficient
D	Detonation velocity
E	Energy
e	Internal energy
E_a	Activation energy
F, G	Flux of variable
H	Enthalpy
I	Integral length scale
J	Source term
K	Amplitude
k	Turbulent kinetic energy
l	Turbulent length scale
l_K	Kolmogorov length scale
N	Number of molecules
n	Wave number

p Pressure

Q A variable

q Change in formation enthalpy

R Gas constant

r Slope of variable

R_1, R_2 JWL parameters

S_L, S_T Burning velocity, laminar, turbulent

S_{ij} Strain rate

T Temperature

t Time

T_a Activation temperature

U Averaged velocity

u Instantaneous velocity

u' Velocity fluctuation

u'_K Kolmogorov velocity scale

X Mass diffusivity

x, y, z Spatial directions

Greek Symbols

α Radical reaction variable

$\bar{\Delta}$ Ratio of induction length to exothermal reaction zone length

β Exothermal reaction variable

Δ Difference

δ_L Laminar flame thickness

δ_{ij} Kronecker delta

$\dot{\omega}$ Reaction rate

ϵ_{ijk} Levi Civita symbol

γ Heat capacity ratio

$\hat{\rho}$	Relative density
λ	Thermal conductivity
μ	Dynamic viscosity
ν	Kinematic viscosity
Ω	JWL parameter
ω	Vorticity
ρ	Density
σ	Expansion ratio
τ	Induction time
τ_C	Chemical time scale
τ_I	Integral turbulent time scale
τ_K	Kolmogorov turbulent time scale

Subscripts

0	Initial
ad	Adiabatic
b	Burned
c	Convective
f	Formation
g	Limiter function
i, j, k	Directions
k	Kinetic
N	Composition
P	Products
R	Reactants
t	Turbulent
u	Unburned
vN	von Neumann state

Groups

η	Thomas number
Da	Damkohler number
Ka	Karlovitz number
Le	Lewis number
M	Mach number
Pr	Prandtl number
Re	Reynolds number

Contents

Chapter 1

Introduction

1.1 Background

Mathematical models are used to predict the loadings on structures from an explosion in pre-mixed fuel-oxidizer gas clouds and to better understand the mechanisms of an explosion. These models may be as simple as the TNO multi-energy method [*Van den Berg, 1985*] or complex CFD-methods where the details of the flame front and the effects of complex geometries on flame acceleration are simulated. Some commercial CFD-tools are designed for simulating gas explosions like FLACS [*FLACS web cite, n.d.*] which is designed for large scale explosions in congested geometries. For studying flame acceleration and DDT in lab scale it is possible to increase the accuracy of the methods by using smaller computational volumes to resolve more of the details in the flow and the flame. [*Gamezo et. al., 2007*] have studied flame acceleration and DDT in complex geometries with a global one-step reaction rate. In these studies the computational mesh size is much smaller than the flame thickness. To simulate lab scale experiments using mesh sizes much smaller than the flame thickness the number of control volumes become very large. An experiment of 1 m^3 and with flame thickness of 0.5 mm using 10 volumes over the flame thickness will give $8{\cdot}10^{12}$ control volumes. And even 10 volumes over the flame thickness is coarse if you want to resolve the flame front. The most popular method for simulating flow in large computational domains is to use larger control volumes and model the small scale effects. In CFD the two most common methods for modelling sub-mesh details are RANS-methods (Reynolds Averaged Navier-Stokes) and LES (Large Eddy Simulation) where averaged equations are solved and a turbulence model accounts for the small scale effects.

In gas explosions flame-flow field interactions produce positive feedback where the flame accelerates the surrounding fluid and fluid instabilities and flow-geometry interactions increase reaction rates. A box diagram of the process of flame acceleration up to a detonation is shown in figure 1.1. The flame propagates as either a deflagration or a detonation. A modelling method need to be able to simulate the different propagation mechanisms of deflagrations and detonations when solving averaged equations to simulate flame acceleration and DDT. In deflagrations transport processes like diffusion and radiation as well as turbulent transport of mass and heat play an important role of transporting radicals to and from the reaction zone and heat to the reactants from the reaction

front. In detonations shock waves compress the reactants to ignition and reactions feed the shock. A reaction model that is going to simulate these mechanisms must include turbulence-flame interactions and temperature dependencies of the reaction rate. A numerical method that is going to solve these models has to be able to capture shock waves and turbulence production and dissipation.

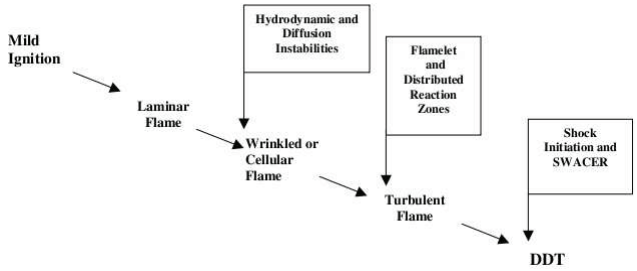

Figure 1.1: Process of flame acceleration to DDT, [*SOAR, 2000*].

1.2 Industrial accidents

Middletown, 2010

In a natural gas power plant in Middletown, Connecticut, USA a large explosion killed six people and injured at least 50 on February 7, 2010. The explosion was caused by ignition of a gas cloud inside the plant. High pressure natural gas was used to blow clean new pipes and was vented inside the plant. About 11 000 Sm^3 [*CSB Don Holmstrom, 2010*] was released and formed a flammable cloud. The ignition source is not yet found but there was some construction work in the area which might have ignited the mixture. The area in which the gas release occurred was inside a building and contained process equipment that increased burning rates causing pressure build-up.

Buncefield, 2005

On December 11, 2005 an explosion followed by a fire occurred at a fuel depot in Buncefield England, [Buncefield report Vol. 1, 2008]. A storage tank was over filled by gasoline and the liquid fuel started to flow over the top of the tank. About 300 tonnes of gasoline escaped and evaporated butane and droplets from less volatile components formed a combustible cloud. The cloud was ignited and a strong explosion lead to destruction of buildings and cars in the area. There are speculations that a lane of trees accelerated the flame up to a detonation. There was no fatalities but 43 people got injured.

Herøya, 1997

A 0.8 m pipe for transport of CO_2 exploded April 17, 1997 at Herøya in Porsgrunn, Norway. The pipe was under maintenance but hydrogen leaked into the pipe from the ammonia plant to which it was connected. Almost 1 km of the pipe ruptured but there were no injuries only structural damage. There are indications that the flame propagating in the pipe experienced DDT and failure several times, [*Pande and Tonheim, 2001*].

1.3 Problem description

The scope of this work is to model deflagration, detonation and transition from deflagration to detonation (DDT) in complex geometries with CFD. Examples of explosions in typical lab-scale geometries are shown in figure 1.2 where the flame propagates in a channel with repeated obstacles or in a pipe with one obstacle.

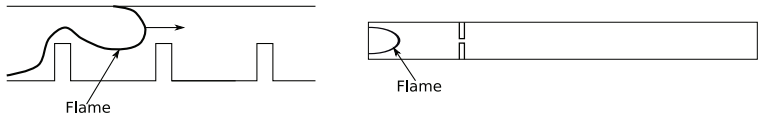

Figure 1.2: Examples of flame propagation in geometries discussed in this thesis. Left: Channel with repeating obstacles. Right: Pipe with one obstacle.

- The main focus in this work is to create a reaction rate model for simulating deflagrations and detonations. The model must handle both explosion regimes to be able to simulate transition between deflagrations and detonations as DDT or failure.
- The reaction model is going to be tested by comparing simulations to experimental and analytical data.
- The most important factor in flame acceleration is the feedback between flame and gas flow and the numerical method must handle compressible effects, like shock waves, as well as having a higher order accuracy for smooth solutions. The chosen numerical solver is going to be validated by comparing non-reactive simulations with experimental and analytical data.
- The models for simulating gas explosions are the conservation equations of mass, momentum, energy and species, equations 1.1 to 1.4. These equations are going to be solved with a computational mesh larger than the flame thickness and a suited turbulence model is going to be included in the model.

Table 1.1 shows a summary of the different simulation results shown in this thesis.

$$\frac{\partial \rho}{\partial t} + \frac{\partial}{\partial x_i}\left(\rho u_i\right) = 0 \tag{1.1}$$

$$\frac{\partial \rho u_i}{\partial t} + \frac{\partial}{\partial x_j}\left(\rho u_j u_i\right) = -\frac{\partial p}{\partial x_i} + \frac{\partial}{\partial x_j}\left(\mu \frac{\partial u_i}{\partial x_j}\right) \tag{1.2}$$

$$\frac{\partial \rho E}{\partial t} + \frac{\partial}{\partial x_i}\left(\rho u_i E\right) = -\frac{\partial}{\partial x_i}\left(p u_i\right) + \frac{\partial}{\partial x_i}\left(\lambda \frac{\partial T}{\partial x_i}\right) \tag{1.3}$$

$$\frac{\partial \rho Y_n}{\partial t} + \frac{\partial}{\partial x_i}\left(\rho u_i Y_n\right) = \frac{\partial}{\partial x_i}\left(\rho D_n \frac{\partial Y_n}{\partial x_i}\right) + \dot{\omega}_n \tag{1.4}$$

1.4 Thesis outline

- Chapter 2: A summary of the important phases of flame acceleration and the process of DDT and detonations and explanations of the different types of instabilities that influence these processes.
- Chapter 3: The method used for simulating gas explosions and blast waves in this thesis.
- Chapter 4: Simulations of basic tests of the numerical scheme and models and simulations of blast from high explosives.
- Chapter 5: Simulations of gas explosions.
- Chapter 6: Conclusion.

Table 1.1: Summary of simulations in this thesis and the data used for comparison.

Description of test	Reference	Simulation condition
Various standard tests of numerical schemes for hyperbolic equations with analytical solutions.	[*Toro, 1999*] and [*Liska and Wendroff, 2003*]	Various
1D detonation simulation with one and two step reaction rate.	[*Erpenbeck, 1969*], [*Bourlioux and Majda, 1992*]	One- and two-step reaction rate, grid resolution 2, 5 and 10 control volumes pr. half reaction zone length.
2D detonation simulation with one step global reaction rate.	[*Gamezo et. al., 1999*], [*Bourlioux and Majda, 1992*]	Single step reaction rate, grid sizes of 20 and 50 control volumes pr. half reaction thickness.
Turbulent shear layer with convective Mach-number 0.51	[*Samimy and Elliot, 1990*]	Testing the grid dependency with grid size 1 mm, 0.5 mm and 0.25 mm. Simulating turbulence in compressible flow with a turbulence model.
Full scale high explosive free field test with 2 l C4	[*Langberg et. al., 2004*]	2D axis symmetry with grid size 0.08 m. Simulating large scale blast in a simple geometry.
Small scale high explosive inside building with 0.5 g of PETN.	[*Reichenbach and Neuwald, 1997*]	3D simulation with grid size 1 mm. Simulating small scale blast in a complex geometry.
Gas explosion in tube with one obstacle, hydrogen-air in 4 m long 107 mm ID tube.	[*Knudsen et. al., 2005a, Knudsen et. al., 2005b*]	2D axis symmetry with grid sizes 1 mm and 2 mm. Simulating flame acceleration and DDT.
Gas explosion in channel with repeated obstacles, hydrogen air in 20, 40 and 80 mm channel with obstacles of BR = 0.5.	[*Teodorczyk, 2007*]	2D and 3D simulation with grid size 0.5 mm and 1 mm. Simulating the different high speed flame propagation regimes.
Gas explosion in pipe with repeated obstacles, methane-air in 12 m long 174 mm ID tube with BR = 0.3 and 0.6.	[*Kuznetsov et. al., 2002*]	2D axis symmetry with grid size 1 mm. Simulating the different high speed flame propagation regimes in a less sensitive gas.

Chapter 2

Review of flame acceleration, DDT and detonation in obstructed channels

From a weak ignition of a combustible gas mixture a flame initially propagates as a laminar flame. Thermo-diffusive and hydrodynamic instabilities distort the flame front and turbulence-flame interaction increase flame area and influence the flame brush to accelerate the flame. [*Dorofeev et. al., 2001*] discussed important parameters for flame acceleration where they considered laminar burning velocity, flame thickness, density ratio across the flame often called expansion ratio, sound speeds, heat capacity ratio, Lewis number, Markstein number and Zeldovich number. A flame expanding with zero velocity in the products will push the reactants in front of itself as shown in figure 2.1. This acceleration is stronger with higher volume expansion and higher velocities in the reactants cause large velocity gradients and more turbulence and flame area increase. Flame-geometry interactions, flame vortex interactions and instabilities discussed in chapter 2.1 increase the flame area and the total reaction rate. Strong acceleration of the reactants due to increased reaction rates cause pressure build-up and pressure waves. In obstructed channels these waves reflect on obstacles and interact with the flame in turn causing compression of the reactants and instabilities that produce increased flame area and increasing flame acceleration.

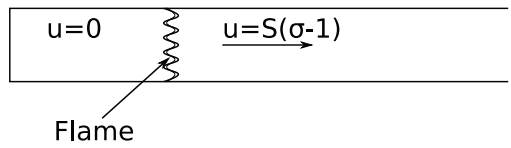

Figure 2.1: Schematics of a flame propagating in a channel from a closed wall, u is the gas velocity, S is the burning velocity and σ is the density ratio.

In obstructed channels and pipes flame obstacle interaction may lead to different propagation regimes. High levels of turbulence may cause quenching of the flame and mixing of hot products and fresh gasses described by [*Lee et. al., 1985*] which causes hot spots with high reaction rates. Shock reflections and focusing cause high temperature in the reactants and spontaneous ignition. A regime seen in obstructed channels and pipes is called

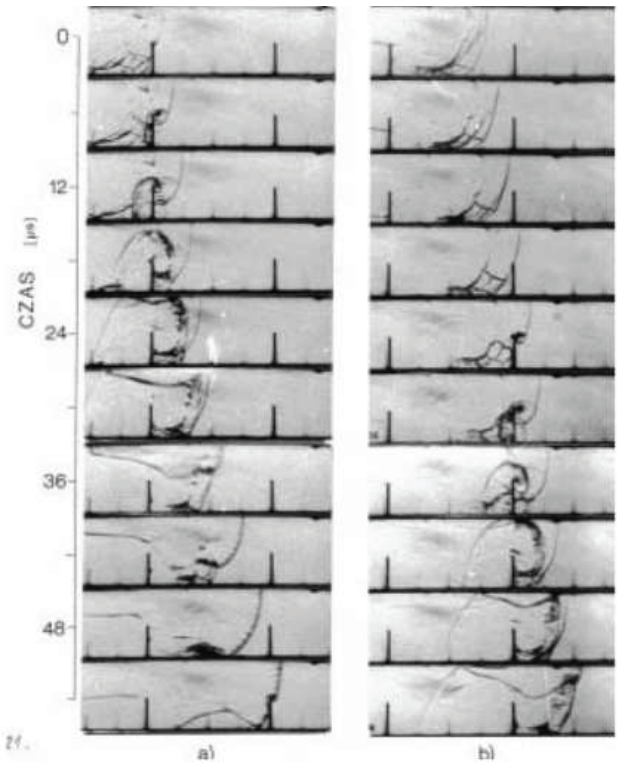

Figure 2.2: Image sequence of the propagation of a quasi detonation. Image is from [*Teodorczyk et. al., 1988*]. The gas mixture is stoichiometric hydrogen-oxygen at 120 torr.

the choking regime which is characterized by flame speeds around the sound speed of the products. This regime is suggested by [*Chao and Lee, 2003*] to be driven by expanding high pressure products over an obstacle. They also suggested that this is no actual flame propagation regime. The quasi detonation regime, [*Lee et. al., 1985*], is characterized by sub-CJ detonation velocity on average. Figure 2.2 shows how a detonation is initiated as a quasi-detonation propagates in a channel where a transition to detonation occurs as the flame passes an obstacle. In figure 2.2 a) the leading shock is focused in the corner between the bottom wall and obstacle in the first frame which ignites the gas and sends a strong shock wave upwards to be reflected at the top wall. The reflected wave reach the flame from the product side causing a compression of the reactants and initiate a detonation. In figure 2.2 b) the transition occurs as the leading shock reflects on the top of the obstacle and the reflected wave is again reflected in the top wall before it interacts with the flame. In figure 2.3 the detonation diffracts over one of the following obstacles and the shock strength is reduced leading to failure of the propagating detonation. In the quasi detonation regime this process is repeated. Figure 2.4 shows flame speed in hydrogen-air

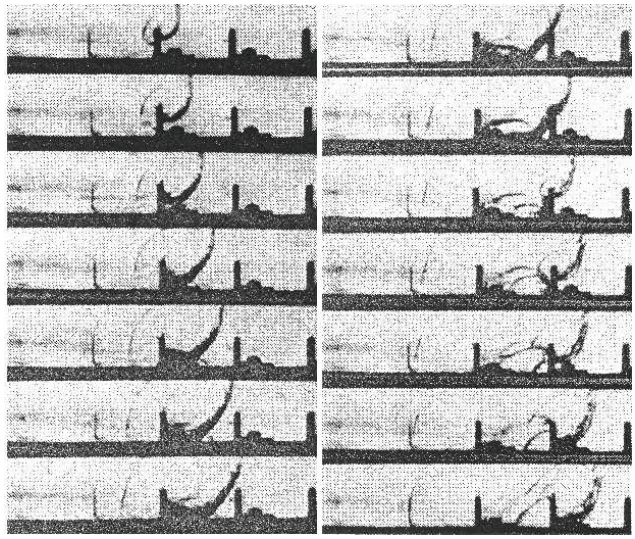

Figure 2.3: Failure of a detonation passing an obstacle. Image is from [*Teodorczyk et. al., 1988*]. The gas mixture is stoichiometric hydrogen-oxygen at 120 torr.

in a channel with repeated obstacles and as a function of concentration where there are abrupt changes in flame speed where the flame changes propagation regime. The maximum flame speed in the 5 cm channel is significantly lower than for the 15 and 30 cm channels because the explosion will not propagate as a detonation but a quasi-detonation.

Suggested reading for comprehensive reviews of flame acceleration, DDT and detonations: [*Lee, 2008*], [*Shepherd, 2008*], [*Ciccarelli and Dorofeev, 2008*], [*Oran and Gamezo, 2007*], [*Shepherd and Lee, 1992*] and the report Flame Acceleration and Deflagration to Detonation Transition in Nuclear Safety [*SOAR, 2000*].

2.1 Instabilities responsible for flame acceleration

This section presents the most common types of instabilities that can be encountered in combustion systems. Instabilities like the Kelvin-Helmholz, Richtmyer-Meshkov, Rayleigh-Taylor and turbulence are instabilities that can occur in all types of fluid flow systems and may cause flame acceleration in reactive flow. The theory of these instabilities are based on non-reactive flow and it is unclear of the effect the flame may have on these instabilities since the flame is not of infinitesimal thickness and can be considered a source of energy at the interface. It might be possible that a flame may respond differently to a force acting on it than an interface separating two inert gasses. [*Teerling et. al., 2005*] studied the instabilities in a flame when it encountered acoustic waves with different frequencies and reported that the flame surface increased to a quasi-steady state where the maximum and minimum in each oscillation is constant.

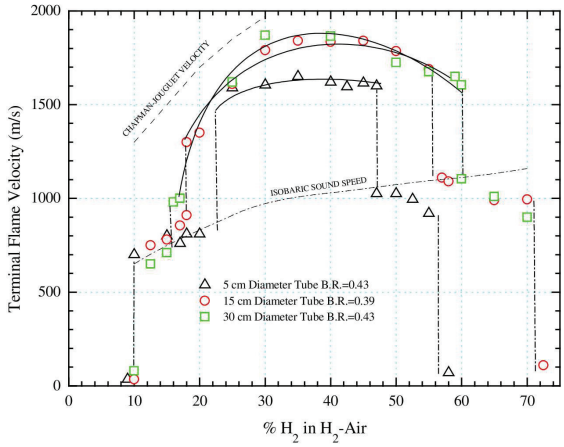

Figure 2.4: Flame speed in hydrogen-air in channels with repeated obstacles with different blockage ratio with respect to concentration [*SOAR, 2000*].

The diffusive-thermal instability is usually seen in the early stages of flame acceleration where the flame propagates as an almost laminar flame. Later turbulence dominates the flame acceleration process by increasing the flame area and influencing the flame brush. Flame-geometry interaction is not considered an instability but can be the most important factor contributing to flame acceleration in complex geometries. In obstacle filled channels vortices are formed in the wake of an obstruction and the total reaction rate increase significantly when it is encountered by a flame. In explosions the Kelvin-Helmholz instability occurs when a flame burns in shear flow like in jets. It is also seen in detonation fronts and might be important in mixing of products and reactants in unstructured detonations where pockets and tongues of unreacted gas can appear far behind the shock front. Figure 2.5 shows the details in a detonation front. In the wake of a propagating triple point the Kelvin-Helmholz instability is seen on the interface between products and reactants.

Richtmyer-Meshkov- and Rayleigh-Taylor-instabilities have similar mechanisms with similar growth rates. When a flame propagates in a complex geometry pressure waves produced by the flame reflects of walls and interact with the flame. Figure 2.6 shows how a curved flame reacts to a shock wave propagating from the reactants towards the flame. The effect shown is commonly known as the Richtmyer-Meshkov instability. If the flame is allowed to propagate with the inverted shape the perturbation will continue to grow due to the Landau-Darrieus instability and continuously increase flame surface area. [*Liñàn and Williams, 1993*] classified combustion instabilities as intrinsic instabilities and chamber instabilities. The intrinsic instabilities are due to the flame itself and are independent on any geometry. The thermal-diffusive and Landau-Darrieus instabilities are typical examples of intrinsic instabilities. The chamber instabilities are dependent

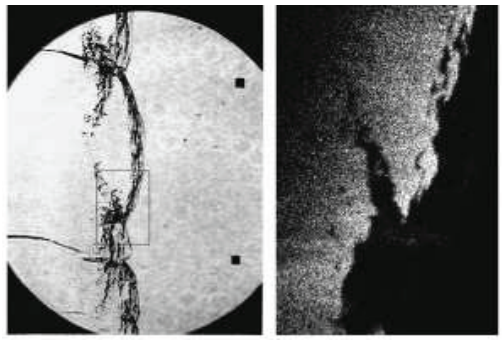

Figure 2.5: Detail of a detonation front in C_2H_4 + $3O_2$ + $10.5N_2$, [*Austin et. al., 2005*].

on the geometry and the flow field and occurs when the flame or flow field interacts with geometry. Kelvin-Helmholz, Rayleigh-Taylor and Richtmyer-Meshkov instabilities, turbulence and vortex-flame interaction are examples of chamber instabilities.

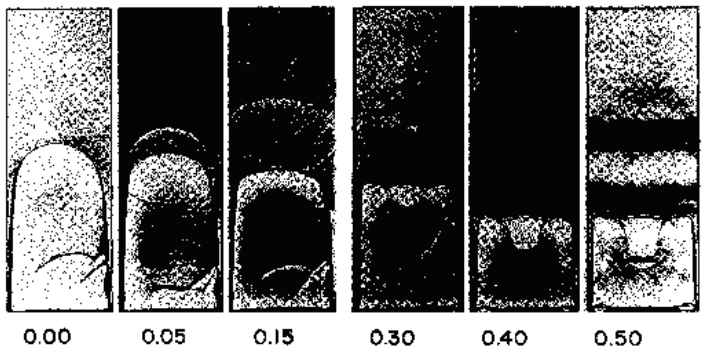

Figure 2.6: Interaction between a weak shock and a flame, [*Markstein, 1957*].

Diffusive-Thermal-instability

Diffusive-thermal instability appears in mixtures with Lewis numbers lower than 1. The Lewis number is the ratio of heat and mass diffusivities, $Le = \lambda/(\rho C_p X)$ where λ is thermal conductivity and X is mass diffusivity. Figure 2.7 is a drawing of a curved flame with the direction of heat conduction from the flame into the reactants and mass diffusion of reactants towards the flame. The directions of these transport phenomena is normal to the flame front. If we assume that the flame has the same thickness in the regions called crest and trough then the reaction zone at the crest has a larger volume than the zone at the trough. When the Lewis number is larger than 1 heat is transported faster

towards the pre-heat zone than mass is transported to the reaction zone. Since the crest of the perturbation has a larger volume the flame cools at the crest compared with the trough. The laminar burning velocity is dependent on the temperature in the flame zone and the trough propagates faster than the crest thus stabilizing the flame. If the Lewis number is smaller than 1 radicals are transported faster to the reaction zone than heat is transported away keeping the flame hot. At the crest of the perturbation the flame has a larger volume of radicals than at the trough and reacts faster and the perturbation grows. The diffusive-thermal instability can stabilize the hydrodynamic instability, [*Liñàn and Williams, 1993*].

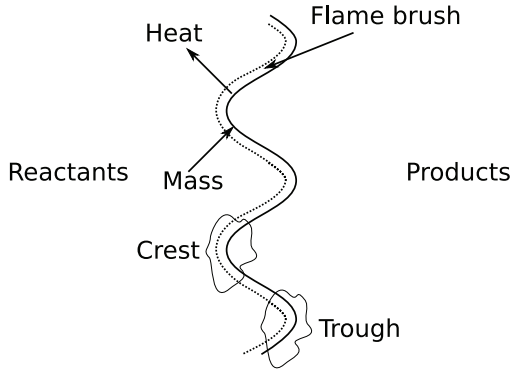

Figure 2.7: Sketch of a perturbed flame front with direction of mass diffusion and heat conduction.

Landau-Darrieus-instability

Landau-Darrieus (LD) ([*Landau, 1944*], [*Darrieus, 1938*]) instability is a hydrodynamical instability that occurs in incompressible reactive flow. By looking at a stationary flame with constant burning velocity the acceleration og the gas across the flame exerts a force on the flow in the direction normal to the flame. This causes the streamlines to diverge in the region where the flame is convex towards the reactants. A sketch of the flame and streamlines is shown in figure 2.8. With diverging streamlines the flow velocity decreases and the flame propagates in the direction of the reactants in a lab reference frame. The flame is pushed back where the streamlines converge and the perturbation grows and the flame surface increase.

Rayleigh-Taylor-instability

Rayleigh presented a study in 1882 [*Lord Rayleigh, 1882*] on the stability of an incompressible fluid with varying density, a similar theory was presented by [*Taylor, 1950*] where he assume incompressible potential flow for a fluid system where an interface separating two fluids of different densities is accelerated. This instability is called the

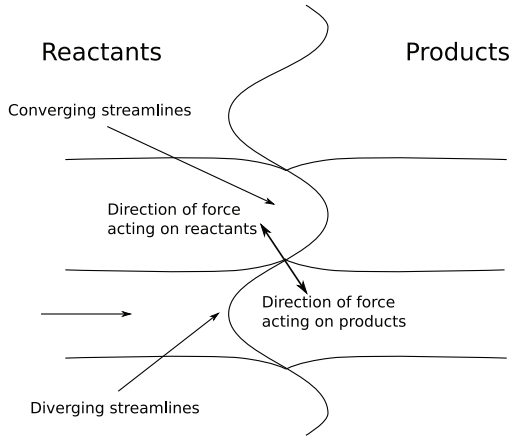

Figure 2.8: Schematic of the Landau-Darrieus instability. The streamlines of the reactants diverges or converges in front of the stationary flame front. The flame propagates faster where the streamlines diverges.

Rayleigh-Taylor instability (RTI). In the RTI the direction of acceleration and the interface is misaligned which causes the perturbation to grow if the acceleration is acting from the light fluid.

Figure 2.9 shows the effect of the RTI on a system with an initial perturbation. The coordinates follow the interface and the accelerating force is acting upwards. In the left image where there is a peak in the initial perturbation more light fluid is accelerated and a force acting on the entire system normal to the mean interface produce a stronger acceleration due to lower mass and a growth of the perturbation. In the right image of figure 2.9 the position of the peak has more heavy fluid and has a lower acceleration. If a constant force is acting on the right interface the minima will have a higher velocity than the peak until the curvature of the perturbation changes and the acceleration with respect to the interface also changes to form a stable situation.

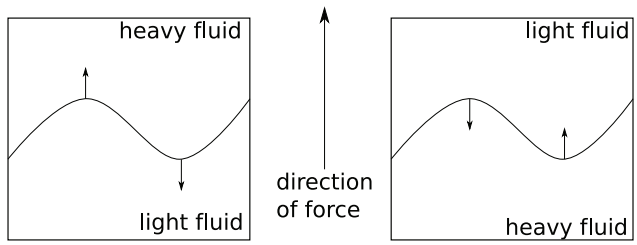

Figure 2.9: The Rayleigh-Taylor instability. The arrows show interface velocities relative to a mean interface position.

If the pressure gradient and the density gradient is at an angle different from 90^o the

force acting on the interface produces vorticity. Equation 2.1 is the conservation equation of vorticity where the last term is the baroclinic source which explains that vorticity is produced if the density gradient and the pressure gradient is not aligned. The effect of vorticity on the development of the instability is discussed by many researchers like [*Hawley and Zabusky, 1989*] and [*Samtaney and Zabusky, 1994*]. In figure 2.10 a pressure gradient (a force) is acting on a density gradient. The pressure gradient exerts the same force on the heavy and the light fluid and the stronger acceleration of the light fluid compared to the heavy fluid produce vorticity. Both a constant force as for the RTI or a short impulsive force which will be discussed for the Richtmyer-Meshkov instability can produce this effect.

$$\frac{\partial \omega_i}{\partial t} + u_j \frac{\partial \omega_i}{\partial x_j} = -\omega_i \left(\frac{\partial u_j}{\partial x_j} \right) + \frac{1}{\rho^2} \frac{\partial \rho}{\partial x_j} \frac{\partial p}{\partial x_k} \epsilon_{ijk} \tag{2.1}$$

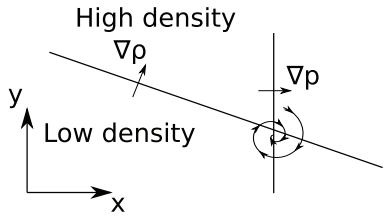

Figure 2.10: Vorticity is produced when a force is exerted on a density gradient.

Figure 2.11 shows a simulation of the RTI with the method presented in chapter 3. An interface with an initial amplitude of 0.2 length units and wave length of 8 units is separating two fluids with different density. A pressure gradient, $\left(\frac{dp}{dx}\right)$, with dimensionless value of 0.25 is acting on the system with the dimensionless density is 1 to the left of the interface and 0.1 to the right. The interface is accelerated towards the left due to the pressure gradient and the perturbation grows.

Richtmyer-Meshkov-instability

[*Richtmyer, 1954*] presented an extension of the RTI where a shock propagates over an interface separating two fluids. The initial conditions for Richtmyers study was a corrugated interface separating two fluids with different density and a planar shock interacting with the interface. Contrary to Taylor, Richtmyers theory assumes compressible and non-potential flow in the region close to the interface. This study looked at the initial part of the instability where the perturbation was much smaller than the amplitude and he could assume a linear expansion of the variables into a mean value for each state and a perturbation. Figure 2.12 shows the different scenarios where a shock is either interacting with a crest or a trough of the corrugated interface and either moving from the heavy or the light fluid. The top left image shows a shock wave propagating through a crest in the corrugation from the heavy fluid and diffracts into the light. Since the shock travels faster in the light fluid a rarefaction wave is sent into the heavy fluid. This diffraction causes the

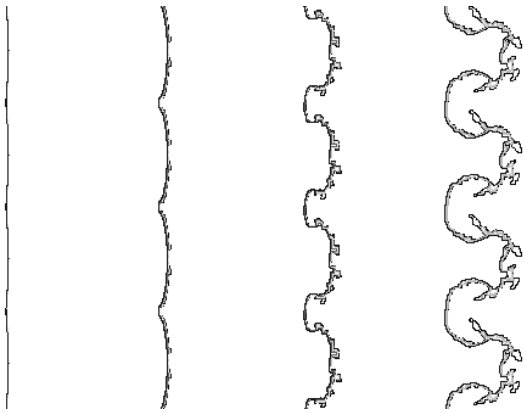

Figure 2.11: An interface from a simulation of the Rayleigh-Taylor instability. The density is 1 to the left of the interface and 0.1 to the right. A constant pressure gradient is acting on the interface with highest pressure to the right.

interface to move faster at the top of the crest than away from it since the velocity component in the x-direction is zero behind the transmitted shock and there is flow only in the y-direction. The interface experiences an inversion of the shape and the perturbation continues to grow in the inverted form. When the same shock is interacting with a trough like in the top right image the shock propagating through the interface produces velocities in the x-direction and a focus in the center of the trough. The focused shock holds back the trough compared to the crest. The effect of the RMI is shown in figure 2.13 where the front is shown at different times from the initial shape at t0 to time t2 after the shock has passed the interface. It is possible to find two gasses where the transmitted shock speed is higher in the heavy gas than the incident shock speed in the light and it might be correct to talk about low and high shock speeds compared with heavy and light gas. The explanation of the instability is still the same and Richtmyers linear model of the instability should also handle this correctly even if the development of the instability might be somewhat different. Meshkov verified Richtmyers theory with experiments [*Meshkov, 1969*] but with the violation of Richtmyers criterion of the amplitude of the perturbation being much smaller than the wave length. Some of the experimental results did not fit Richtmyers theory and the mis-match was explained as deviation from the linear theory due to the violation of the criterion.

Richtmyers theory does not include non-linear growth of the perturbation but his description of the phenomena explains the rotational motion observed as a shock passes a density gradient. By looking at the vorticity equation, 2.1, the cross product of the density gradient and pressure gradient produce vorticity and is evident in later stages of the RMI.

Kelvin-Helmholtz-instability

The Kelvin-Helmholtz (KHI)([*Lord Kelvin, 1871*], [*von Helmholtz, 1868*]) instability appears in shear flow where there is an interface separating fluids with different density.

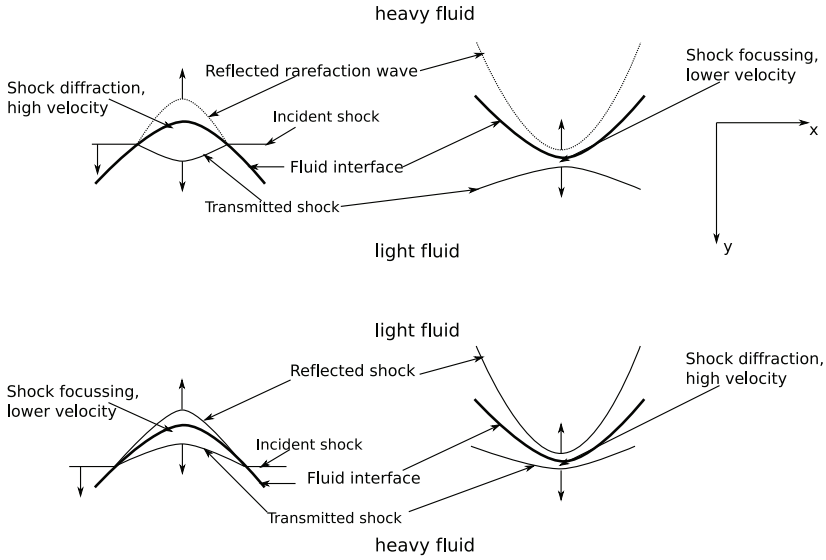

Figure 2.12: The process of the Richtmyer-Meshkov instability. Top left: shock propagating from heavy into light fluid through a crest in the perturbation. Top right: shock propagating from heavy into light fluid through a trough in the perturbation. Bottom left: shock propagating from light into heavy fluid through a crest in the perturbation. Bottom right: shock propagating from light into heavy fluid through a trough in the perturbation.

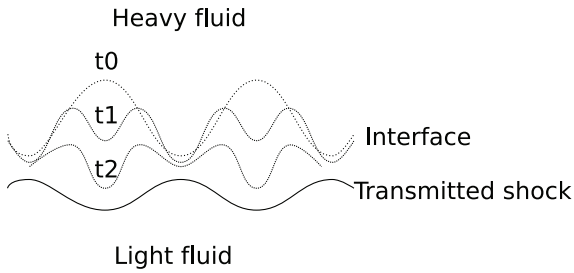

Figure 2.13: The effect of the RMI as the shock propagates from a heavy into a light gas. The interface is shown at different times, the interface at t0 is the initial corrugated interface.

The KHI can often be seen in stratified flow or flow with two or more fluids with different densities such as products and reactants in a combustion processes. Figure 2.14 shows the principle of the KH instability in reactive flow where a flame separates two gasses and there is shear flow in the flame plane. A perturbation in the flame is shown as a wavy front where the streamlines of the flow is shown as solid lines. Due to the perturbations these lines are converging where the flame is convex towards the flow and diverging where the

flame is concave. For a simple explanation of the effect of the converging and diverging streamlines incompressible flow is assumed but the effect is similar for compressible flow below Mach number 1. The converging streamlines produce higher velocity and lower pressure and diverging streamlines produce lower velocity and higher pressure. At one period of the perturbation the flow has low pressure on one side and high pressure on the other side of the interface which creates a force that moves the interface in the direction of the low pressure and increase the amplitude of the perturbation. This is similar to the RTI explained earlier and according to the vorticity equation the KHI will produce vorticity at the interface due to the baroclinic source term. The geometry of the interface in it self causes vorticity in the fluid as it flows from crest into a trough. When the perturbation is large enough the fluid flow separates from the interface and create vortices behind the peaks. The roll-up of the interface due to the separation is commonly thought of as part of the KHI.

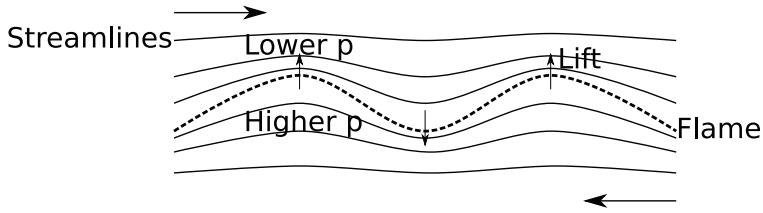

Figure 2.14: Schematics of the Kelvin-Helmholz-instability with a flame. The doted line is the flame and the solid lines are streamlines.

Turbulence in reacting flow

A detailed description of the complex physical behavior of turbulence is a difficult task but the origin of turbulence might give some idea of the effect turbulence has on a flow system. The non-linear term in the momentum equation, which describes convection of momentum, will try to enhance any perturbations in the flow. If the perturbations are small the diffusion of momentum (viscous forces) will try to dampen the perturbations. In a transition from laminar to turbulent flow with small perturbations the competition between these two transport processes will show as small waves called Tollmien-Schlichting (TS) waves. These perturbations grow and eventually lead to turbulent flow. If the perturbations are sufficiently large these waves are not seen. Typical examples of large perturbations are jets or flow past obstacles where the perturbations produce an inflection point in a shear layer and the diffusion of momentum is negligible in the transition to turbulence. Turbulence spreads through all wave-lengths from a large scale which is a characteristic size of the geometry to the smallest scale. The mechanism of the spreading is thought to be mainly due to vortex stretching. In a non-uniform flow field a vortex-tube can be stretched in its longitudinal direction to reduce the tube diameter and increase the rotational velocity due to conservation of vorticity. When the velocity of the rotation increases the kinetic energy also increases. When this energy is taken from the main flow field it can be interpreted as the production of turbulence. The smallest scales are called the

Kolmogorov scale where the turbulence does not have enough momentum to overcome the viscous forces in the fluid and will be dampened, this is the process of dissipation of turbulence, [*Chomiak, 2000*].

Turbulence is a significant contributor to flame acceleration as flame-turbulence interaction increase the flame surface and smaller turbulent scales can influence the flame brush and increase transport of reactants and radicals. The Borghi diagram in figure 2.15 explains how turbulence effects the flame at different length and time scales. The horizontal axis in this diagram is the ratio of integral length scale (I) and laminar flame thickness (δ_L). The vertical axis is the ratio of the turbulent velocity ($u' = \sqrt{\overline{u'(t)^2}}$), or the velocities of the integral turbulent eddies, and the laminar burning velocity S_L. The Damköler number (Da) is τ_I/τ_c where τ_I is the time scale of the integral turbulent eddies, $\tau_I = I/u'$ and τ_c is the chemical time scale of laminar combustion, $\tau_c = \delta_L/S_L$. The Karlovitz number relates the chemical time scale to the Kolmogorov turbulent time scale, $Ka = \tau_c/\tau_k$ where $\tau_k = l_k/u'_k$. The Reynolds number Re_T is based on the integral turbulent scales, $Re_T = \frac{u'I}{\nu}$.

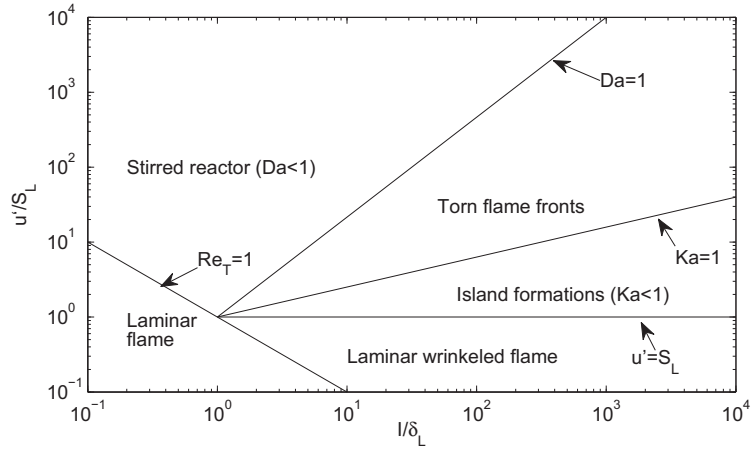

Figure 2.15: The Borghi diagram as presented by [*Warnatz et. al., 1999*].

A flame that experiences large turbulent length scales but low intensity burns laminar but is wrinkled. With higher turbulent intensities the flame wrinkling is more violent and islands of products and reactants are formed. Both of these two regimes are characterized by $Ka < 1$ and the chemical time scale is smaller than the Kolmogorov time scale. In the torn flame front region the Kolmogorov turbulent time scales are smaller than the chemical time scale and the turbulence increase flame thickness and possibly quenches the flame. Since $Da > 1$ the integral time scale is larger than the chemical time scale. For $Da < 1$ and $Ka > 1$ all turbulent motions are faster than the chemical rates and the reactions occur in distributed zones like a well stirred reactor.

Modelling turbulence

Modelling turbulence is one of the major challenges in CFD research and are no general turbulence model for all flow situations. Methods like LES where the mesh spacing is small and the large scale turbulence is resolved in space and time and Direct Numerical Simulations where all turbulent scales are resolved are getting more popular with the increase of computational power. But there is still a long way to go before this can be applied to engineering problems.

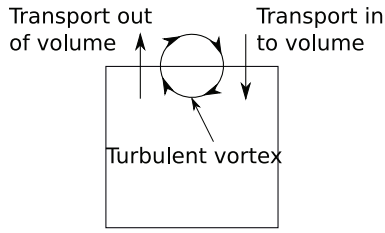

Figure 2.16: The principle of turbulent transport. [*Versteeg and Malalasekera, 2007*].

Traditional turbulence modelling separates all variables into mean values and turbulent fluctuations as in equation 2.2. By averaging the transport equations either in time or as an ensemble the convective terms produce non-zero averages of the fluctuation terms. These terms are called turbulent stresses. The turbulent stresses are new variables that need closure and is the focus of all turbulence modelling. Including the density in the averaging process is common in compressible turbulence modelling and is called Favre averaging seen in equation 2.3. By using Favre averaging only the convective terms produce new variables even though the transient terms are non-linear.

$$u(t) = U + u'(t) \tag{2.2}$$

$$\tilde{u} = \frac{1}{\bar{\rho}} \lim_{\Delta t \to 0} \int_0^{\Delta t} \rho u dt \tag{2.3}$$

The Favre averaged equations of mass, momentum and energy is shown in equations 2.4 to 2.6 and equation 2.7 are the turbulent stresses.

$$\frac{\partial \bar{\rho}}{\partial t} + \frac{\partial}{\partial x_i} \left(\bar{\rho} U_i \right) = 0 \tag{2.4}$$

$$\frac{\partial \bar{\rho} U_i}{\partial t} + \frac{\partial}{\partial x_j} \left(\bar{\rho} U_j U_i \right) = -\frac{\partial \bar{p}}{\partial x_i} + \frac{\partial}{\partial x_j} \left(\mu \frac{\partial U_i}{\partial x} \right) - \frac{\partial}{\partial x_j} \left(\widetilde{\bar{\rho} u_j' u_i'} \right) \tag{2.5}$$

$$\frac{\partial \bar{\rho} \widetilde{E}}{\partial t} + \frac{\partial}{\partial x_i} \left(\bar{\rho} U_j \widetilde{E} \right) = -\frac{\partial}{\partial x_j} \left(\bar{p} U_j \right) + \frac{\partial}{\partial x_j} \left(\lambda \frac{\partial \widetilde{T}}{\partial x_j} \right) - \frac{\partial}{\partial x_j} \widetilde{\bar{\rho} u_j' E'} \tag{2.6}$$

The turbulent stresses are not physical stress but a modelling approach treat these as such. The turbulent transport of mass, momentum and energy into and out of a control

volume acts as "large scale diffusion" as principally shown in figure 2.16. Even by looking at mean values of the variables the turbulence transports properties into and out of a control volume. Since this is occurring at a scale smaller than the control volumes it can be viewed as a diffusion process even though turbulence is convective.

$$\tau_{ij} = \bar{\rho}\widetilde{u_i' u_j'} \tag{2.7}$$

The most popular method for modeling turbulence is the Boussinesq approach that treat the turbulent stresses as Newtonian viscous stresses as shown in equation 2.8. The Boussinesq approach assumes that the coefficient of proportionality between the stresses and the strain rates is isotropic and dependent on the turbulent kinetic energy shown in equation 2.9. Equation 2.10 is the strain rate tensor for fluids.

$$\tau_{ij} = 2\mu_t S_{ij} - \frac{2}{3}\rho k \delta_{ij} \tag{2.8}$$

$$k = \frac{1}{2}\widetilde{u_i' u_i'} \tag{2.9}$$

$$S_{ij} = \frac{1}{2}\left(\frac{\partial U_i}{\partial x_j} + \frac{\partial U_j}{\partial x_i}\right) \tag{2.10}$$

Turbulent kinetic energy is often used as a variable to describe the general turbulence level in a flow field. Well known turbulence models for turbulent stresses are k-ϵ [*Chou, 1945*] and k-ω [*Wilcox, 1993*]. Both of these use the turbulent kinetic energy as one variable and another variable to describe the length scale of the turbulence.

2.2 Transition to detonation

The pressure increase from flame acceleration may form shock waves that increase the temperature of the reactants and change the flame front shape. Reflections of shock waves further heats the reactants that start to react by chain branching and form radicals which in turn reacts exothermally. The heating of reactants and formation of radicals is similar to a laminar flame but for a detonation the heating is by compression. The time from the gas is heated to the exothermal reactions start is called the induction time. Some define the induction time as the time from a particle is heated to the maximum exothermal reaction rate [*Shepherd, 2008*]. [*Schultz and Shepherd, 2000*] has compiled theoretical and experimental data on induction times for a large variety of gasses.

$$\tau = Aexp\left(\frac{E_a}{RT}\right) \tag{2.11}$$

A typical form of a simplified model for the induction time is shown in equation 2.11. A variable α can be defined which is the time integral of the inverse of the induction time, as seen in equation 2.12. Where t_0 is the time when a fluid particle is compressed by a shock wave and α describes how far the radical producing reactions have come. When α

reaches 1 the exothermal reactions start.

$$\alpha = \int_{t_0}^{t} \frac{1}{\tau} dt \tag{2.12}$$

The SWACER (Shock Wave Amplification through Coherent Energy Release) [*Lee and Moen, 1980*] mechanism explains that the formation of a strong shock wave that ignites the reactants is not necessarily enough to make a transition from deflagration to detonation. The reaction rate need to be high enough to increase the strength of the shock wave but if the reaction rate is too high the flame catches up to the shock wave and will not burn a compressed gas and the process only acts as constant volume combustion. A similar explanation for transition to detonation is the Zeldovich gradient mechanism [*Zeldovich, 1970*] where there is a gradient in α in the reactants. A sufficiently strong hot-spot ignites the gas and create a shock wave followed by a reaction zone that propagates from where α is 1 in the direction of the gradient. The magnitude of the gradient determines the speed of the reaction front. If the gradient is too steep or too flat a detonation will not be initiated. A drawing of this effect is shown in figure 2.17. The hot spot may be created from shock reflections ([*Lee and Moen, 1980*], [*Thomas and Bambrey, 2002*]) or high reaction rates due to turbulence ([*He, 2000*], [*Kuznetsov et. al., 2005*]) or heated pockets of unreacted gas [*Khoklov and Oran, 1999*].

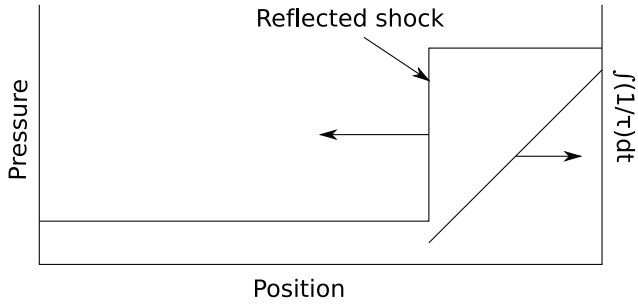

Figure 2.17: Zeldovich gradient mechanism. The Right vertical axis i the time integral of the inverse of the induction time. When this value reaches 1 the exothermal reactions start and the gradient of α determines the speed of the reaction wave as it propagates through the pre-compressed gas.

DDT from reflection of shock waves can manifest itself as either a strong or mild ignition [*Vermeer et. al., 1972*]. In the strong ignition case the reflected shock wave directly or almost directly initiates a detonation as described above. The mild ignition occurs when several local flames lead to a detonation. The difference in these two cases are the induction time gradient. For the strong ignition the shock wave creates a steep gradient where the gas ignites in a large area due to compression and a flame follows the shock wave. For the mild ignition the reflected wave creates smaller gradients where disturbances from for instance boundary layers create small volumes with higher temperatures that eventually ignites to create a spotty ignition. Schlieren photographs and descriptions

of these two ignition mechanisms are presented by Thomas and Bambrey [*Thomas and Bambrey, 2002*] and also shown in figure 2.18. [Urtiew and Oppenheim, 1966] showed

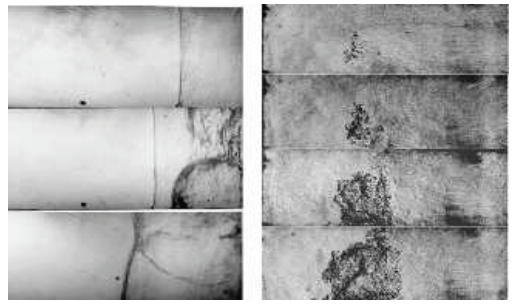

Figure 2.18: DDT in shock reflection. Shock is reflected off the wall at the right side of the images. The three images on the left show the strong ignition and the four on the right show the mild ignition. The gas is mixture is C_2H_4+3O_2+12Ar at 5.3 kPa initial pressure. The incident Mach numbers are 2.64 for the left case and 2.31 for the right [*Thomas and Bambrey, 2002*].

with experiments that DDT can occur at four different positions when a flame propagates in a channel. 1) Explosion between flame and shock front. 2) Explosion at the flame front. 3) Explosion at the shock front. 4) Explosion at a contact surface.

2.3 Detonations

Mathematical representation of detonations in gas mixtures is explained in its simplest form by the Chapman-Jouguet theory [*Chapman, 1899*], [*Jouguet, 1917*]. The CJ theory looks at a steady front where the shock and reaction wave is coupled as one wave and is a solution of the inviscid conservation equations of mass, momentum and energy shown here in equations 2.13-2.15. Figure 2.19 shows the Rayleigh-lines which are the combined mass and momentum equations and the Hugoniot-curve which is a combination of all three equations. The points where the Rayleigh lines are tangent to the Hugoniot curve are called CJ-states, see figure 2.19. The upper CJ-state is the CJ-detonation and the lower is the CJ-deflagration. Both states are characterized by Mach-number 1 in the products with respect to the reaction front. The Rayleigh lines can intersect the Hugoniot curve giving two deflagration solutions and two detonation solutions usually called strong and weak solutions.

$$\rho_u \left(u_u - D\right) = \rho_b \left(u_b - D\right) \tag{2.13}$$

$$\rho_u \left(u_u - D\right)^2 + p_u = \rho_b \left(u_b - D\right)^2 + p_b \tag{2.14}$$

$$h_u + \frac{1}{2}\left(u_u - D\right)^2 = h_b + \frac{1}{2}\left(u_b - D\right)^2 \tag{2.15}$$

A more detailed model for a one-dimensional detonation front is the ZND theory ([*Zel'dovich, 1940*], [*von Neumann, 1942*], [*Döring, 1943*]) where the reaction zone

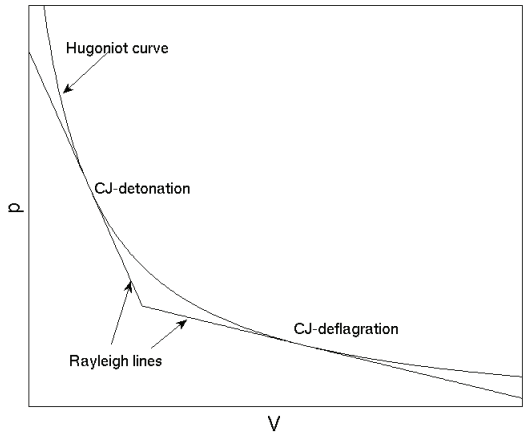

Figure 2.19: The Hugoniot curve and the two Rayleigh lines tangent to the Hugoniot curve giving the CJ-deflagration and CJ-detonation.

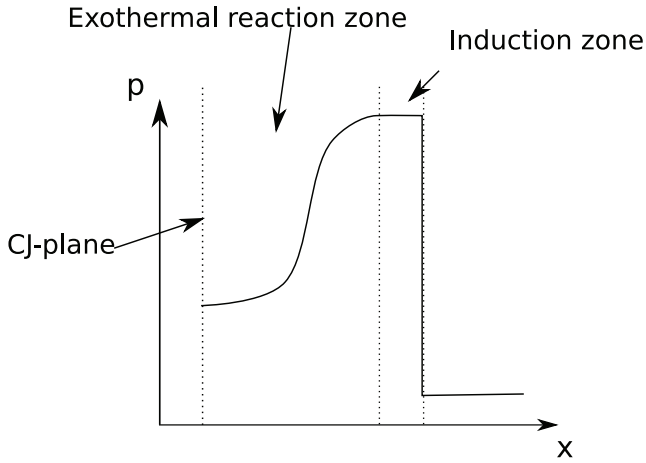

Figure 2.20: Pressure profile of a detonation front as described in the ZND-theory.

thickness is taken into account. Figure 2.20 shows a typical ZND detonation front pressure profile. A simplified theory assumes that in the induction zone no heat is released where the state behind the leading shock is often referred to as the von Neumann spike. The CJ plane discussed by the Chapman-Jouguet theory can be found behind the reaction front.

Detonation in gasses are in reality not stationary planar waves. The structure of a detonation wave is usually very complex and there are transverse waves normal to the

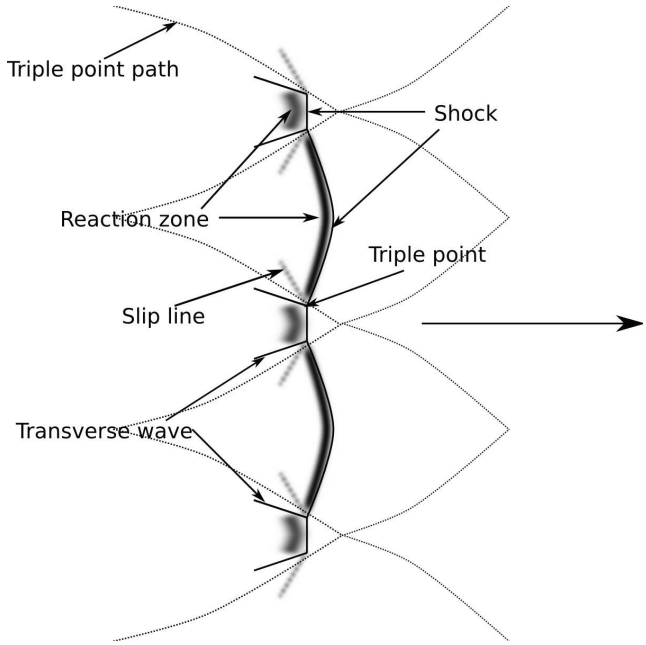

Figure 2.21: Structure of a cellular detonation front. The dashed line shows the triple point trajectories.

front. As first reported by [*Campbell and Woodhead, 1927*] and later [*Densiov and Troshkin, 1959*] discovered the importance of these transverse waves. [*Erpenbeck, 1969*] presented a mathematical study on the stability of one-dimensional detonation waves for a simple single step reaction model. He showed that for some gasses the front pressure was not constant but oscillated. These oscillations were also discussed by [*Fickett and Davies, 1979*]. [*Taki and Fujiwara, 1978*] presented the first simulation results of a two-dimensional non-planar detonation and [*Bourlioux and Majda, 1992*] presented a study where the reactive Euler equations with a single step reaction rate where solved in two dimensions with the FCT numerical scheme.

Figure 2.21 shows a schematic representation of the non-planar or cellular detonation front. The triple point trajectories draws the typical fish-scale pattern that can be seen in experiments where a smoked foil is placed inside a channel or pipe. The triple point then draws this pattern in the soot on the walls like in figure 2.22 which shows a smoked foil from experiments with methane-air. In figure 2.23 the streamlines with respect to the triple point in a detonation front shows how the slip line separates gas that has experienced one and two shock waves and has different density and velocities.

The regularity of the detonation cells are dependent of the reaction energy and activation energy of an overall induction reaction. The overall induction reaction can be modelled as a one-step reaction rate for the induction zone. [*Austin, 2003*] performed experiments with different reduced activation energies $\Theta = E_a/RT_{vN}$ where E_a is the

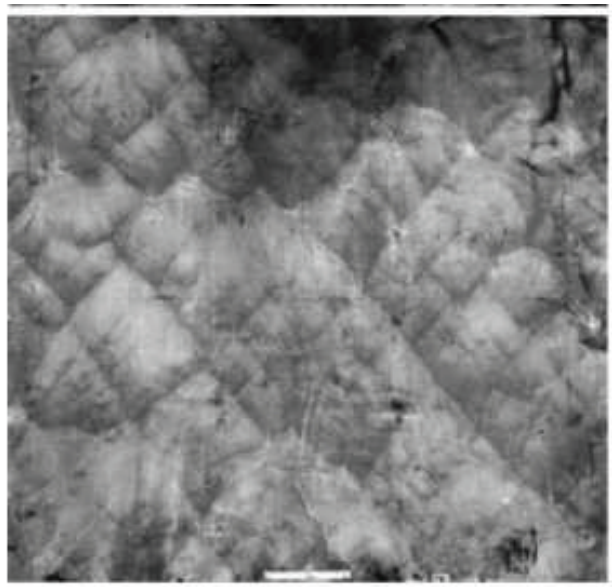

Figure 2.22: Soot tracks in smoked foil of a detonation in 12 $\%$ methane in air, [*Kuznetsov et. al., 2002*].

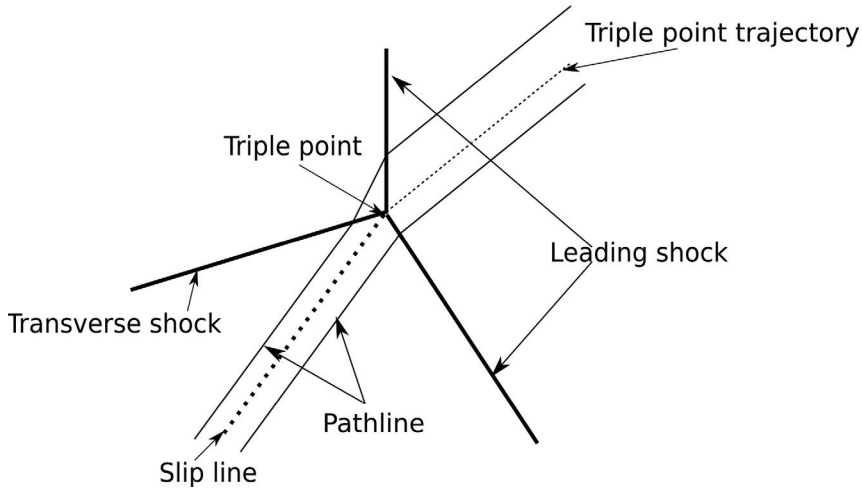

Figure 2.23: Schematic representation of the flow direction behind the leading shock of a detonation.

induction reaction activation energy and T_{vN} is the temperature behind the unperturbed shock wave also called the von Neumann state temperature. The reduced activation en-

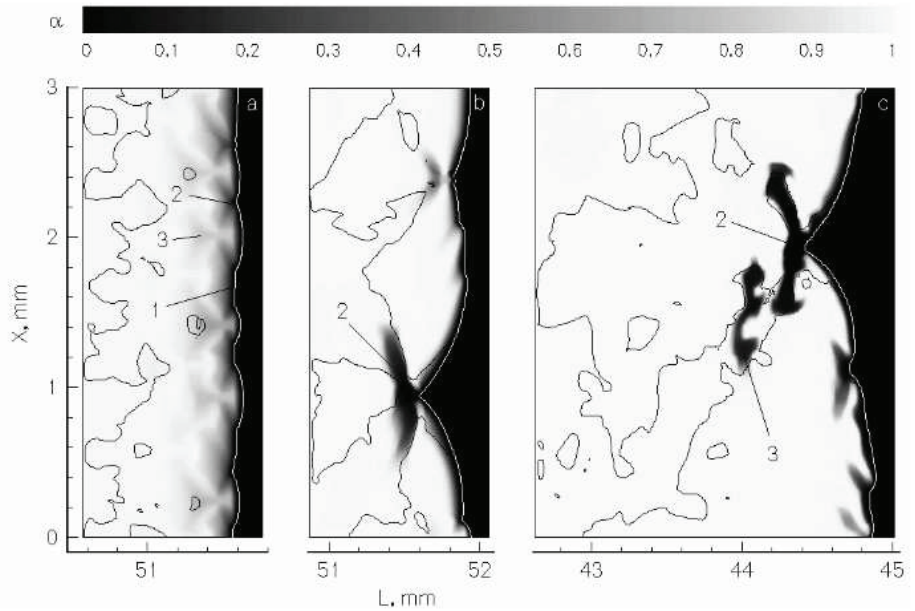

Figure 2.24: Simulation of unstable detonation fronts by [*Gamezo et. al., 1999*]. a) E_a/RT_{vN}=2.1, b) E_a/T_{vN}=4.9, c) E_a/T_{vN}=7.4

ergy gives a measure of the induction zone thickness. If the reduced activation energy is small the induction zone is kept short over the detonation cell cycle. If the reduced activation energy is high the induction zone becomes long in the cell cycle where the shock and reaction zone is decoupled due to shock diffraction. The re-initiation of the detonation is caused by triple point collisions which may take place ahead of the reaction zone and can form pockets of unreacted gas between the propagating flame front and the newly formed detonation. These pockets might burn slowly far behind the detonation front. This effect is shown by simulations by [*Gamezo et. al., 1999*] in figure 2.24 c). Figure 2.25 shows experimental results for different cellular structures with different reduced activation energies.

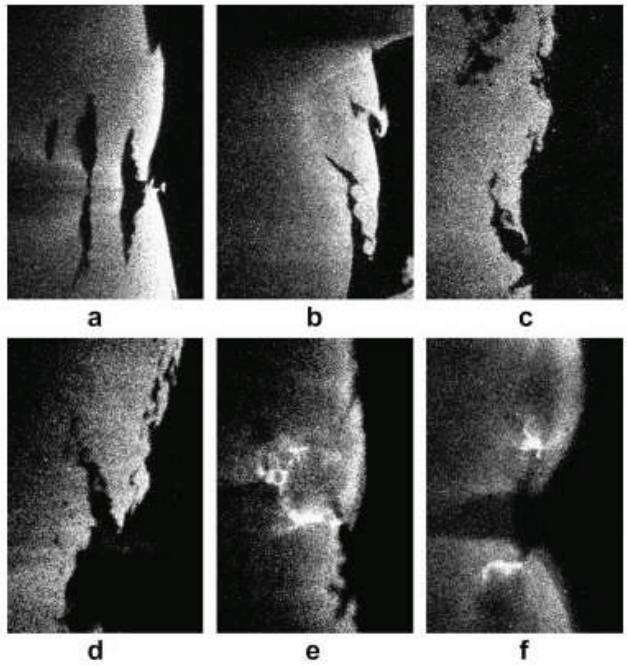

Figure 2.25: PLIF images of unstable detonation fronts ([*Austin, 2003*], [*Pintgen, 2004*], [*Shepherd, 2008*]). a) E_a/RT_{vN}=6, $\bar{\Delta}$=3.4 b) E_a/T_{vN}=7, $\bar{\Delta}$=4.6 c) E_a/T_{vN}=8-9, $\bar{\Delta}$=7.3 d) E_a/T_{vN}=11-12, $\bar{\Delta}$=2.7 e) and f) E_a/T_{vN}=11-13, $\bar{\Delta}$=9.7

Chapter 3

Models and methods

This chapter describes the models and solvers used to simulate gas explosions and blast waves in this thesis. Chapters 3.1 to 3.3 presents the mathematical models. Chapters 3.4 and 3.5 is a discussion on thermodynamics in explosion modelling and chapters 3.6 to 3.7 show the numerical methods for solving the models.

3.1 Conservation equations

The conservation equations of mass, momentum and energy are the basic models for fluid flow and shown in equations 3.1-3.3 for a Newtonian fluid, neglecting work done by viscous forces.

$$\frac{\partial \rho}{\partial t} + \frac{\partial}{\partial x_i}\left(\rho u_i\right) = 0 \tag{3.1}$$

$$\frac{\partial \rho u_i}{\partial t} + \frac{\partial}{\partial x_j}\left(\rho u_j u_i\right) = -\frac{\partial p}{\partial x_i} + \frac{\partial}{\partial x_j}\left(\mu \frac{\partial u_i}{\partial x_j}\right) \tag{3.2}$$

$$\frac{\partial E}{\partial t} + \frac{\partial}{\partial x_i}\left(u_i E\right) = -\frac{\partial}{\partial x_i}\left(p u_i\right) + \frac{\partial}{\partial x_i}\left(\lambda \frac{\partial T}{\partial x_i}\right) \tag{3.3}$$

The total energy E is shown in equation 3.4.

$$E = C_v T + \frac{1}{2}\rho u_i u_i + E_{Ch} \tag{3.4}$$

The $C_v T$ term is the internal energy and can be modelled by ideal gas law as seen in equation 3.5.

$$U = C_v T = \frac{p}{\gamma - 1} \tag{3.5}$$

E_{Ch} is the change in enthalpy due to chemical reactions.

3.2 Turbulence model

To model the sub-grid scale turbulence the presented method uses a model based on the turbulent kinetic energy equation. The model is a conservation equation of the turbulent

kinetic energy, k, with a production term and a destruction term as shown in equations 3.6-3.8. The turbulent viscosity is used to calculate the turbulent stresses together with equation 2.8. The left hand side of equation 3.6 describes the rate of change of k for a fluid particle. The first term on the right hand side describes production of turbulence, the second term describes dissipation of turbulence and the third term describes turbulent transport of turbulence.

$$\frac{\partial \rho k}{\partial t} + \frac{\partial}{\partial x_i}\left(\bar{\rho} U_i k\right) = -\tau_{ij}\frac{\partial U_i}{\partial x_j} - \frac{C_\epsilon \rho k^{\frac{3}{2}}}{l} + \frac{\partial}{\partial x_i}\left(\frac{\nu_t}{\sigma}\frac{\partial k}{\partial x_i}\right) \tag{3.6}$$

$$\tau_{ij} = -2\rho\nu_t(S_{ij} - \frac{1}{3}S_{kk}\delta_{ij}) + \frac{2}{3}\rho k\delta_{ij} \tag{3.7}$$

$$\nu_t = C_\nu k^{\frac{1}{2}} l \tag{3.8}$$

Here the C_ϵ and C_ν are model constants and are usually set to $0.09^{3/4}$ and $0.09^{1/4}$ respectively, l is a length scale of the turbulence and the tensor S_{ij} is the strain rate. The origin of the closure coefficients is an assumption that the dissipation rate of turbulent kinetic energy, ϵ, can be expressed as a function of k as in equation 3.9 where C_μ is usually set to 0.09, [*Versteeg and Malalasekera, 2007*].

$$\epsilon = C_\mu^{3/4}\frac{k^{1/2}}{l} \tag{3.9}$$

[*Prandtl, 1925*] proposed a turbulence model where the turbulent viscosity is the product of a length scale and a velocity scale. Equation 3.10 is Prandtl's mixing length model where l_{mix} is the mixing length.

$$.\tau_{xy} = -\rho l_{mix}^2 |\frac{\partial U}{\partial y}|\frac{\partial U}{\partial y} \tag{3.10}$$

Townsend [*Townsend, 1976*] reported that for boundary layers, shear layers and wakes the turbulent stress in the axial-normal plane can be approximated as in equation 3.11.

$$\tau_{xy} = -0.3\rho k \tag{3.11}$$

Combining equation 3.10 and 3.11 we get an expression for the mixing length, equation 3.12.

$$l_{mix} = \sqrt{0.3k\left(\frac{\partial U}{\partial y}\right)^{-2}} \tag{3.12}$$

In equilibrium turbulent flow the length scale, l, in equation 3.6 and the mixing length is about the same. This is only valid if the ratio of production to dissipation is constant [*Wilcox, 1993*] and is a simplification when used for transient explosion modelling.

For compressible effects on turbulence modelling the turbulent Mach number, M_t is introduced, as seen in equation 3.13 [*Wilcox, 1993*].

$$M_t^2 = \frac{2k}{c^2} \tag{3.13}$$

The compressibility is assumed to only effect the dissipation of turbulence as dilatation dissipation. An approach to include these effects is to modify the model constant C_ϵ by a function of the turbulent Mach number. The effects of compressibility is assumed to be important for flows with $M_t > 0.1$ which is for air at normal temperature $k > 5000$. Wilcox [*Wilcox, 1993*] proposed a model for modifying the dissipation as in equation 3.14.

$$C_\epsilon = C_{\epsilon,inc}\left(1 + \xi f(M_t)\right) \tag{3.14}$$

Where ξ is 1.5, $C_{\epsilon,inc}$ is the incompressible closure coefficient and the turbulent Mach number function is seen in equation 3.15.

$$f(M_t) = \left(M_t^2 - 0.25^2\right)\aleph(M_t - 0.25) \tag{3.15}$$

$\aleph$ is the Heaviside step function. For this model the effect of compressibility starts to become important for turbulent Mach numbers larger than 0.25.

3.3 Combustion model

The conservation of species is represented as a variable β which is a normalized concentration or a reaction progress variable. The value of β is between 0 and 1, where 0 is reactants and 1 is products. The transport equation of β is shown in equation 3.16. The total reaction rate, $\dot{\omega}$, is a combination of a progress variable approach, [*Poisont and Veynante, 2001*], and chemical kinetics and is seen in equation 3.17. The idea of the model is that for laminar and turbulent combustion the progress variable approach dominates the total reaction rate and the kinetics only contribute in the later stages of combustion where β is close to the products value. With an increase in the reactant temperature the kinetic term becomes significant in the total reaction and for detonations it is the dominant term.

$$\frac{\partial \rho\beta}{\partial t} + \frac{\partial}{\partial x_i}\left(\rho U_i \beta\right) = \dot{\omega} \tag{3.16}$$

$$\dot{\omega} = max\left[\rho_u S_T \sqrt{\left(\frac{\partial \beta}{\partial x_i}\right)^2}, \dot{\omega}_k\right] \tag{3.17}$$

The energy term due to reactions in the energy equation 3.3 is modelled as equation 3.18. Where q is the change in enthalpy per unit mass of the mixture due to reactions.

$$E_{Ch} = \rho q \beta \tag{3.18}$$

Figure 3.1 shows the reaction rates for the two terms across a flame front. The reaction rate $\dot{\omega}_T$ is highest where the progress variable gradient is highest and thus the heat release is highest. The peak reaction rate causes pressure gradients in both directions with a peak between β=0 and β=1. The pressure gradients create velocities in the direction of the negative pressure gradients and can lead to significant artificial thickening of the flame. The Arrhenius kinetic term $\dot{\omega}_k$ which is dependant on temperature can counteract this

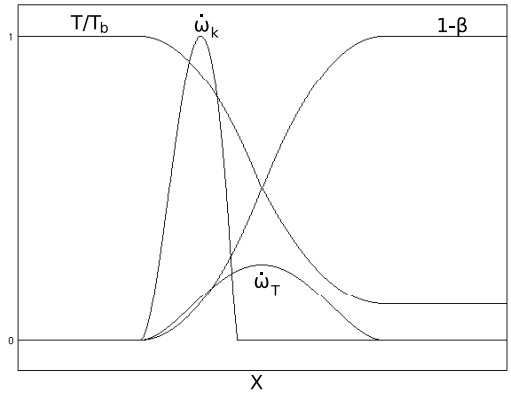

Figure 3.1: Schematic representation of reaction variable, temperature, and reaction rates across a flame. T/T$_b$: temperature divided by temperature of the totally burned gas. 1-β: reaction variable. $\dot{\omega}_k$: reaction rate from chemical kinetics. $\dot{\omega}_T$: reaction rate from mixing rate.

thickening and keep the flame thin. For deflagrations when the Arrhenius term is handling the later stage of combustion turbulence might not be as important as it is closer to the reactants. This model assumes that small scale turbulence does not play an important part in the overal reaction rate in detonations.

Figure 3.2 shows a thin flame on a coarse computational mesh. For progress variable approaches the flame is averaged over a few control volumes. The turbulence in the control volumes containing the averaged flame front is accounted for by the turbulence model but instabilities addressed in chapter 2 are not. These instabilities may occur in laminar flow and is not captured by the turbulence model if the length scale is smaller than the mesh size. These instabilities may even produce turbulence which is not modelled.

The turbulent burning velocity is a model presented by Flohr and Pitsch [*Flohr and Pitsch, 2000*] in equation 3.19.

$$S_T = S_L \left(1 + A \frac{\sqrt{Re \cdot Pr}}{Da^{0.25}} \right) \tag{3.19}$$

Where A is a model constant and is usually set to 0.52. Re is a Reynolds number for the sub-mesh turbulence and is modelled as $Re_\Delta = \frac{u'l}{\nu}$, l is the length scale of the turbulence, Pr is the Prandtl-number, Da is the sub-mesh Dahmkohler number, Da=$\frac{\delta}{u' \cdot \tau_c}$. Below is an example of a kinetic model used for hydrogen explosions. The chemical reaction model is a two-step, two species reaction model where in the first step the reactants react to radicals and no heat is released. The second step is the reaction of the radicals to products and all of the heat is released. The Arrhenius type model was presented by [*Korobeinikov et. al., 1972*]. The chemical kinetics are shown in equation 3.20 and equation 3.21. Equation 3.20 is the induction time model and equation 3.21 is the reaction rate for

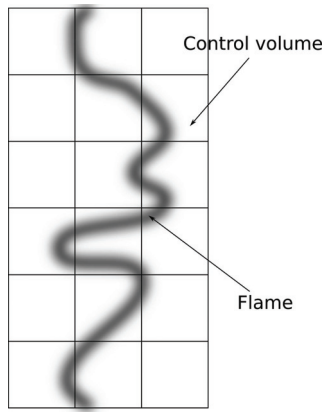

Figure 3.2: A thin flame imposed on a coarse computational mesh.

the heat releasing reaction. The second reaction start when the value $\alpha = \int \frac{1}{\tau} dt$ reaches one.

$$\tau = \left(\frac{d\alpha}{dt}\right)^{-1} = A_\alpha \left(T/p\right) exp\left[-B_\alpha + C_\alpha/T + D_\alpha \left(p/p_{atm}\right)^2 exp\left(E_{a,\alpha}/T\right)\right] \quad (3.20)$$

$$\frac{d\beta}{dt} = -A_\beta p^2 \beta^2 exp\left(-E_{a,\beta}/T\right) + A_\beta p^2 \left(1-\beta\right)^2 exp\left(-\left(E_{a,\beta}/T + q/(RT)\right)\right) \quad (3.21)$$

Where A_β is 1.05·10^{-5} in SI units, $E_{a,\beta}$ is the activation temperature and is 2000 K and q is the change in formation enthalpy and is here 3·10^6 J/kg. A_α is 6.2335·10^{10} Pa/K·s, B_α is 35.1715, C_α is 8530.6 K, D_α is 7.22·10^{-11}, $E_{a,\alpha}$ is 21205 K. These values, except the A_α is from the induction time model presented by Sichel et. al. [*Sichel et. al., 2002*]. Results from this model for high speed flames was presented in [*Vaagsaether and Bjerketvedt, 2007*]. For hydrogen-air the laminar burning velocity is calculated by a model presented by Iijima and Takeno [*Iijima and Takeno, 1984*], equation 3.22 for stoichiometric hydrogen-air.

$$S_L = 2.38\left(1 + 1.54log\left(\frac{p}{p_0}\right)\right)\left(\frac{T}{T_0}\right)^{0.43} \quad (3.22)$$

3.4 Thermodynamics

The constant q appearing in the energy term 3.4 and 3.18 is the change in formation enthalpy from reactants to products. This heat of combustion is calculated by using a thermodynamics package like Cantera [Cantera, n.d.]. In figure 3.3 an example of enthalpy of the reactants and products are plotted as a function of temperature for stoichiometric hydrogen-air combustion. The formation enthalpy used in this model is at 298.15 K. The

real fluid curves are calculated using Cantera and assuming a constant pressure combustion. For the ideal gas curves the heat capacity ratio γ for the reactants is at the initial state of 300 K and the γ for the products is at the adiabatic flame temperature. This is the reason the curves for the ideal gas matches the real gas curves at 300 K for the reactants and at adiabatic flame temperature for the products. The type of process determines the equilibrium composition and temperature and the γ and heat of formation, ΔH_f, is dependent on the process. A constant volume process will have higher temperature in the products than a constant pressure process and the values of C_p and C_v is dependent on the reaction. In the method described here these are frozen heat capacities which means that the heat capacities are calculated from the product state with a constant composition as seen in equations 3.23 and 3.24.

$$C_p = \left(\frac{\partial H}{\partial T}\right)_{p,N} \tag{3.23}$$

$$C_v = \left(\frac{\partial U}{\partial T}\right)_{V,N} \tag{3.24}$$

The enthalpy in the reactants and products is calculated as equations 3.25 and 3.26.

$$\Delta H_R = \int_{T_{ref}}^{T_0} C_p dT + \Delta H^0_{f,R} \tag{3.25}$$

$$\Delta H_P = \int_{T_{ref}}^{T_{ad}} C_p dT + \Delta H^0_{f,P} \tag{3.26}$$

For a constant pressure process the change in formation enthalpy is calculated as in 3.27 since the enthalpy is constant, $\Delta H_R = \Delta H_P$.

$$\Delta H_f = \int_{T_{ref}}^{T_{ad}} C_p dT - \int_{T_{ref}}^{T_0} C_p dT \tag{3.27}$$

Where T_{ref} is the reference temperature, usually 298.15 K, T_0 is the temperature of the reactants, T_{ad} is the temperature of the products. $\Delta H^0_{f,R}$ is the formation enthalpy of the reactants at reference temperature and $\Delta H^0_{f,P}$ is the formation enthalpy of the products at reference temperature. For ideal gas the enthalpy is calculated as in equation 3.28.

$$\Delta H_{ideal} = \frac{\gamma p}{\rho\left(\gamma - 1\right)} \tag{3.28}$$

As a study of the consequence of the different methods for choosing different values for γ a short comparison with other studies using a similar approach is presented. These are studies of flame acceleration and detonations in stoichiometric hydrogen-air at 1 atm and 293 K. [*Strehlow, 1991*] reported heat of reaction corresponding to a constant γ for detonations to be 4 MJ/kg and 1.173. This was based on curve fitting of the Hugoniot curve for equilibrium composition at the CJ-state. [*Gamezo et. al., 2008*] used q = 5 MJ/kg and γ = 1.172 which was matched to laminar flame velocity or detonation cell size. Results from the two methods are compared with results from the method presented in this chapter with heat of reaction q = 3 MJ/kg, reactant γ = 1.4 and product γ = 1.242.

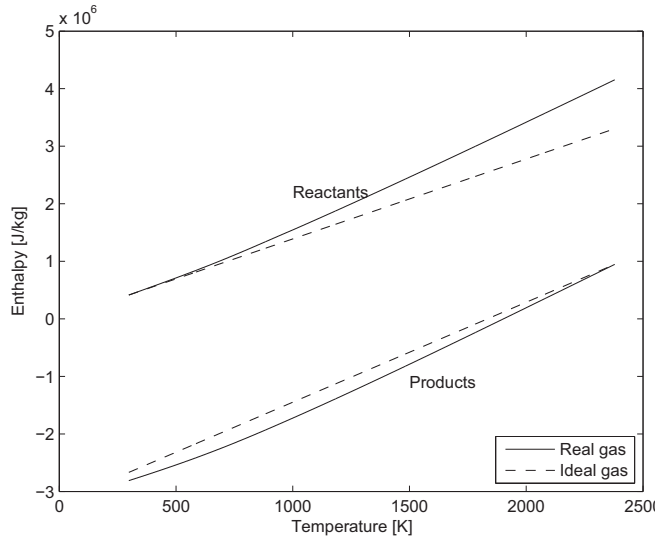

Figure 3.3: Enthalpy curves for products and reactants for both real fluid and ideal gas. This is for a constant pressure reaction of stoichiometric hydrogen-air at 300 K and 1 atm.

For the three different cases the Riemann solver from appendix B calculates the states in front of and behind a flame. Figure 3.4 shows the wave characteristics in the reactants and the products. The state U_R is in front of the flame and U_L is behind the flame. The initial condition is 1 atm on both sides and zero velocity, the density is 0.858 kg/m^3 to the right and 0.15 kg/m^3 to the left. Figures 3.5, 3.6 and 3.7 shows the comparison of pressure, density and gas velocity as a function of burning velocity right in front of (U_0) and behind (U_I) the flame for the three different methods and figure 3.8 shows the flame speeds.

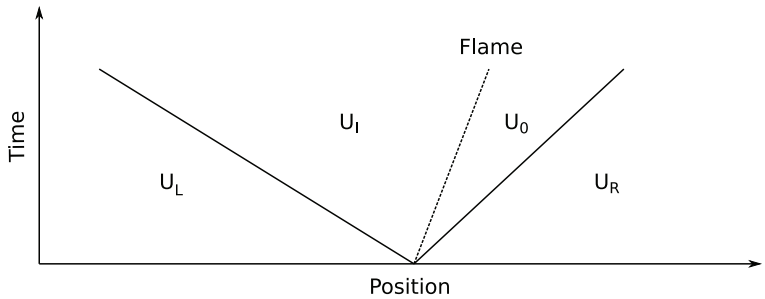

Figure 3.4: Schematics of the flame setup used for comparison for different models. The flame sends pressure waves into the reactants and products.

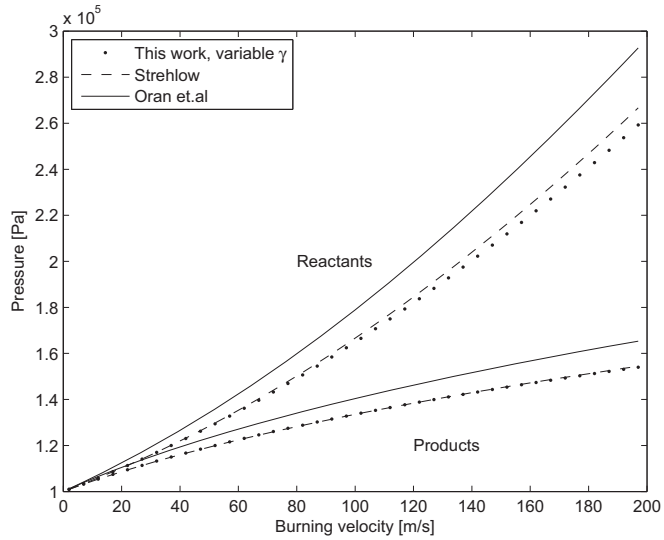

Figure 3.5: Comparison of pressure in the shocked reactants and the shocked products for the three different models.

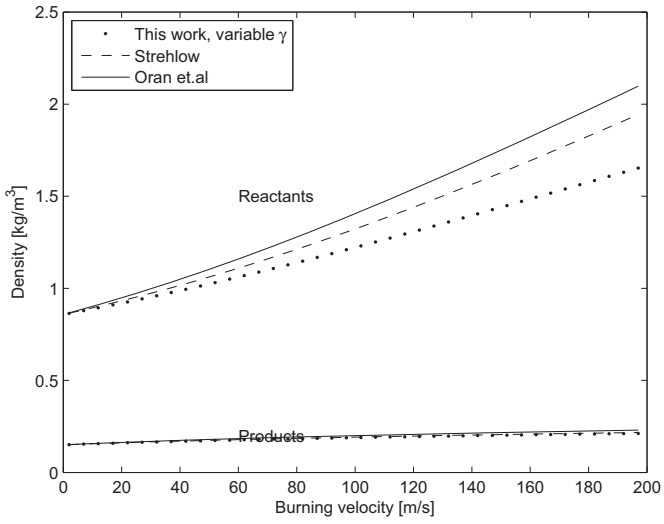

Figure 3.6: Comparison of density in the shocked reactants and the shocked products for the three different models.

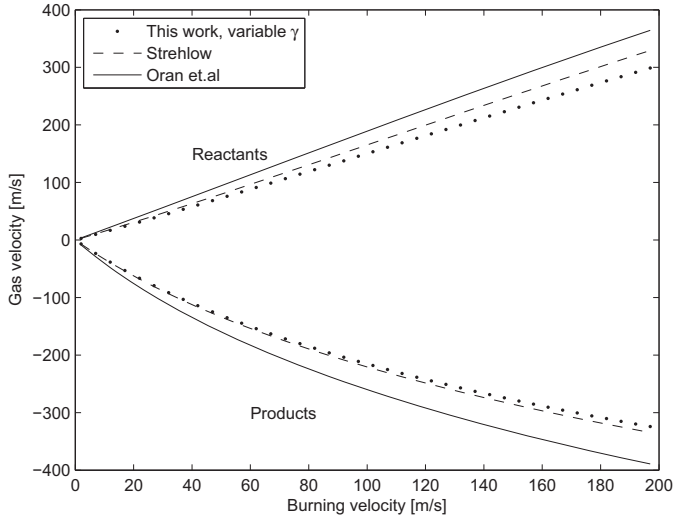

Figure 3.7: Comparison of velocity in the shocked reactants and the shocked products for the three different models.

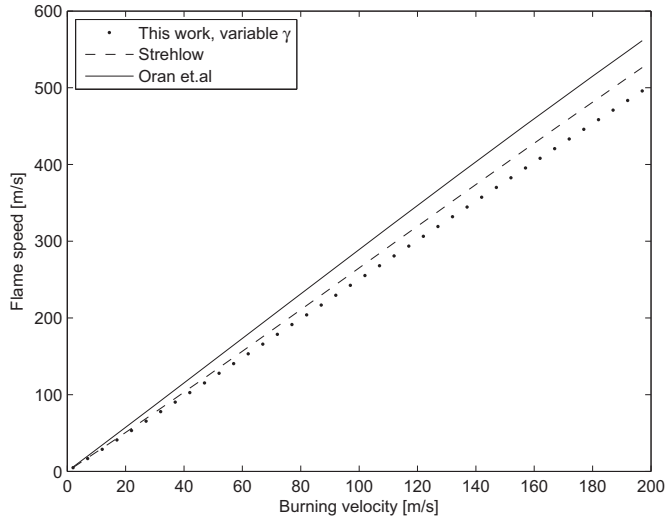

Figure 3.8: Comparison of flame speed for the three different models.

Discussion

Using the ideal gas law to model the internal energy and using a constant γ restricts the calculation to constant heat capacity. By using different γ for the reactants and the products the heat capacities are assumed different for these states even if the temperature-dependence in each gas is not handled. For higher temperatures in the reactants produced by for instance shock waves the internal energy will be modelled incorrectly. The deviation is seen in figure 3.3, where the difference in enthalpy in the reactants between the ideal Gauss and real gas increases as the temperature increases. For stoichiometric hydrogen-air this is not too critical since this mixture starts to react at about 900 K, but for other mixtures it might give larger differences. By comparing three different methods of choosing thermodynamic properties for simulating explosions we see that the Strehlow method and the variable γ method used here produce similar results for pressure and velocities. The constant γ method of [*Gamezo et. al., 2008*] produce higher pressures and flame speeds due to the high value of heat of combustion.

3.5 JWL equation of state

When calculating the expansion of detonation products from high explosives the ideal gas law is not well suited. The only gas dependent coefficient in the ideal gas law is the heat capacity ratio γ. Using a constant γ does not take into account temperature changes in the heat capacities or any change in equilibrium due to temperature changes. The Jones-Wilkins-Lee (JWL) [*Lee et. al., 1968*] equation of state express the pressure as a function of internal energy and expansion of the high explosive products. Equation 3.29 shows the general form of the JWL eos.

$$p = \Omega\frac{e}{\hat{\rho}} + A\left(1 - \frac{\Omega}{R_1\hat{\rho}}\right)\exp\left(-R_1\hat{\rho}\right) + B\left(1 - \frac{\Omega}{R_2\hat{\rho}}\right)\exp\left(-R_2\hat{\rho}\right) \tag{3.29}$$

Where e is the internal energy, $\hat{\rho}$ is the initial high explosive density over the density, A, B, R_1, R_2 and Ω are constants dependent on the high explosive. Ω behaves like $\gamma - 1$ for ideal gas when the products have expanded to a few times its initial volume. Figure 3.9 compares the JWL eos to the ideal gas law for C4 high explosive. This shows that the JWL behaves like the ideal gas law after the products have expanded to about 1.6 times the initial radius. This value might be different for other types of high explosives.

3.6 FLIC-scheme

TVD-schemes (Total Variation Diminishing) are methods for solving hyperbolic differential equations without producing unstable results. The transient and convective terms of the conservation equations, including the pressure forces, is hyperbolic. A general form of a non-linear hyperbolic equation is shown in equation 3.30 where $\mathbf{Q}$ is the conserved variables and $\mathbf{F}(\mathbf{Q})$ is the convective flux function.

$$\frac{\partial \mathbf{Q}}{\partial t} + \frac{\partial \mathbf{F}(\mathbf{Q})}{\partial x} = 0 \tag{3.30}$$

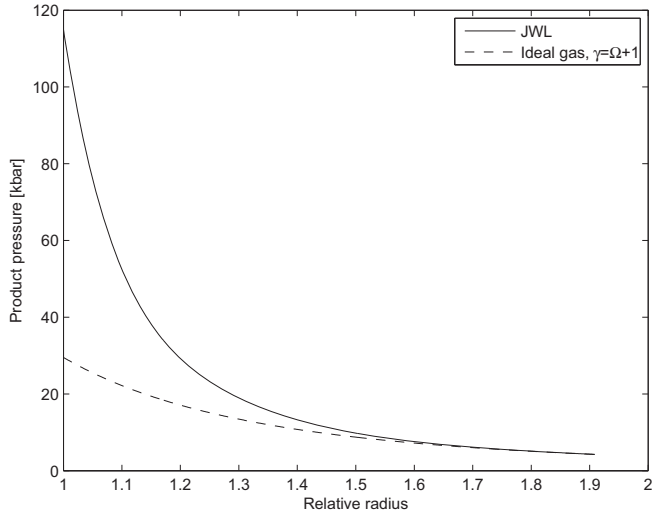

Figure 3.9: Ideal gas law and JWL eos comparison of product pressure in C4 high explosive as a function of product radius assuming the products expands spherically and neglecting work. The heat capacity ratio in the ideal gas law is $\Omega + 1$.

The integration of a hyperbolic differential equation like the one-dimensional Euler equations without sources over a generic control volume i shown in figure 3.10 and over time step Δt gives the result shown in equation 3.31.

$$\mathbf{Q}^{n+1} = \mathbf{Q}^{n} + \frac{\Delta t}{\Delta x}\left(\mathbf{F}_{i-1/2} - \mathbf{F}_{i+1/2}\right) \tag{3.31}$$

Where the superscripts n and n+1 denotes the time at t and t+Δt. Note that the fluxes $\mathbf{F}$ at the interface does not include a superscript for time since the approximation in time may use discrete values from different time-steps. Most numerical schemes for solving propagating waves use an explicit formulation of the fluxes since there is a strict criterion for stability on the time steps both for explicit schemes and for the flow. This criterion is given by the Courant-Friedrich-Levi (CFL) number. For compressible flow the criterion demands that no wave in the system can travel farther than one control volume in one time step. The CFL-number is the ratio of a wave speed to a ”mesh speed” as seen in equation 3.32 and is between 0 and 1. The mesh speed is the mesh length divided by the time step. If the CFL-number is 1 the fastest wave travels one control volume during one time step. By setting a global Courant number based on the fastest wave speed in the computational domain the time step can be determined.

$$C_{CFL} = \frac{c + u}{\frac{\Delta x}{\Delta t}} \tag{3.32}$$

Another property of higher order numerical schemes used for compressible flow simulations is the total variation diminishing (TVD) capability. For stable solutions the scheme

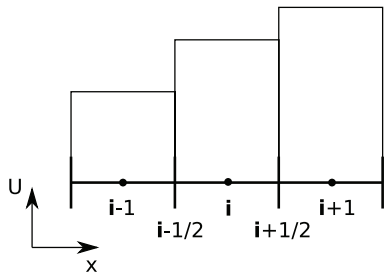

Figure 3.10: Principle of a computational mesh with discrete nodes and piecewise constant values.

must not introduce spurious oscillations near large gradients and the total variation of the solution must not increase. This property is usually introduced through some form of controlled numerical diffusion.

The FLIC scheme, [*Toro, 1999*], is a 2nd order accurate centered flux-limiter scheme that combines the 1st order accurate FORCE scheme and the 2nd order Richtmyer version of the Lax-Wendroff scheme. The FORCE flux is the arithmetic mean of the Richtmyer flux and the Lax-Friedrich flux. The 1st order Lax-Friedrich flux is defined in equation 3.33. The simplest form of these schemes are for one dimension. In this thesis the 1-dimensional version is used and solved with the fractional step method. In the presentation of this scheme 3.34 to 3.37 the conserved variable vector $\mathbf{Q}$ and the flux vector $\mathbf{F}$ from the conservation equations are used.

$$\mathbf{F}^{LF}_{i+\frac{1}{2}} = \frac{1}{2}[\mathbf{F}(\mathbf{Q}_i) + \mathbf{F}(\mathbf{Q}_{i+1})] + \frac{1}{2}\frac{\Delta x}{\Delta t}[\mathbf{Q}_i - \mathbf{Q}_{i+1}] \tag{3.33}$$

The 2nd order Richtmyer flux is defined by the intermediate states of the conserved variables as shown in equation 3.35.

$$\mathbf{Q}^{RI}_{i+\frac{1}{2}} = \frac{1}{2}[(\mathbf{Q}_i) + (\mathbf{Q}_{i+1})] + \frac{1}{2}\frac{\Delta t}{\Delta x}[\mathbf{F}(\mathbf{Q}_i) - \mathbf{F}(\mathbf{Q}_{i+1})] \tag{3.34}$$

$$\mathbf{F}^{RI}_{i+\frac{1}{2}} = \mathbf{F}(\mathbf{Q}^{RI}_{i+\frac{1}{2}}) \tag{3.35}$$

$$\mathbf{F}^{FORCE}_{i+\frac{1}{2}} = \frac{1}{2}[\mathbf{F}^{LF}_{i+\frac{1}{2}} + \mathbf{F}^{RI}_{i+\frac{1}{2}}] \tag{3.36}$$

And the full FLIC scheme can be written as equation 3.37. Where ϕ is the flux limiter.

$$\mathbf{F}^{FLIC}_{i+\frac{1}{2}} = \mathbf{F}^{FORCE}_{i+\frac{1}{2}} + \phi_{i+\frac{1}{2}}[\mathbf{F}^{RI}_{i+\frac{1}{2}} - \mathbf{F}^{FORCE}_{i+\frac{1}{2}}] \tag{3.37}$$

The flux limiters control the order of the scheme. For areas where the solution is smooth the scheme is 2nd order accurate or close to 2nd order. For areas with discontinuous solutions the scheme is 1st order accurate. A measure of the smoothness of the solution is needed to construct the flux limiter. Equations 3.38 to 3.42 shows how the

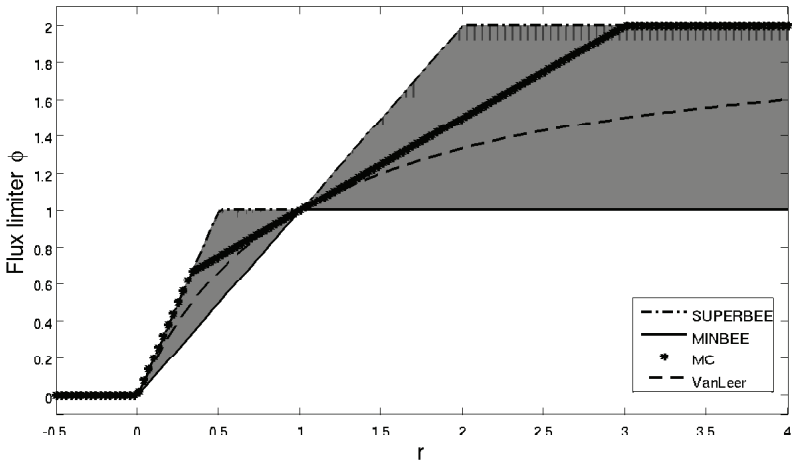

Figure 3.11: Graphic representation of the flux limiters, ϕ as a function of gradient r. The shaded area is the TVD region for the Euler equations.

slopes, r, in the solution are calculated. For these equations Q is a variable that includes all wave types such as total energy or density.

$$r^L_{i+\frac{1}{2}} = \frac{\delta Q_{i-\frac{1}{2}}}{\delta Q_{i+\frac{1}{2}}} \tag{3.38}$$

$$r^R_{i+\frac{1}{2}} = \frac{\delta Q_{i+\frac{3}{2}}}{\delta Q_{i+\frac{1}{2}}} \tag{3.39}$$

Where the differences in the variable Q is defined as:

$$\delta Q_{i-\frac{1}{2}} = Q_i - Q_{i-1} \tag{3.40}$$

$$\delta Q_{i+\frac{1}{2}} = Q_{i+1} - Q_i \tag{3.41}$$

$$\delta Q_{i+\frac{3}{2}} = Q_{i+2} - Q_{i+1} \tag{3.42}$$

Different kinds of flux limiters are constructed based on a stability region for the slopes. The different flux limiters are displayed in figure 3.11 graphically. These limiters are constructed based on the TVD region bounded by the SUPERBEE and MINBEE limiters. The SUPERBEE limiter is the least diffusive limiter possible and may induce small oscillations around strong gradients and MINBEE is the most diffusive limiter. The shaded area between these two limiters is the stable region of the limiters. The limiter used for all calculations in this thesis is the MC-limiter [*LeVeque, 2002*].

SUPERBEE

$$\phi = \begin{cases} 0 & \text{if } r < 0 \\ 2r & \text{if } 0 \leq r < \frac{1}{2} \\ 1 & \text{if } \frac{1}{2} \leq r < 1 \\ min(2, \phi_g + (1-\phi_g)r & \text{if } r \geq 1 \end{cases}$$

MC-limiter

$$\phi = \begin{cases} 0 & \text{if } r < 0 \\ 2r & \text{if } 0 \leq r < \frac{1}{3} \\ min(2, 0.5 + \frac{r}{2}) & \text{if } r \geq \frac{1}{3} \end{cases}$$

VanLeer

$$\phi = \begin{cases} 0 & \text{if } r < 0 \\ \frac{2r}{1+r} & \text{if } 0 \leq r < 1 \\ \phi_g + 2(1-\phi_g)\frac{r}{1+r} & \text{if } r \geq 1 \end{cases}$$

MINBEE

$$\phi = \begin{cases} 0 & \text{if } r < 0 \\ r & \text{if } 0 \leq r < 1 \\ 1 & \text{if } r \geq 1 \end{cases}$$

The flux limiter for the inter cell boundary $i + 1/2$ is chosen as the smallest limiter value of the left and right slopes, equation 3.43.

$$\phi_{i+\frac{1}{2}} = min(\phi(r^L_{i+\frac{1}{2}}), \phi(r^R_{i+\frac{1}{2}})) \tag{3.43}$$

3.7 Fractional step method

The fractional step method solves higher dimensional equations and source terms with one-dimensional numerical schemes. An example with a two-dimensional hyperbolic equation with a source term is shown in equation 3.44.

$$\frac{\partial \mathbf{Q}}{\partial t} + \frac{\partial \mathbf{F}(\mathbf{Q})}{\partial x} + \frac{\partial \mathbf{G}(\mathbf{Q})}{\partial y} = \mathbf{J} \tag{3.44}$$

This equation is split into three sub-problems with the change of $\mathbf{Q}$ in time term is common in all sub-problems as is seen in equations 3.45 to 3.47.

$$\frac{\partial \mathbf{Q}}{\partial t} + \frac{\partial \mathbf{F}(\mathbf{Q})}{\partial x} = \mathbf{0} \tag{3.45}$$

$$\frac{\partial \mathbf{Q}}{\partial t} + \frac{\partial \mathbf{G}(\mathbf{Q})}{\partial y} = \mathbf{0} \tag{3.46}$$

$$\frac{\partial \mathbf{Q}}{\partial t} = \mathbf{J} \tag{3.47}$$

The solution of equation 3.45 is used as initial conditions for equation 3.46 and the solution of equation 3.46 is used as initial condition for equation 3.47. This method has truncation error of first order. A more thorough discussion on the fractional step method can be read in [*LeVeque, 2002*].

3.8 Total algorithm

Figure 3.12 shows an overview of the total algorithm for using the FLIC-scheme with the fractional step method to solve the models presented above. The metod is implemented in Matlab [*The MathWorks, n. d.*]. The initial conditions are set for all variables in all control volumes before the time stepping starts. A time step is calculated using the global CFL-number, usually set to 0.9. The burning velocity is calculated from the temperature, pressure and turbulence field before each time the algorithm solves the convective part using the FLIC-scheme. The gradients of β and velocity is calculated from the intermediate states in the Richtmyer scheme. These gradients are needed for the source terms in the combustion model and turbulence model respectively.

Figure 3.12: Algorithm chart.

Chapter 4

Basic tests of the method

4.1 Test of numerical scheme

This chapter presents siulation results from well known tests of numerical schemes for compressible, inviscid flow. For all one-dimensional tests the domain is length 1 and is discretized by 100 control volumes. [*Liska and Wendroff, 2003*] and [*Toro, 1999*] have performed several tests for different numerical schemes and the tests shown here are from these two studies. Table 4.1 summarize the initial conditions for the tests used as verification of the numerical scheme. The three one-dimensional tests have the discontinuity between the left and right state at x = 0.5. The 2D test is a cylindrical test where the left state is the state at radius smaller than 0.4. The domain is square with side lengths of 2.

Test 1 is a modified Sod's test. For comparison test 1 is also solved with the 3. order PPM-MUSCL-Hancock (PPM-MH) scheme with an analytical Riemann solver and the Random Choice Method. Figure 4.1 shows the comparison of density at t=0.25 for the three methods. The density contains all wave families and is a good variable for comparing the schemes performance. The RCM is used for comparison for several cases since the RCM does not have any numerical diffusion the discontinuities are not solved as a continuous gradient. Test 2 is called the 123 test. It consists of two rarefaction waves that produces low pressure and density. Figure 4.2 shows the specific internal energy $\left(e = \frac{p}{\rho(\gamma-1)}\right)$ for the exact solution and the FLIC solution at t = 0.15, figures 4.3 and 4.4 are pressure and density. The internal energy is the variable most schemes has problems simulating correctly for this test. Test Noh is a test by [Noh, 1987] for testing numerical schemes on their ability to handle infinitely strong shocks. Most codes will set the minimum pressure to 10^{-6}. Figure 4.5 shows density for for the Noh test at t = 2. Test 2D is a two-dimensional test where a cylinder of high pressure and density expands cylindrically. Figure 4.6 shows the density along the radius at t = 0.25 and figure 4.7 shows the entire density field also at t = 0.25.

Table 4.1: Initial conditions for tests of the numerical scheme.

Test	ρ_L	u_L	p_L	ρ_R	u_R	p_R	γ
1	1.0	0.75	1.0	0.125	0.0	0.1	1.4
2	1.0	-2.0	0.4	1.0	2.0	0.4	1.4
Noh	1.0	1.0	0.0	1.0	-1.0	0.0	5/3
2D	1.0	0.0	1.0	0.125	0.0	0.1	1.4

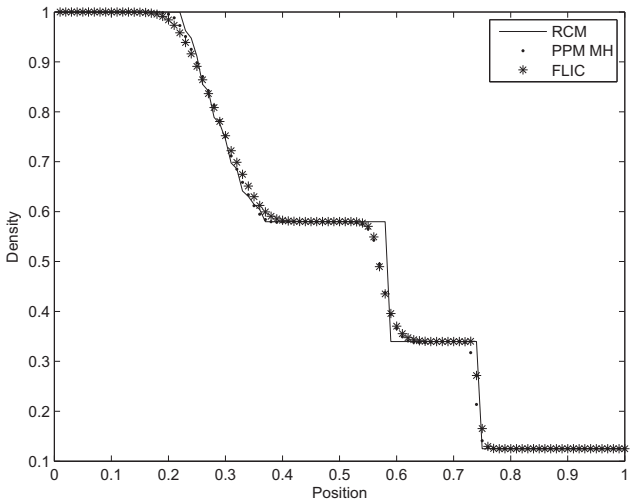

Figure 4.1: Comparison of density for test 1 at t=0.25.

Discussion

The simulation results from test 1 show that the FLIC scheme and PPM-MH scheme has similar performance. Both have numerical diffusion that smooths the discontinuities over a few control volumes and the numerical diffusion acts stronger on the contact discontinuity than on the shock front. The PPM-MH simulates the head and tail of the rarefaction wave somewhat better than the FLIC scheme. This is because PPM-MH is a higher order method and the flux limiting produce higher order fluxes where the solution is continuous. [*Liska and Wendroff, 2003*] showed that many schemes have problems with test 2 where all schemes they tested showed the same type of discrepancy as seen in figure 4.2 where the schemes are unable to produce the minimum region in the internal energy. Even though pressure and density are close to the analytical solution there are large deviations in the internal energy due to numerical diffusion which in this case erroneously produce entropy. In the solution algorithm the numerical diffusion is first applied to the mass equation to update the density then the momentum equation to get the new velocity and finally the energy equation for pressure. The density and velocity from the new time step is used to calculate the new pressure and artificial viscosity is effectively applied three times to

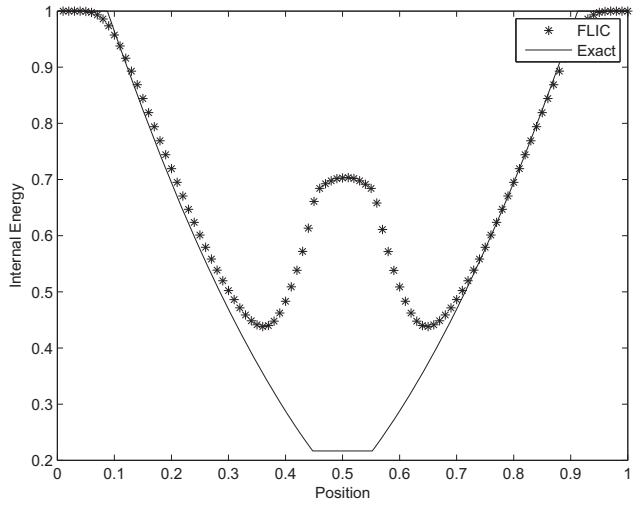

Figure 4.2: Comparison of internal energy for test 2 at t=0.15.

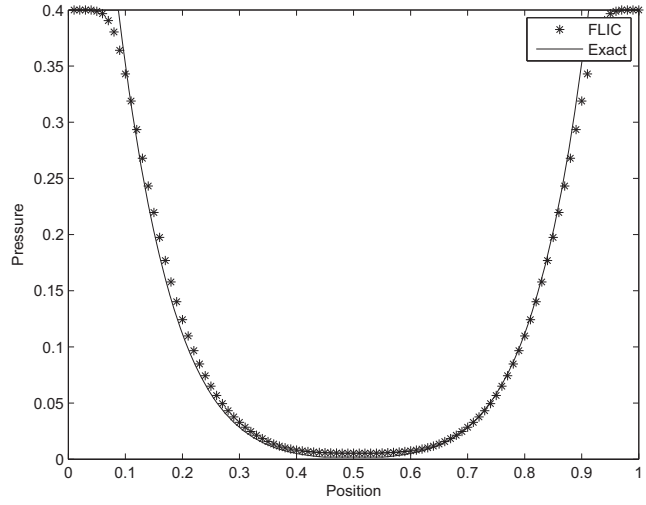

Figure 4.3: Comparison of pressure for test 2 at t=0.15.

the energy equation. The FLIC scheme handles the Noh test satisfyingly but there is a small dip in the density in the center of the domain due to numerical diffusion. Some schemes have larger problems with this case and even too much numerical diffusion at

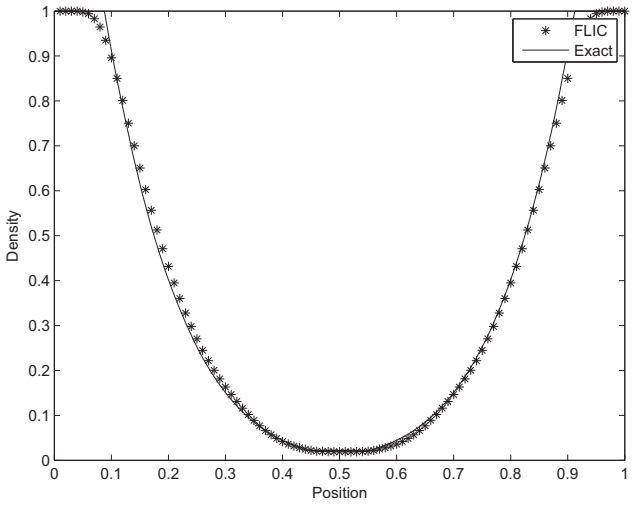

Figure 4.4: Comparison of density for test 2 at t=0.15.

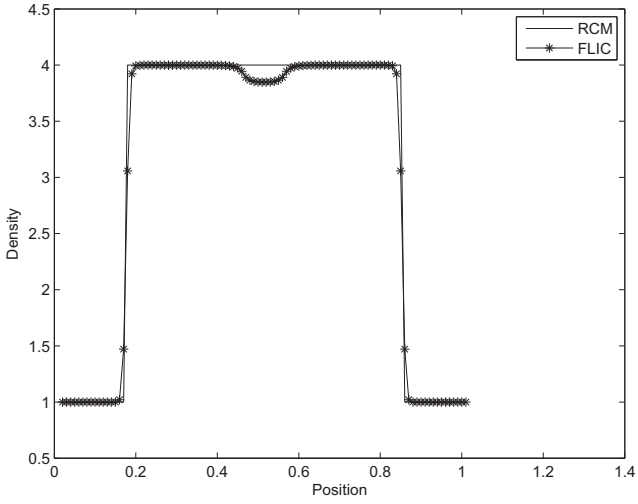

Figure 4.5: Comparison of density for the Noh test at t=2.

the shock front [*Liska and Wendroff, 2003*]. Results from the 2D test show increased numerical diffusion compared to the similar 1D test 1. This is due to numerical diffusion in two directions and even inaccuracies in the fractional step method which is only a 1.

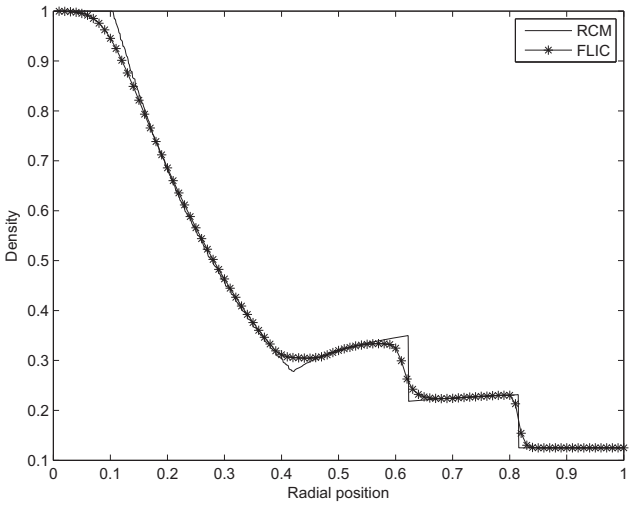

Figure 4.6: Comparison of density for the 2D test at t=0.25 along the radius.

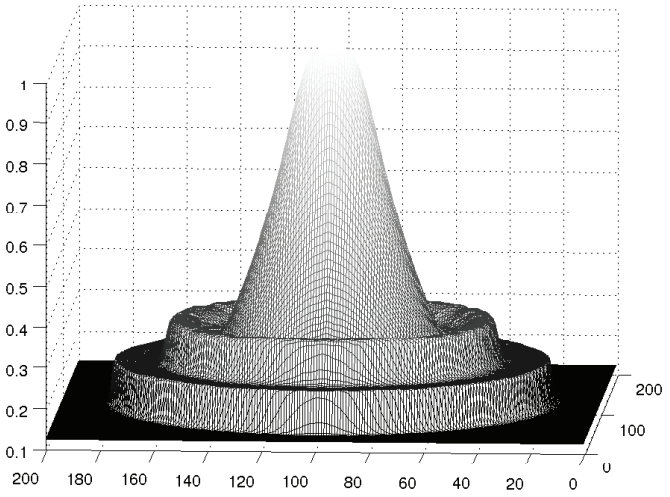

Figure 4.7: Density from the 2D test at t=0.25, simulated by the FLIC-scheme.

order approximation.

4.2 Test of combustion model

As a test of the behavior of the combustion model presented in chapter 3.3 a one dimensional flame is simulated with constant burning velocity. The Random Choice Method with the very thin flame Riemann solver (appendix B) is used for comparison. The gas in this test is typical hydrogen-air mixture with γ_u = 1.4, γ_b = 1.241, q = 3·10^6 J/kg, T_0 = 293 K, the burning velocity is constant 40 m/s, which is assumed for a turbulent flame in a pipe where the burning velocity includes the total flame area. The gas is ignited at the left side, which is closed. Both methods use 1000 control volumes. Figure 4.8 shows the pressure along the computational domain for both the FLIC-method and the RCM with the very thin flame Riemann solver. In figure 4.9 the comparison of the velocity for both methods can be seen.

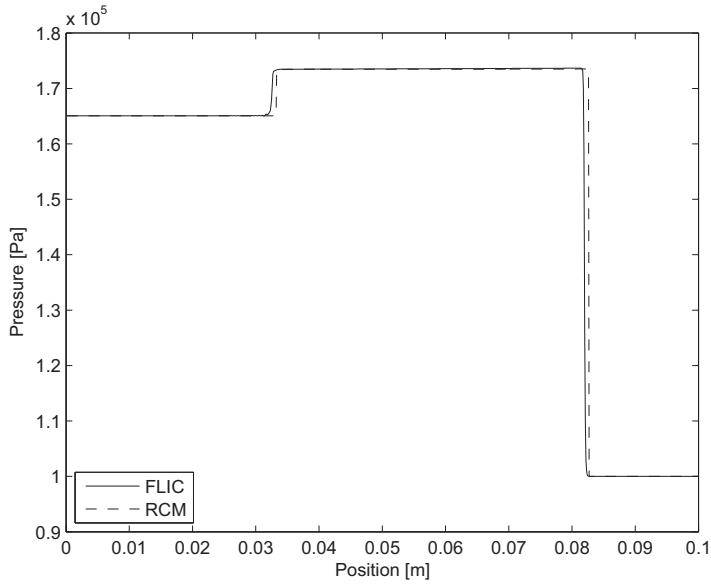

Figure 4.8: Simulated pressure for FLIC and RCM. The time is 1.6·10^{-4} and the flame is located at about 0.035 m.

Discussion combustion model

The RCM with the very thin flame Riemann solver should produce exact results for this simple case with a constant burning velocity. The combustion model presented here gives the same pressure and velocity as the RCM. For this one-dimensional case the combustion model is only using the progress variable gradient rate and the kinetic part is virtually zero since the temperature in front of the flame is low.

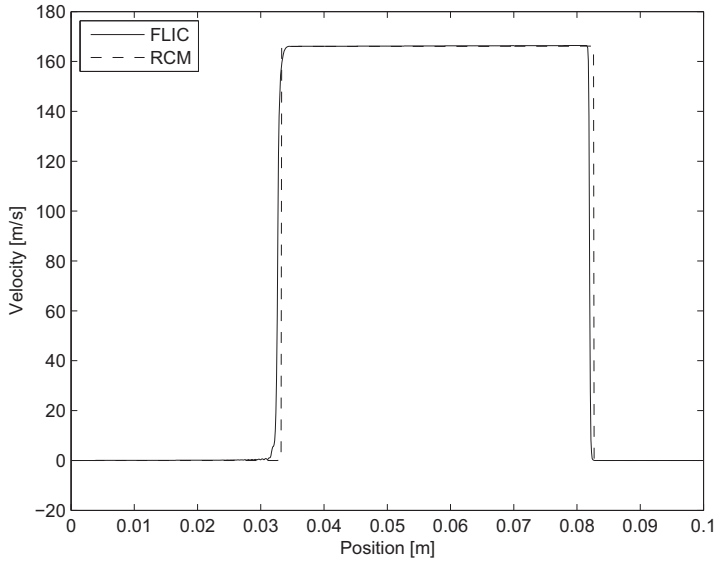

Figure 4.9: Comparison of pressure between FLIC and RCM. The time is $1.6{\cdot}10^{-4}$ and the flame is located at 0.035 m.

4.3 1D Detonation simulations

This section presents results and discussions of simulations of one-dimensional detonation problems where detonation in two different gasses is simulated. The first gas has only one reaction rate which is exothermal and the second gas has two rates where one rate is modelling the isothermal induction reaction and the other rate models the exothermal reaction of radicals to products.

1D Detonation simulation with one step reaction kinetics

The numerical simulations presented here are typical simple benchmark tests for numerical methods on their abilities to handle unstable detonations. It is the same model gas that Erpenbeck used in his study of instabilities in detonations and has been used in several other studies [*Bourlioux and Majda, 1992*], [*Fickett and Davies, 1979*]. The reactive Euler equations are solved with a single step forward reaction rate, as shown in equation 4.1. The unreacted non-dimensional pressure and density is 1 and the temperature is p/ρ.

$$\frac{d\beta}{dt} = -\beta K_0 exp\left(-\frac{T_a}{T}\right) \tag{4.1}$$

To determine K_0 so that half reaction length is one length unit equation 4.1 is transformed from describing the change of β in time to a change in space. The transformed

coordinate system is relative to the detonation front and the positive spatial direction is from the shock into the reaction zone as seen in equation 4.2.

$$\frac{dx}{dt} = D - u(x) \tag{4.2}$$

Where $u(x)$ is the particle velocity and D is the detonation velocity.

$$\frac{d\beta}{dx} = -\frac{\beta K_0}{D - u(x)} exp\left(-\frac{T_a}{T(x)}\right) \tag{4.3}$$

Equation 4.3 is the transformed reaction rate and is solved iteratively for K_0 at β = 0.5 for x = 1.

Two factors that influence the stability of this system is the activation energy, T_a, and the overdrive of the detonation, f, defined in equation 4.4.

$$f = \left(\frac{D}{D_{CJ}}\right)^2 \tag{4.4}$$

[*Fickett and Wood, 1966*] reported a f-T_a diagram, shown in figure 4.10 for q = 50 and γ=1.2 where the stable and unstable areas are marked.

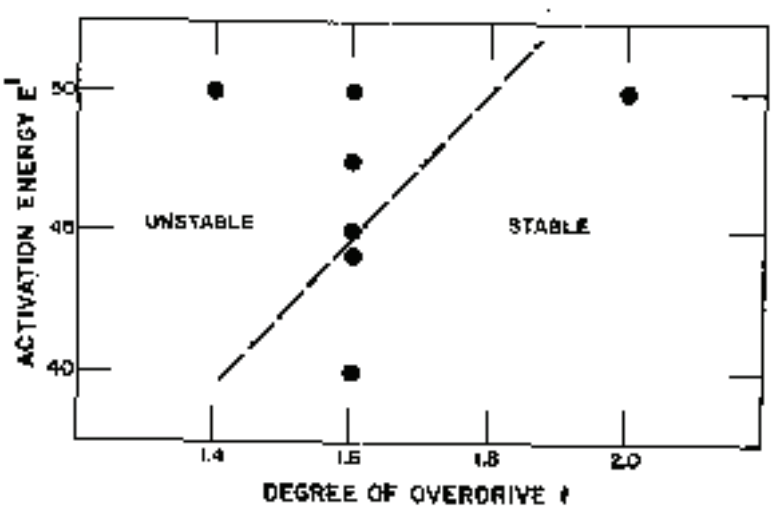

Figure 4.10: Stability boundary for γ=1.2 and q=50, [*Fickett and Wood, 1966*].

Results

Figure 4.11 shows the effect of spatial resolution on the pressure just behind the shock front of a traveling detonation wave for a simulation where q = 50, γ = 1.2, f = 1.6 and T_a = 50. According to the stability regions this should be an unstable detonation. [*Erpenbeck, 1969*] calculated that the maximum pressure peaks here is 101$\pm$0.2. The ZND theory gives a constant pressure peak of 67.3. Three different spatial resolutions are shown for testing the grid dependency in the simulation. The length and time scale is half the reaction thickness and half reaction time. The spatial resolutions used is 2, 5 and 10 volumes pr. half reaction length.

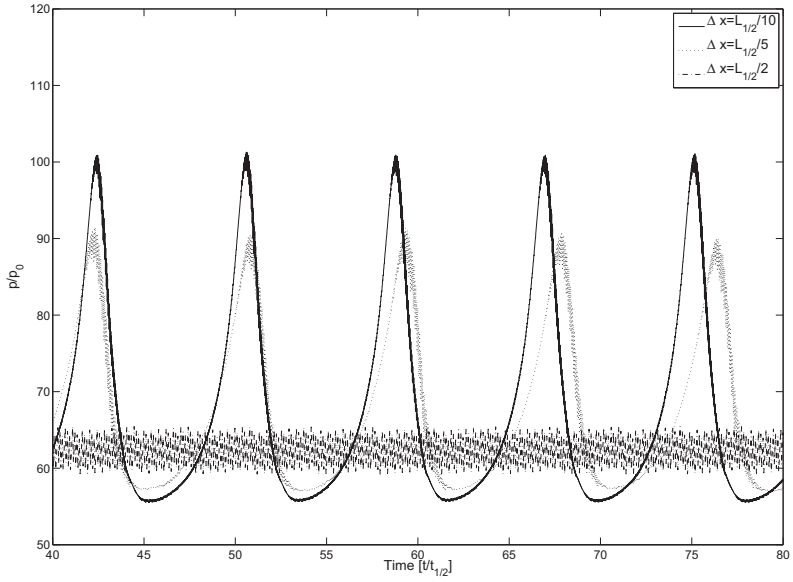

Figure 4.11: Simulated shock pressure results for 2, 5 and 10 computational cells pr. half reaction thickness.

1D Detonation simulation with two step reaction kinetics

To introduce a longer reaction zone by an isothermal reaction in an induction zone a new reaction variable α is solved. Where α is between 0 and 1, where 0 is reactants and 1 is radicals. This reaction does not release energy and only works as a switch so that the second reaction equation does not start until the value of α reaches 1. Equation 4.5 is an

example of a reaction rate of the variable α and is the inverse of the induction time.

$$\frac{d\alpha}{dt} = -K_0 exp\left(-\frac{T_{a,\alpha}}{T}\right) \tag{4.5}$$

Results

Figure 4.12 shows the comparison of two spatial resolutions of an unstable detonation front with two step kinetics. The two grid sizes are 10 and 5 control volumes pr. half reaction thickness of the exothermal reaction. The exothermal reaction rate is the same as for the one step reaction. The reaction rate of the radical reaction is shown in equation 4.5 with $T_{a,\alpha}$ = 50 and K_0 = 1128.7 which gives an induction time of 1 time unit based on the stable von Neumann spike temperature.

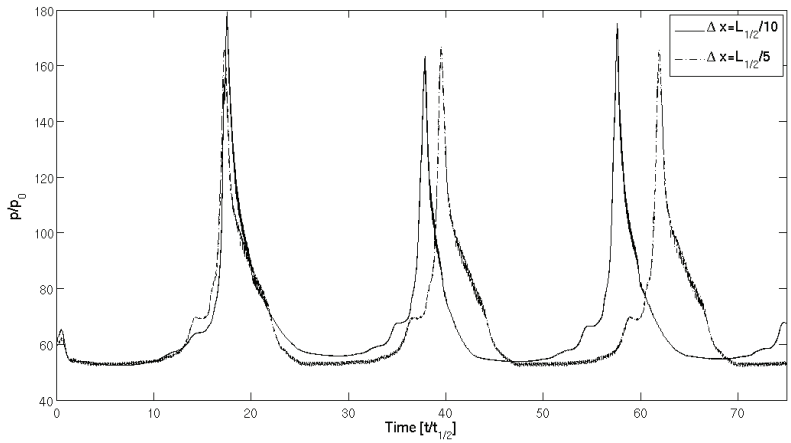

Figure 4.12: Simulated pressure for a two-step reaction. The spatial resolution is 5 and 10 computational cells pr. half reaction length.

Discussion

The calculated half reaction thickness is based on a stable ZND solution but in an oscillating detonation the thickness fluctuates with the states behind the shock front and the thickness is decreased as the temperature behind the shock increases. For the one step chemical reaction the grid resolution influences both the amplitude and frequency of the fluctuating detonation front pressure. The numerical diffusion smooths the shock front over a few control volumes and artificially cools the shocked gas just behind the shock front. For a very coarse calculation this cooling takes place in a relatively large part of the reaction zone and the effect of the oscillating reaction thickness is not seen for two control

Table 4.2: 2D detonation simulation conditions.

	Case 1	Case 2
γ	1.4	1.2
T_a	10	41.3
q	42	50
T_a/T_{vN}	0.8	7.4
f	1	1.2
$\Delta x/\Delta x_{1/2}$	50	20

volumes over half reaction length. It even under-predicts the stable detonation induction zone pressure. These results are also shown by [*Bourlioux and Majda, 1992*] and [*Helzel, 2000*]. [*Helzel, 2000*] proposed a method for counter acting this effect by modifying the numerical scheme. For the two step chemistry the frequency of the fluctuations are influenced by the mesh resolution, but the amplitude is similar for both resolutions shown here. By introducing an isothermal induction zone the flame thickness is increased and the resolution of 5 control volumes over half reaction length is based on the exothermal reaction length. Effectively the induction zone increases the mesh resolution.

4.4 2D detonation simulation

As for one dimensional detonation systems two dimensional detonations can display oscillations in all variables, but the oscillations in two dimensions also form waves that are transverse relative to the leading shock. The interaction of waves from fluctuations in two directions display the cellular structure associated with detonation fronts. Figure 4.13 shows the initial setup for detonation front simulations where the non-reacted gas flows towards the detonation front with the CJ-velocity fron the right boundary. The products flow out the left boundary and the upper and lower boundaries are periodic.

The structure of the oscillating detonation front can be expressed by a relative activation energy T_a/T_{vN}, where T_{vN} is the temperature just behind the shock in the ZND profile, also called the von Neumann spike temperature. For low values of the relative activation energy the cellular pattern of the detonation front is structured. For higher values of activation energy the front becomes more unstructured. The simulations presented here are for two different relative activation energies where T_a/T_{vN} is 0.8 and 7.4. This should produce a structured and an unstructured detonation front as shown by [*Gamezo et. al., 1999*]. The slight overdrive of f = 1.2 in case 2 reduces the relative activation energy from 8.6 at f = 1 to 7.4 at f = 1.2. [*Bourlioux and Majda, 1992*] showed how the regularity of a detonation front increased with increasing overdrive due to increasing von Neuman spike temperature. Table 4.2 summarizes the simulation conditions, $\Delta x/\Delta x_{1/2}$ is the ratio of mesh size to half reaction zone length. For both simulations the initial dimensionless pressure, density and temperature is 1 and with a one-step irreversible reaction in equation 4.1.

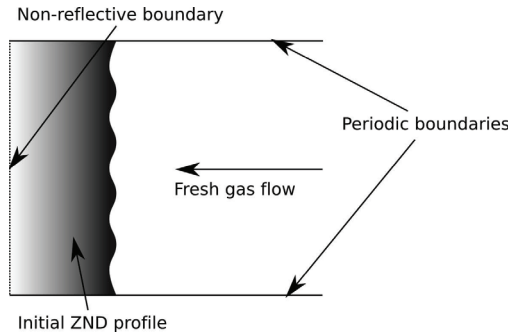

Figure 4.13: Setup for numerical simulation of 2D detonation.

Results

A structured simulated detonation front is shown in figure 4.14 where the unreacted gas has dimensionless pressure of 1, dimensionless density of 1, and γ=1.4. The chemical reaction rate is a one-step forward reaction as described in equation 3.17 with T_a = 10. The dimensionless energy release is q = 50. This front is structured since the activation energy is low, T_a/T_{vN} = 0.8. Figure 4.15 shows a snap-shot from simulations with the unstructured detonation where T_a/T_{vN} = 7.4 and q = 42.

Discussion

It is possible to discern the different waves and instabilities that are characteristic of cellular detonations from the simulation of the structured detonation. The Kelvin-Helmholz-instabilities occur at the slip-line where there is a jump in the density and velocity causing a shear layer, as shown schematically in figure 2.23. The Richtmyer-Meshkov-instability appears where the triple points collide and can be seen in different stages of development behind the shock. The simulation results of the detonation cells show a distinct difference between the two relative activation energies. The heat of reaction for both cases are quite similar, but the activation energy is much higher for the unstructured case. This causes the reaction zone to be more sensitive to temperature and diffraction of the front shock. A reduction in shock strength significantly increases the induction zone and may lead to detonation failure followed by a re-initiation due to collisions of triple points. These re-initiations at the shock front form pockets of unreacted gas behind the front that reacts slowly compared to the reactions in a detonation front. The simulation results of the structured and unstructured detonation front are similar to the results presented by [*Bourlioux and Majda, 1992*] and [*Gamezo et. al., 1999*] with relative activation energies of 0.8 and 7.4. The simulation results of [*Gamezo et. al., 1999*] is seen in figure 2.24.

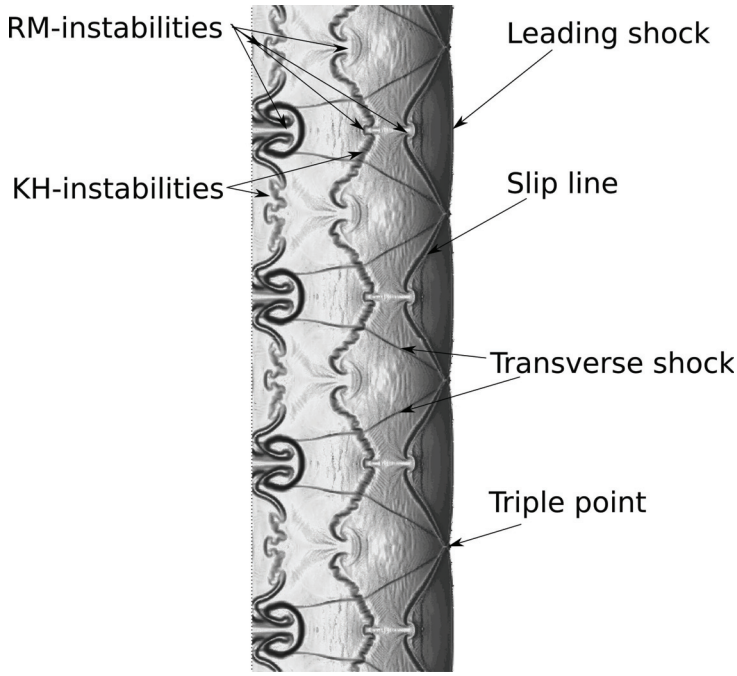

Figure 4.14: Simulation of a structured cellular detonation with T_a = 10, q = 42, f = 1, γ=1.4, T_a/T_{vN}=0.8, case 1 table 4.1.

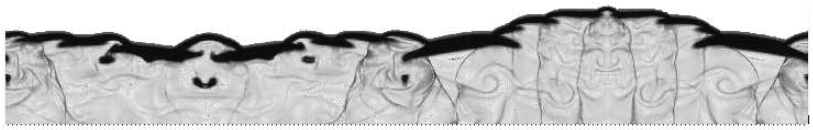

Figure 4.15: Simulation of a unstructured cellular detonation with T_a = 41.3, q = 50, f = 1.2, γ=1.2, T_a/T_{vN}=7.4, case 2 table 4.1.

4.5 Simulation of compressible mixing layer

This section presents a test for validation of the codes ability to handle compressible turbulence with the one-equation turbulence model. Since the code is going to simulate explosions with averaged equations the sub-grid turbulence is important for modelling the turbulent burning velocity. The experiments consists of two parallel streams of air flowing in a channel. The compressibility of a mixing layer is described by a single convective Mach-number which is the stream-wise velocity of the eddies in the mixing layer relative to an average sound speed, equation 4.6.

$$M_c = \frac{U_1 - U_2}{c_1 + c_2} \tag{4.6}$$

Experimental and simulation setup

The experiments by [*Samimy and Elliot, 1990*] are simulated as a validation. In these experiments there is a shear layer in a channel with cross-sectional area of 15 cm x 15 cm. Figure 4.16 shows the side-view of the channel where a splitting plate is separating a supersonic stream (M1) from a subsonic stream (M2). In the experiments discussed in this thesis the subsonic stream has a Mach number of 0.45 and the supersonic stream has a Mach number of 1.8 and the convective Mach number is 0.51. The simulation and experimental mean velocity at 60 and 120 mm from the splitting plate results are compared. These velocities where measured with 2D LDV. The boundary conditions at the splitter plate are from the experiments and set as boundary conditions in the simulations. The computational mesh sizes used in this study is 0.25 mm, 0.5 mm and 1 mm.

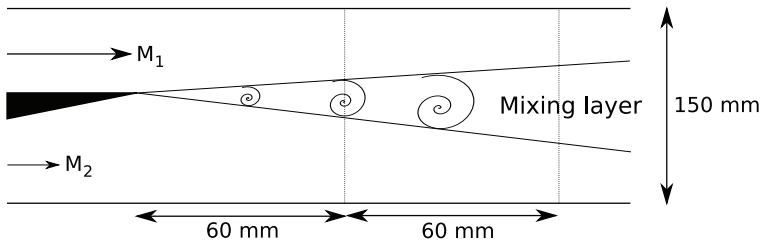

Figure 4.16: Setup of experiments with compressible mixing layer.

Results

Figure 4.17 and 4.18 shows the simulation results with 0.25, 0.5 and 1 mm mesh and experimental results of the mean velocity at positions 60 and 120 mm from the splitting plate.

Discussion

The simulated shear layer profile for 0.25 and 0.5 mm mesh size is similar to the experiments but the results for the 1 mm mesh size shows too large spreading rate of the layer. The shear layer is very thin and the velocity gradients become very high in a thin region and the coarse mesh smooths the gradient increases the spreading rate. In a shear layer like there are coherent structures or vortices that are important for the spreading of the layer. These structures are not necessarily effects of turbulence but might produce turbulence. For a simulation with a coarse mesh the length scale of the structures might be too large and produce an artificially large spreading rate. The number of control volumes over the mixing length thickness can be a parameter that shows how well the simulation captures

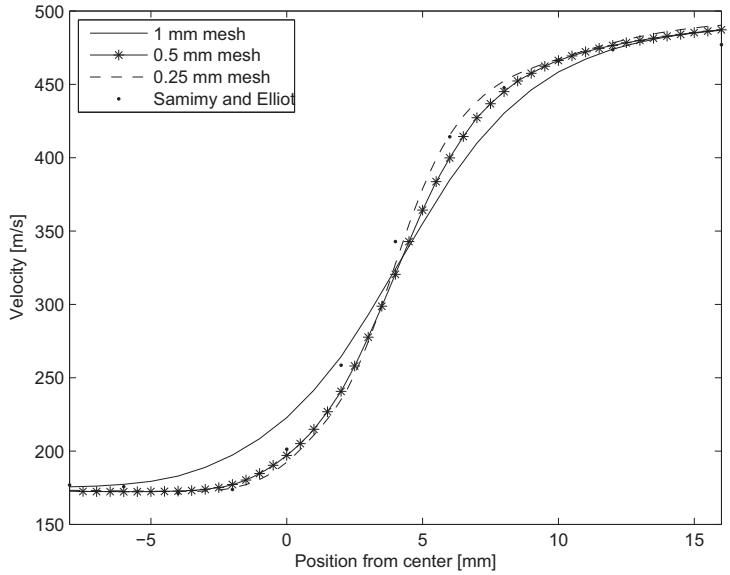

Figure 4.17: Velocity profile for M_c = 0.51 at 60 mm from splitting plate for experiments and simulations with 0.25 mm, 0.5 mm and 1 mm mesh resolution.

the phenomena. The spreading of the velocity gradients will also spread the modelled turbulence and introduce too large momentum diffusion in areas where the shear rate is small in the experiments.

4.6 Simulations of blast from high explosives

This chapter describes tests of the numerical scheme for blast from high explosives. The simulations are of realistic cases and the results are compared with experimental data. The simulations does not take into account any reactions occurring as the high explosive detonates but simulates the shock propagating in air and high explosive products. The solver is the FLIC-scheme with the JWL equation of state to model the thermodynamics in the high explosive products. Two different simulations are shown one in two dimensions of a free field detonation of C4 high explosive and the other is in three dimensions in a generic building.

4.6.1 Free field tests 2D simulation

The experiment by [*Langberg et. al., 2004*] is a high explosive charge of 2 liters C4 placed in a free field at 1 m above ground with pressure transducers at distances 4 m, 5 m, 6 m and 10 m from the center of the blast.

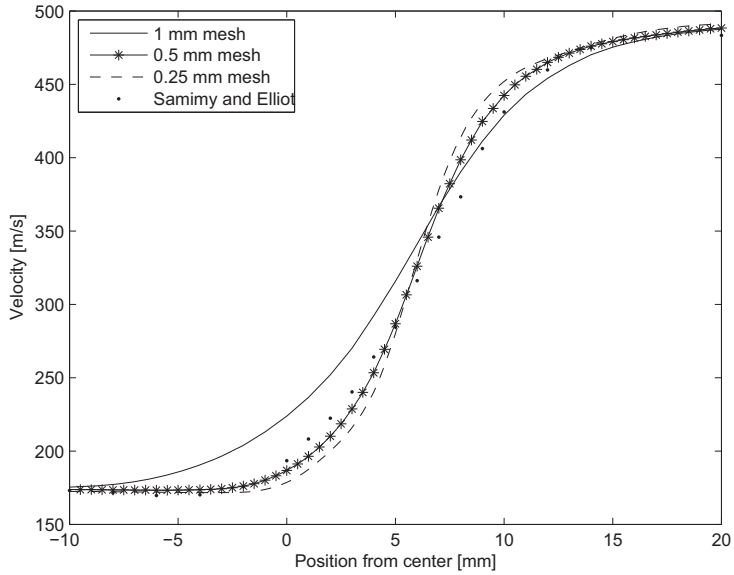

Figure 4.18: Velocity profile for M_c = 0.51 at 120 mm from splitting plate for experiments and simulations with 0.25 mm, 0.5 mm and 1 mm mesh resolution.

Simulation conditions

The numerical simulation is set up as a 2D domain in axisymmetric cylindrical coordinates where one edge of the domain is the symmetric central axis and one edge is the ground as is seen in figure 4.19. The two other boundaries are non-reflective. Only the pressure transducers at 4 m and 10 m are discussed here. The mesh size is constant 0.08 m. The initial conditions for the high explosive charge is determined by assuming the condensed matter is reacted to gas in the same initial volume as the charge. The internal energy from the high explosive is set in the JWL eos and the solution strategy is to solve a small area around the charge with very fine mesh and then map the solution onto a coarser mesh for the entire domain. The ground boundary is full slip and no boundary layer is formed and no topological variations are included. The temperature of the initial non-compressed air is unknown but is assumed to be 288 K. The temperature influences the speed of the blast wave and the assumed value may be a source of error.

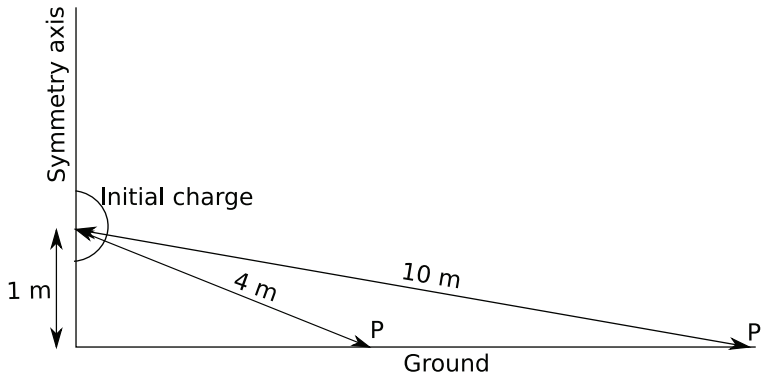

Figure 4.19: Case setup for free-field blast from 2 liters C4. P are pressure transducers.

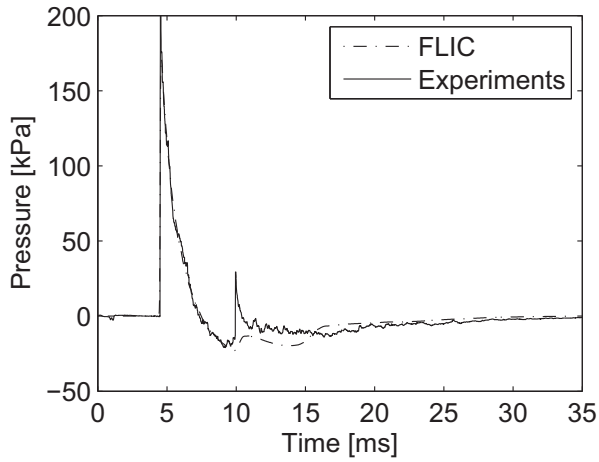

Figure 4.20: Pressure history at 4 m from center of charge comparison with experiments and simulations.

Results and discussion

The results are compared for pressure and impulse pr. area, equation 4.7, at each transducer.

$$I = \int \Delta p dt \tag{4.7}$$

Figure 4.20 and 4.21 show the simulated and experimental pressure and impulse at 4 m from the center of the blast. Figures 4.22 and 4.23 shows the same at 10 m. The experimental histories are solid lines and the simulated histories are dash-dotted.

The simulated initial shock wave with the following rarefaction wave is identical to the experimental results at both 4 m and 10 m. After about 10 ms at 4 m the secondary

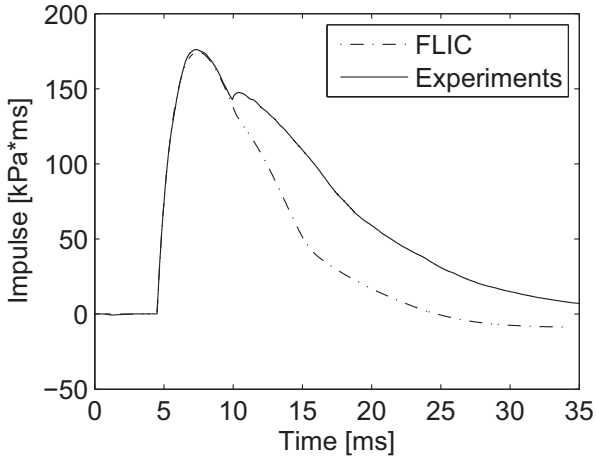

Figure 4.21: Impulse history at 4 m from center of charge comparison with experiments and simulations.

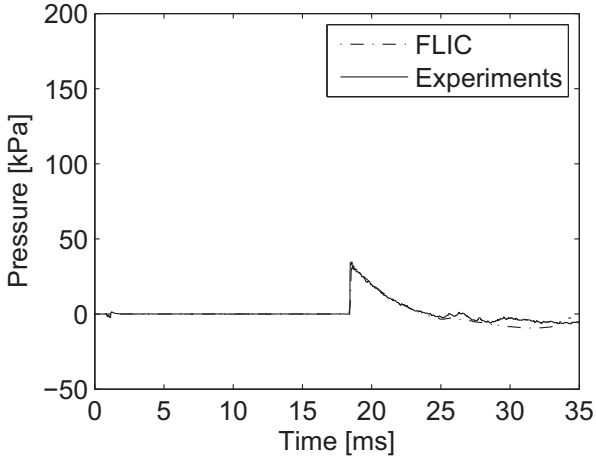

Figure 4.22: Pressure history at 10 m from center of charge comparison with experiments and simulations.

blast arrives but the magnitude of this shock is not predicted correctly by the simulations. The origin of this shock wave is the over-expansion of the gas due to the spherical shock propagation and a subsequent focusing in the center. The focusing takes place in the products from the high explosives and numerical diffusion discussed in chapter 4.1, figure 4.2, may be the reason for the under-prediction of the secondary shock. The internal energy and also the sound speed is over predicted in a low pressure and density region

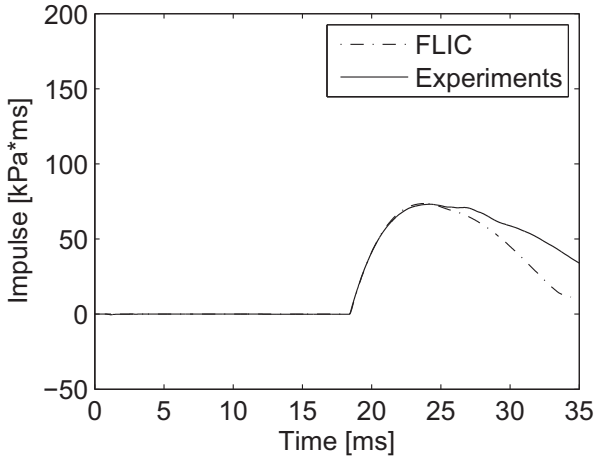

Figure 4.23: Impulse history at 10 m from center of charge comparison with experiments and simulations.

and entropy is artificially produced.

Conclusion

The simulated incident shock is similar to the experimental shock. This shows that the initial conditions for the high explosives is correct. The numerical scheme also behaves satisfyingly for this wave. The secondary shock is not handled correctly, which is a known problem and can only be corrected by higher accuracy methods or very fine mesh.

4.6.2 High Explosive Blast in Small-Scale Generic Single-Story System

This section presents simulations of high explosive blast in a generic building and the simulation results are compared with experimental data of [*Reichenbach and Neuwald, 1997*] in a small scale model of a one story building, see figure 4.24. The building is composed of six small rooms and one large room connected by a hallway. The height of the geometry is 39 mm. The small rooms have dimensions 130 mm by 117 mm by 39 mm, the large room has dimensions 130 mm by 280 mm by 39 mm and the hallway is 26 mm wide. The internal walls are 10 mm thick and the external wall is 20 mm thick. This is a 1:77 scale model. A high explosive charge is placed in the center of one room as showed in figure 4.24. The charge is 0.5 g of Nitropenta which corresponds to a 228 kg charge in full scale. In the experiments there are pressure transducers in every room except the room with the charge. In addition there are three transducers in the large room. In this thesis results from only two transducers are discussed, the one in the room opposite the room with the charge and one in the large room. The transducers are placed in the wall opposite the entrance to the rooms marked gage 1 and 9. Gage 1 experience the direct

blast from the detonation and in addition the reflected shocks, gage 1 should experience the highest pressures since it is located closest to the detonation in a direct path. Gage 9 is located far away from the initial blast and the waves that reach gage 9 has experienced several diffractions and reflections.

Simulation conditions

The numerical experiment is set up as a 3D domain with axisymmetry along the central horizontal plane of the geometry. The same solution strategy is used here as in chapter 4.6.1 where a small area around the charge is solved first on a fine mesh then mapped into the coarser mesh. The simulation mesh for the entire domain has a constant size of 1 mm.

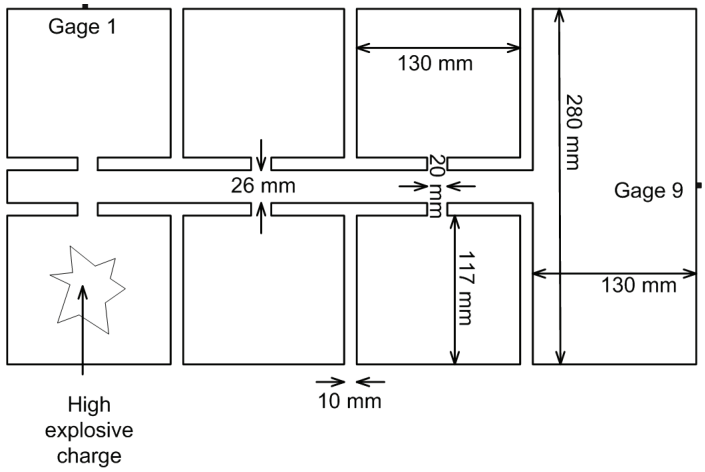

Figure 4.24: Experimental setup for high explosive blast in small scale house.

Results and discussion

To analyze the results from both the physical and numerical experiments a description of the shocks that reach the wall at gage 1 is given. Four different pressure peaks numbered in figure 4.25 are discussed. Since the transducer is set in the wall all pressure peaks are from stagnated waves. Peak number 1 is the shock wave from the initial blast which is an incident wave that has experienced diffraction when entering the hallway and room 1. Peak number 2 is a result of the reflected and focused shocks in the room with the charge. When the waves from the initial blast is reflected from all walls and focused in the center two separate peaks are produced since the rooms are non-quadratic the time of arrival of the reflected waves is different. Peak 3 is the reflection of peak 2 in the side walls and focusing in the far corners of room 2. The waves that produce 4 are the reflections of the strong shocks that has previously entered the room.

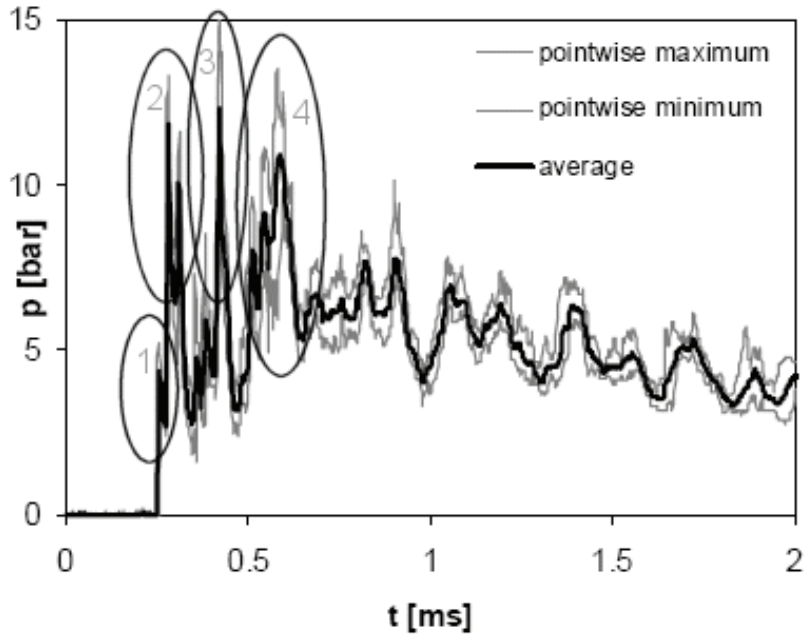

Figure 4.25: Pressure peak numbering from the experiments. [*Reichenbach and Neuwald, 1997*].

For sensor P1 simulated pressure results are plotted together with experimental pressure results in figure 4.26 and simulated and experimental impulses are seen in figure 4.27. For sensor P9 the pressure is shown in figure 4.28 and the impulse in figure 4.29.

The simulated pressure and impulse follow the experiments satisfyingly both at sensor P1 and P9. The maximum pressure and time of arrival are close to the experimental values and the pressure history follow each other quite well. The impulse also shows this. The simulation results show that peak 1 and the peaks in number 2 are merged at sensor P1. The numerical diffusion solves a shock over a few control volumes the scheme can not keep these three waves separate. With higher mesh resolution this may have been avoided but the computational cost of increasing the resolution in 3D simulation is very high since halving the mesh length makes the memory demand 8 times as high and computational time 16 times longer. This simulation does not have the same problem with the secondary shock as the free field test. The over-expansion of products is not as strong here since reflected waves from the ceiling and floor reaches the detonation center before the products have time to expand sufficiently.

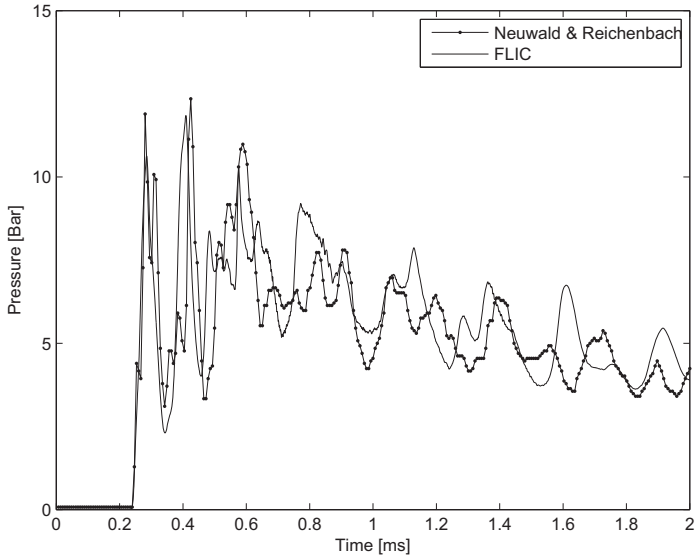

Figure 4.26: Experimental and simulated pressure history at P1.

Conclusion

The initial conditions set by the JWL equation of state gives good agreement between simulation and experiments for this case. The shock structure is reproduced but some pressure peaks are merged due to numerical diffusion. The problem of artificial production of entropy in low pressure and density areas is not seen in this simulation since the products don't have time to expand as in free field explosions.

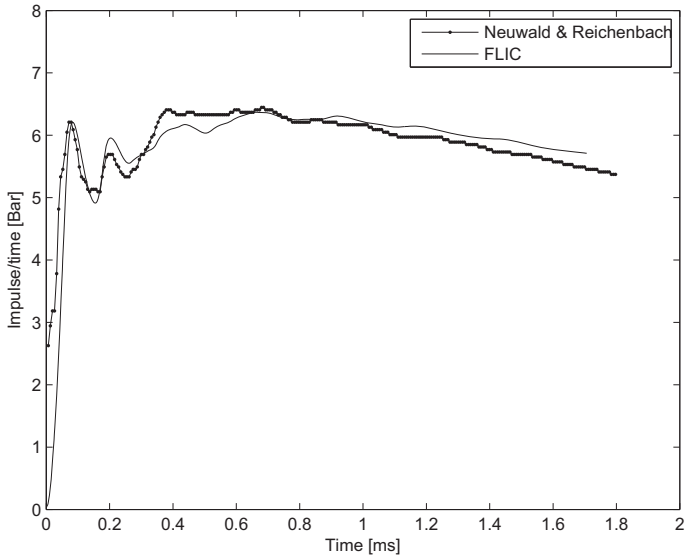

Figure 4.27: Experimental and simulated impulse history at P1.

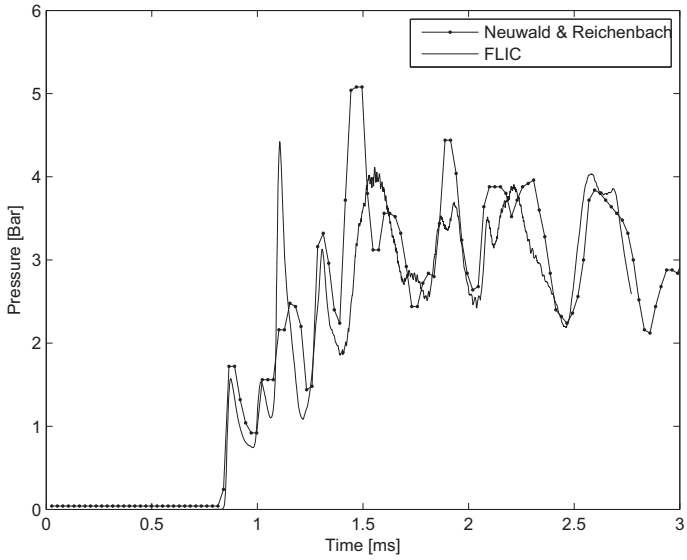

Figure 4.28: Experimental and simulated pressure history at P9

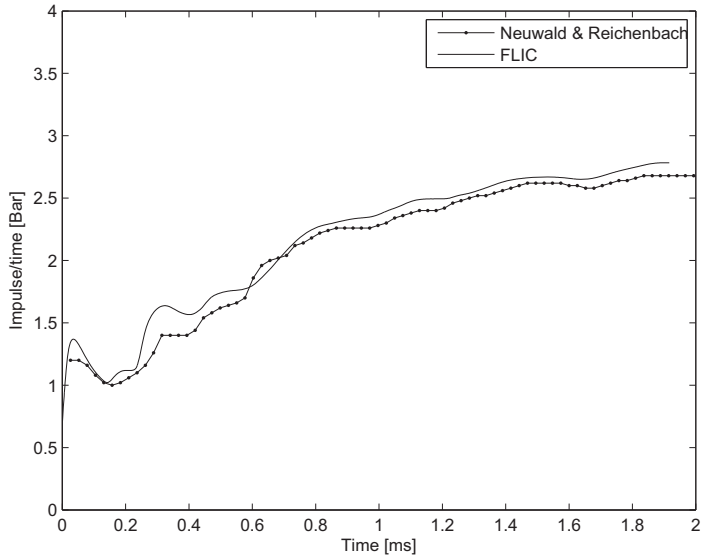

Figure 4.29: Experimental and simulated impulse history at P9

Chapter 5

Simulations of gas explosions

This chapter present simulations of gas explosions in complex geometries. Appendix A contain two papers which is not discussed here. The first paper was presented at MABS 20, Oslo 2008, and shows simulation- and experimental results of detonation and blast from fuel-air explosives (FAE). The second paper is published in International Journal of Hydrogen Energy [*Vaagsaether et. al., 2007*] and shows simulation- and experimental results of flame propagation in a pipe. The case is the same as in chapter 5.1 but the simulation method in the paper is different than the method presented in chapter 3.

5.1 Simulation of flame acceleration in a pipe with one obstacle

Parts of the work reported in this chapter was presented at ICDERS 21, Poitiers 2007, [*Vaagsaether and Bjerketvedt, 2007*]. This chapter presents simulation results of flame acceleration in a pipe with one obstacle. The simulations are compared with experimental results performed at Telemark University College by Knudsen et. al. [*Knudsen et. al., 2005a*], [*Knudsen et. al., 2005b*]. The experiments show the effect of the flame acceleration phase in a smooth tube before the flame passes an obstacle and the subsequent flame acceleration or DDT. The flame experiences several interactions with pressure waves that travels between the ignition end and the obstacle and the shape of the flame is strongly dependent on these interactions. The flame will experience the Richtmyer-Meshkov instability as a short duration force is acting on the flame. A more thorough explanation for a similar experiment in a square channel is presented in [*Gaathaug et. al., 2009*]. The geometry studied here is similar to the geometry studied by [*Dorofeev et. al., 1996*].

5.1.1 Geometry and setup

The experimental setup is shown in figure 5.1. It is a closed 4 m long tube with 0.107 m diameter. The tube is filled with stoichiometric hydrogen air at atmospheric pressure and 293 K. The ignition is a spark set in one end wall. A disc with 0.03 m hole (BR = 0.92) is placed 1.0 m from the ignition. A pressure transducer is placed at the ignition end and in addition there are five pressure transducers at 0.5 m intervals behind the

obstacle starting at 0.5 m. The simulation domain is discretized with 2D axisymmetric cylindrical coordinates and with two homogeneous meshes at 1 and 2 mm size. The assumption of 2D geometry is assumed because the strain in the axial-tangential plane and the radial-tangential plane is assumed small and the dominant strain rate is in the axial-radial plane due to the hemispherical development of the flame from central ignition and the cylindrical geometry.

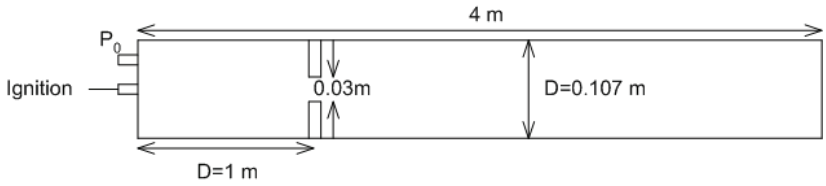

Figure 5.1: Experimental setup of a 4 m long tube with a single obstacle.

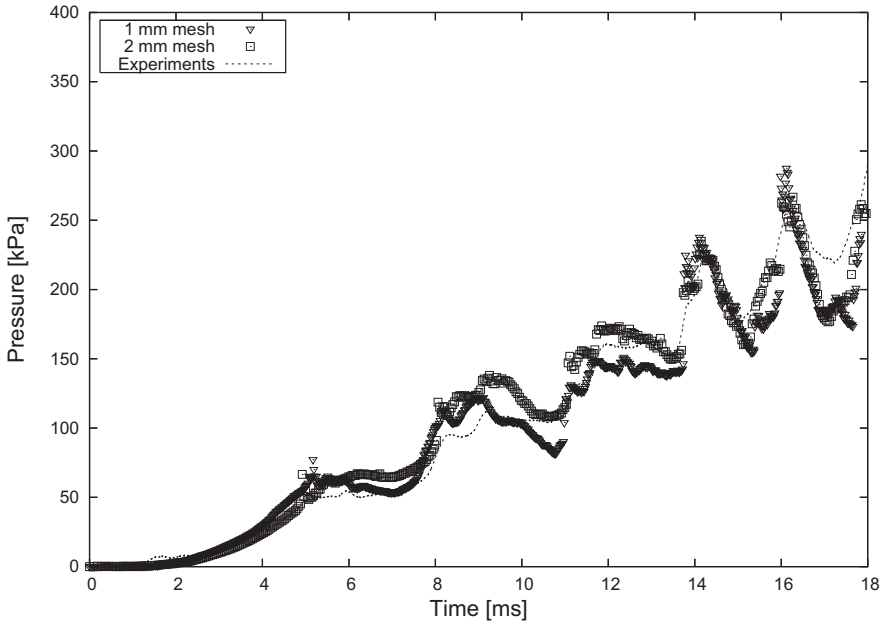

Figure 5.2: Pressure history at ignition point for simulations with 1 mm mesh and 2 mm mesh and for experiments. Stoichiometric hydrogen-air at 293 K and 1 atm in a tube with one obstacle.

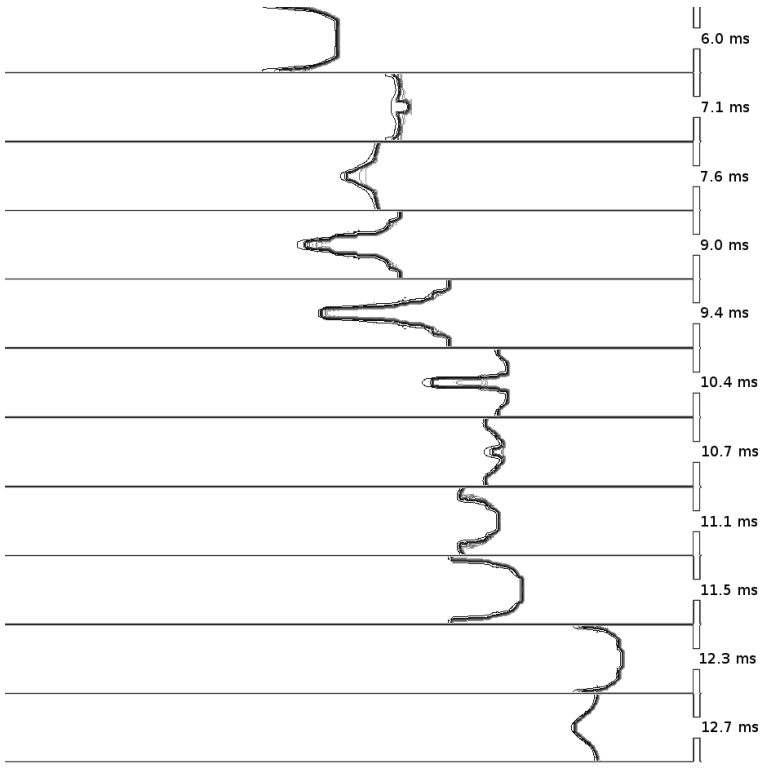

Figure 5.3: Simulated flame front development at time intervals from ignition in tube with one obstacle. Stoichiometric hydrogen-air.

5.1.2 Results and Discussion

Figure 5.2 shows the pressure records from transducer P_0 at the ignition end for the experiments and two simulations with two different mesh sizes, 1 mm and 2 mm. The simulation time in this figure is up to the time the flame passes the obstacle. Figure 5.3 shows the simulated flame front at different times from ignition time. The flame is highly distorted by pressure waves, as seen in figure 5.3. These large scale distortions are probably the most important effects that contribute to flame acceleration before the flame reaches the obstacle. By comparing simulated and experimental pressure histories it is possible to see that the simulated flame speed is reasonable. Propagating pressure waves are reflected from the flame front and these waves are captured by the transducer and the simulated time of arrival is the same as in the experiments. The combustion model keeps the flame thin and propagation is controlled by the reaction variable gradient model for the most part. The Arrhenius rate expression is only active in areas of high temperature and low values of β and only help to keep the flame thin in this part of the explosion. The flame inversion can be explained by the Richtmyer-Meshkov instability described in

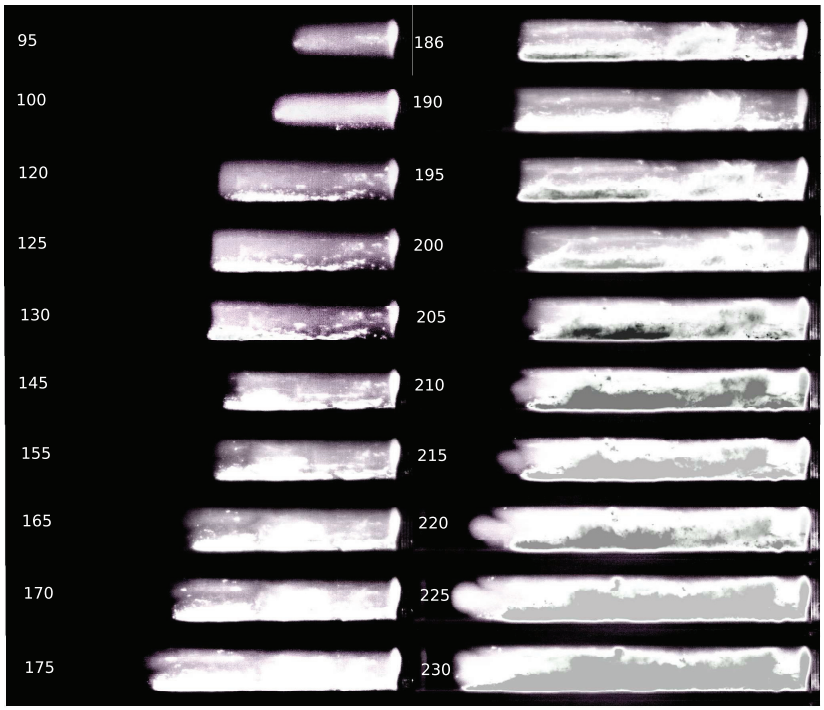

Figure 5.4: Experimental flame front development at time intervals from ignition in tube with one obstacle. Stoichiometric hydrogen-air at 293 K and 1 atm [*Gaathaug, 2008*].

chapter 2.1. When a pressure wave interact with the flame in the top image in figure 5.3 from the reactant side the flame is pushed in the direction of the products along the center axis of the pipe. When the same pressure wave is reflected at the back wall and interacts with an inverted flame, as seen in the third image, from the product side the RMI predicts a growth of the funnel. The pressure gradients and density gradients are opposite as the first interaction and the vorticity grows in the same direction. When the wave interacts with the inverted flame from the reactant side the signs of the cross product changes and the rotation changes direction and can be seen as the flame is again back to a finger shape in the 9th image.

[*Gaathaug, 2008*] filmed the flame development in a similar pipe as used in the simulation. Frames from the high speed film is shown in figure 5.4 where the shape of the flame starts as finger-shaped. When a pressure wave reflected from the obstacle interacts with the flame it gets a tulip shape (frame 120). When the wave again reaches the flame from the product side the tulip shape gets even more pronounced (frame 165). When again the wave reaches the flame from the reactant side at frame 190 the flame changes curvature and the leading front of the flame is in the central part of the pipe (frame 210). The process is shown schematically in figure 5.5 where the vorticity effecting the flame is indicated. The simulations does not show the details of the flame after it has interacted

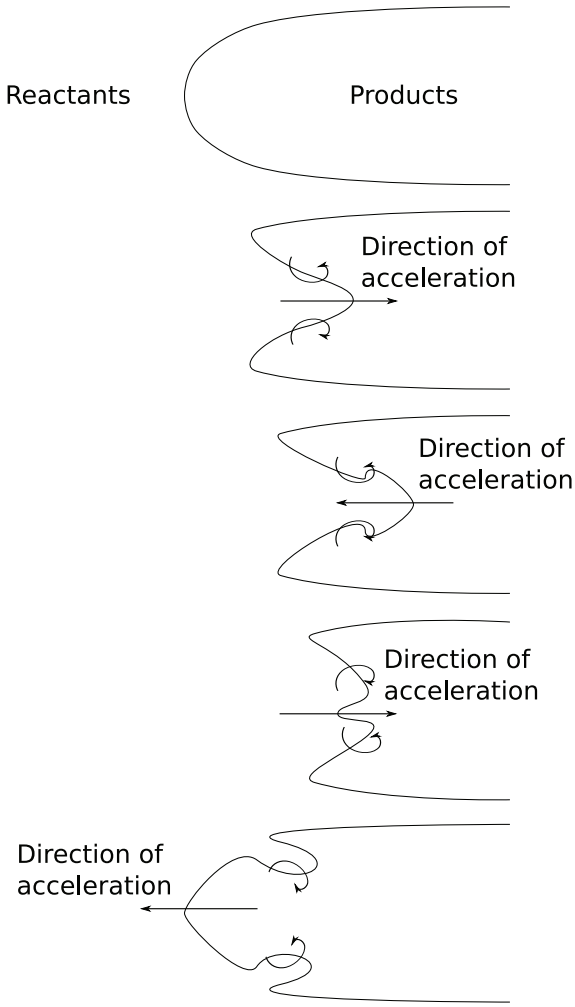

Figure 5.5: Drawing of the flame-pressure wave interaction with the direction of vorticity. First image: finger-shaped flame. Second image: a wave has interacted with the flame from the reactant side, changing the curvature. Third image: a wave has interacted with the flame from the product side increasing the vorticity. Fourth image: a wave has interacted with the flame from the reactant side changing direction of the vorticity and curvature. Fifth image: a wave has interacted with the flame from the product side increasing vorticity.

with a pressure wave and small tongues of reactants or products are reacted in an averaged larger volume due to the artificial thickness of the flame. This occurs even if the overall reaction rate is not over predicted but a finer mesh would be able to resolve the details in the simulated flame and should be able to show the details seen in the experiments.

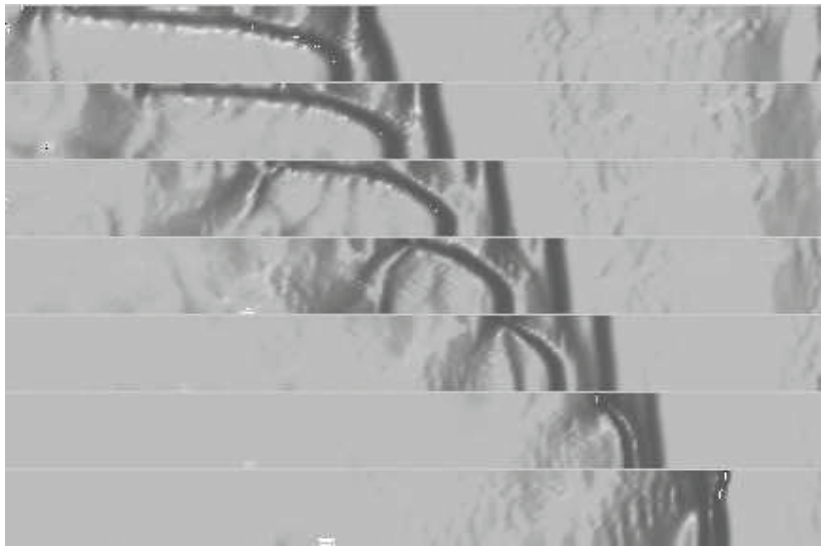

Figure 5.6: Simulated flame 220 mm to 740 mm behind obstacle with 1 mm mesh. The simulation shows high reaction rates at the walls. DDT occurs when the fast flame in the boundary layer catches up to flame tip. Stoichiometric hydrogen-air at 293 K and 1 atm.

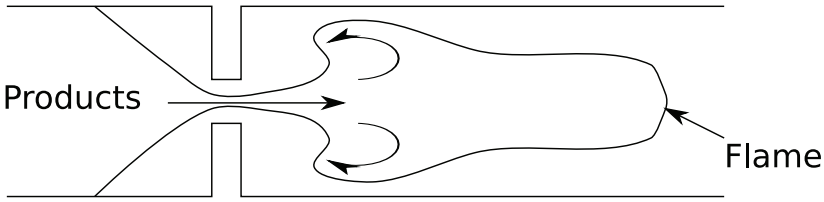

Figure 5.7: Schematics of the flame passing the obstacle. The vortex behind the obstacle increase the reaction rate.

Figure 5.6 shows the simulated density gradient contours behind the obstacle. The simulation is with 1 mm mesh size. The radial-axial plane shown is at a position from 220 mm to 740 mm behind the obstacle. The pressure in the section in front of the obstacle becomes high enough to choke the flow through the obstacle. When the flame passes the obstacle it follows the jet and forms a volume of unburned gas close to the wall. A vortex is formed behind the obstacle which create high reaction rates and a local explosion, see figure 5.7. The volume of reactants close to the wall burns with a very high reaction rate due to high velocities and turbulence. This high reaction rate create a shock wave that causes DDT when it catches up to the flame tip. The pressure sensor placed 0.5 m behind the obstacle, shown in figure 5.8, shows that it is not a detonation that goes through this volume but a deflagration. This volume is narrow and cannot sustain a detonation as the shock created from the high reaction rate is diffracted into the products.

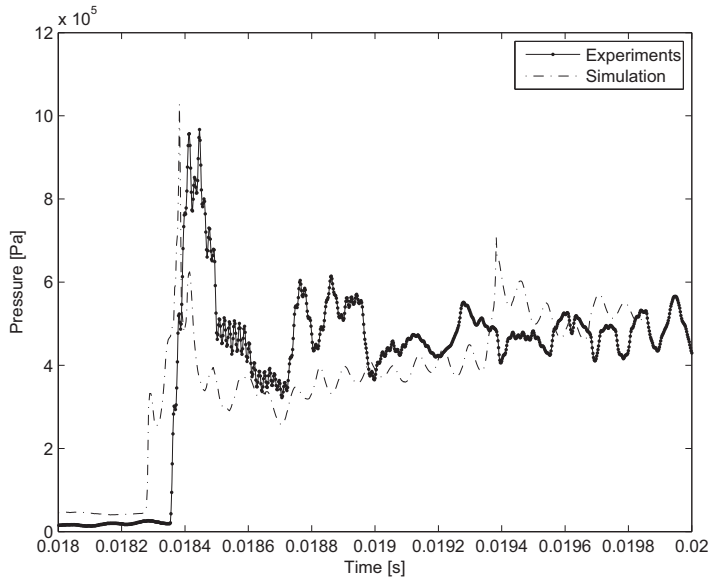

Figure 5.8: Experimental and simulated pressure records at 0.5 m behind obstacle. Stoichiometric hydrogen-air at 293 K and 1 atm.

The pressure sensor at 1 m behind the obstacle, figure 5.9, shows that there has been a transition to detonation and a detonation is propagating down the pipe. [*Kuznetsov et. al., 2005*] reported that high reaction rates close to the wall caused transition to detonation for a flame propagating in a smooth pipe and is similar to what is seen in these simulations.

5.1.3 Conclusion

The simulation results show that the combustion model behaves reasonable and simulations with this model show promising results for cases with deformations of the flame shape due to propagating pressure waves. The structure of the flame front is not captured in detail with the mesh sizes used in this simulation. The differences in pressure histories in front of the obstacle for the simulations with two different mesh sizes are small and for the 1 mm mesh the model predicts DDT behind the obstacle where the initiation is due to high reaction rates close to the wall. The position of the detonation is about the same as the experimental position.

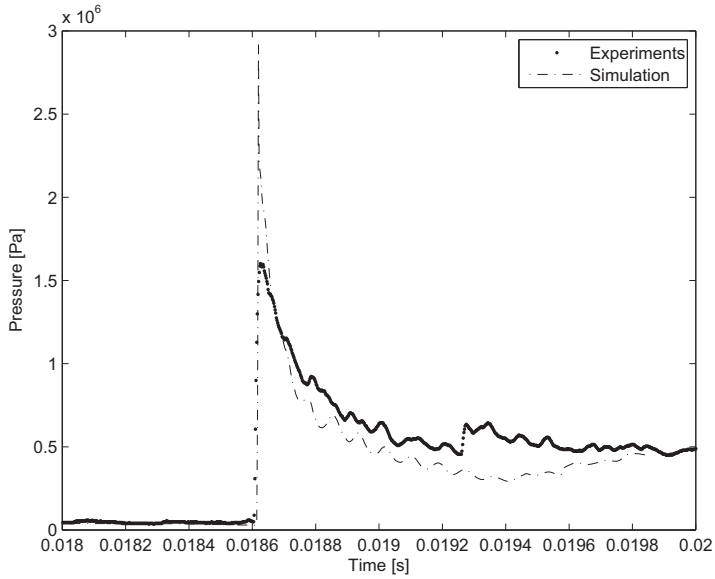

Figure 5.9: Experimental and simulated pressure records at 1.0 m behind obstacle. Stoichiometric hydrogen-air at 293 K and 1 atm.

5.2 Flame acceleration and DDT in channel with several obstructions

Parts of the work reported in this section was presented at ICDERS 22 [*Vaagsaether and Bjerketvedt, 2009*]. [*Lee et. al., 1985*] and [*Lee and Moen, 1980*] have described different regimes of high speed flame propagation in obstructed channels. Flame acceleration may lead to three different regimes, i) choked flow, ii) quasi-detonation where DDT occurs but the detonation fails due to interactions with obstructions and iii) CJ detonation. Experiments with flame acceleration and DDT in obstructed channels has been presented by several authors [*Lee et. al., 1985, Lee and Moen, 1980, Chan, 1995, Dorofeev, 2000, Teodorczyk et. al., 1988, Teodorczyk, 2007*] among others. [*Gamezo et. al., 2007*] has presented simulation results for channels with repeated obstacles with one step Arrhenius reaction rate. The flame acceleration in obstructed channels are caused by instabilities such as Rayleigh-Taylor, Richtmyer-Meshkov and Kelvin-Helmholtz, flame-shock interaction and flame-vortex interaction. Shock focusing and Mach-reflections cause transition to detonation. [*Thomas et. al., 2002*] presented experiments and a criterion for the onset of detonation from shock reflecting on an obstacle, equation 5.1.

$$\eta = \frac{h}{c_r \tau_r} \tag{5.1}$$

If η is smaller than one a direct initiation of detonation might not occur. Where h is the height of the obstacle, c_r is the sound speed behind the reflected shock and τ_r is the induction time behind the reflected shock. This number, called the Thomas number, explains that for smaller obstacles a stronger shock wave is needed to initiate a detonation.

The study of simulations of flame acceleration and DDT with an under-resolved mesh is motivated by having the ability to predict DDT and fast flames in large geometries or to get simulation results within a short time. Models for sub-grid behavior of the flame-flow field interaction are important for describing the flame acceleration since the flame front is thinner than the computational mesh size. This section describes some of the validation of this methods ability to predict DDT with an under-resolved mesh. The simulation results are compared with experiments by [*Teodorczyk, 2007*].

5.2.1 Geometry and setup

In figure 5.10 the experimental setup of [*Teodorczyk, 2007*] is shown and results from three different channel heights of 20 mm, 40 mm and 80 mm are presented here. The channel is 2 m long and closed in all directions and the blockage ratio for all experiments are 0.5. In the experiments the channel is 110 mm wide, but the simulation domain is in two dimensions assuming an infinitely wide channel with ignition along the entire width. The ignition of stoichiometric hydrogen-air mixture at atmospheric pressure and 293 K is in the center of one wall. Two different mesh sizes of 1.0 and 0.5 mm are tested but most of the results presented here are with 1 mm mesh.

5.2.2 Results and discussion

The results are presented as contour plots of gradients of density and flame speeds along the channel length just below the top wall. The present simulations are 2D simulations and according to [*Gamezo et. al., 2007*] there is not a significant difference between 2D and 3D simulations for this geometry. For all channel heights the flame accelerates due to the effects described in chapter 2.1 and a shock wave is formed ahead of the flame. When the shock passes an obstacle a diffracted shock front reflects at the bottom wall and creates a Mach-stem. Both the leading shock and Mach-stem reflects at the obstacles and is focused in the corner between the bottom wall and obstacle and can ignite the gas behind the focused shock to send a strong shock wave into the products that diffract over the obstacles and reflects at the top wall. The reflected and diffracted shock interacts with the flame from the product side and accelerates the flame and may even heat the reactants in front of the flame and cause DDT. The process is shown in figure 5.11 and is seen and discussed by several authors [*Lee et. al., 1985, Lee and Moen, 1980, Teodorczyk et. al., 1988, Shepherd and Lee, 1992*].

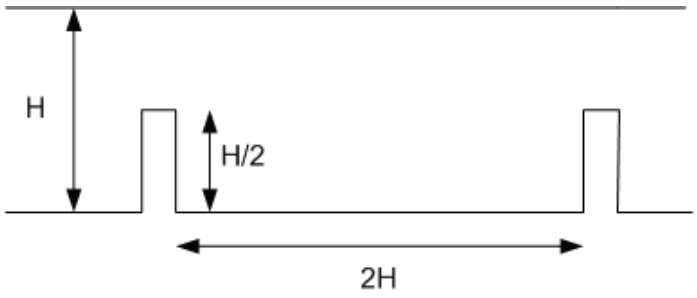

Figure 5.10: Experimental setup of [*Teodorczyk, 2007*] with channel height and distance between obstacles.

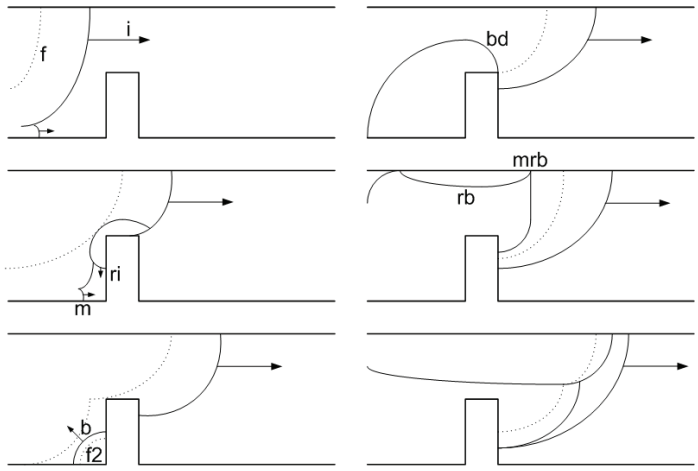

Figure 5.11: Explanation of the DDT process in the channel with repeated obstacles. Where f is the propagating flame, i is the incident shock created by flame acceleration, ri is the reflection of the incident shock at the obstacle, m is the Mach-stem from the reflection of the incident shock at the bottom wall, f2 is a flame created from ignition by the focusing of ri and m, b is the shock created by the constant volume reaction that caused f2, bd is a diffraction of b, rb is the reflection of bd from the top wall, mrb is the Mach-stem created by the same reflection. In the last image mrb catches up with the flame and causes DDT.

For simulations of the 20 mm channel the leading shock is reflected at the obstacles as seen from the sequence of images in figure 5.12 this reflected shock interacts with the flame and slows it down. The reflection of the shock at the bottom wall also creates a Mach-stem that together with the reflected leading shock is focused in the corner between the bottom wall and obstacle, this effect can be seen in experiments from [*Dorofeev, 2000*]. The flame speed of the 20 mm channel along the channel length as seen in figure 5.13 shows that the flame accelerates each time it passes an obstacle which is discussed by [*Gamezo et. al., 2007*] and is due to Rayleigh-Taylor, Richtmyer-Meshkov and Kelvin-Helmholtz instabilities and flame-vortex interactions behind obstacles. These effects are present in all cases discussed here. After about 0.4 m down the channel length from ignition the flame reaches an average speed of over 1000 m/s, fluctuating between 1200 m/s and 800 m/s and is described as the choking regime for this case. In the experimental results there are probably a transition to detonation around 0.7 m which is not seen in the simulation. But the flame speed after about 1.0 m is on average constant around 1000 m/s in both the experiments and in these simulations. The coarse mesh is not able to resolve the smaller scales of the different instabilities important in flame acceleration and these instabilities may form small hot spots that can cause DDT.

Figure 5.14 shows the DDT process in the 40 mm channel where the shock reflection of the top wall behind the flame is strong enough to ignite the reactants in front of the flame and cause a DDT. When the detonation in the 40 mm channel propagates past an obstacle the shock diffracts and the detonation fails, as can be seen in figure 5.15. For

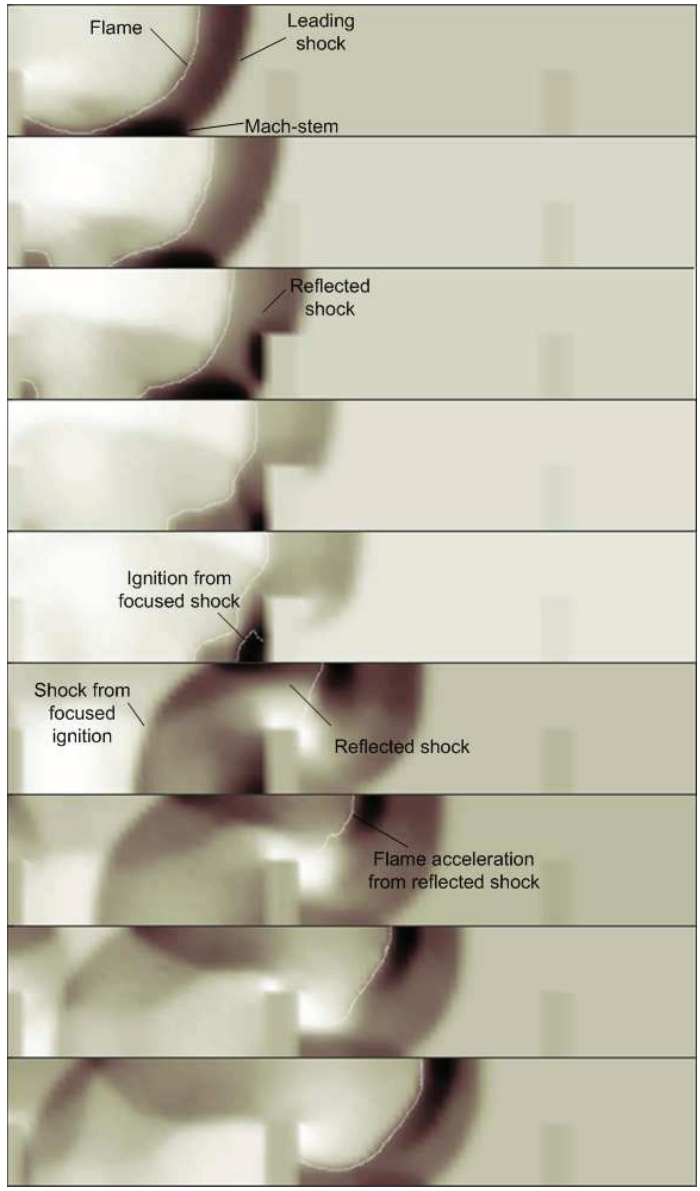

Figure 5.12: Simulated density gradients of shock-flame-obstacle interactions for the 20 mm channel with repeated obstacles with 1 mm mesh. Stoichiometric hydrogen-air at 293 K and 1 atm.

the 40 mm channel the flame accelerates due to the instabilities and vortex interactions explained above. In figure 5.16 when the flame has reached 1.1 m from ignition the flame experiences DDT and a flame speed of just below 2000 m/s is reached. Due to

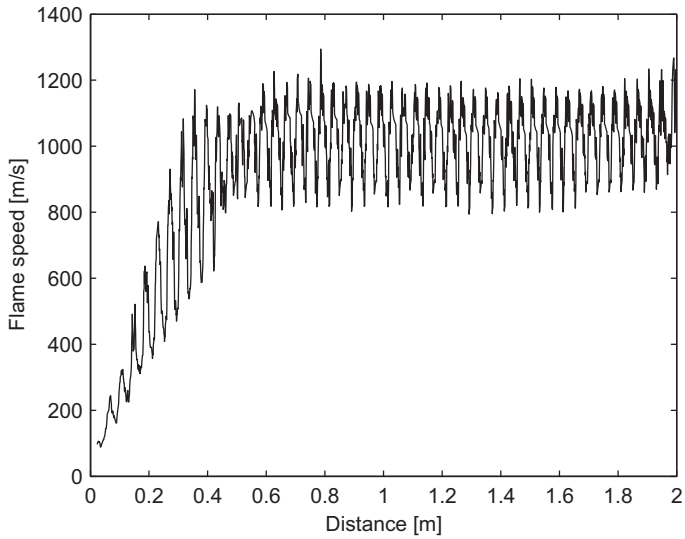

Figure 5.13: Simulated flame speed as a function of time for the 20 mm channel with repeated obstacles with 1 mm mesh. Stoichiometric hydrogen-air at 293 K and 1 atm.

diffraction over the next obstacle the flame does not propagate as a CJ-detonation. The average flame speed after this point is about 1400 m/s and can be interpreted as the quasi detonation regime. In the experiments there is a significant scatter of where the first DDT occurs. Figure 5.17 shows the flame speeds for the experiments in the 40 mm channel where DDT occurs between 0.9 and 1.0 m. The average flame speed in the experiments after this first transition is about 1250 m/s but varies with as much as 200 m/s.

In the channel with 80 mm height the flame experiences DDT almost at the end of the channel. Figure 5.18 shows that the shock formed from the ignition in the corner of the bottom wall diffracts over the obstacle and initiates a detonation when interacting with the flame. This detonation wave fails but is re-initiated when the shock reflects on the top wall. The flame speed for the 80 mm channel as seen in figure 5.19 show the same development as the other two cases but the position of the DDT is close to the end wall at about 1.6 m from ignition. Teodorczyk reports the position of DDT in this case to be about 1.6-1.7 m from ignition. The simulations show that the detonation in the 80 mm channel fails close to the end of the channel but was not seen in the experiments. The cause of the failure is the diffraction of the detonation front which is averaged over a few control volumes that are larger than the detonation thickness.

In figure 5.20 the results of a grid sensitivity test is shown. The 40 mm channel is probably the most interesting case since it includes flame acceleration, DDT and failure. The flame speed of the 40 mm channel along the channel is roughly the same for both mesh sizes.

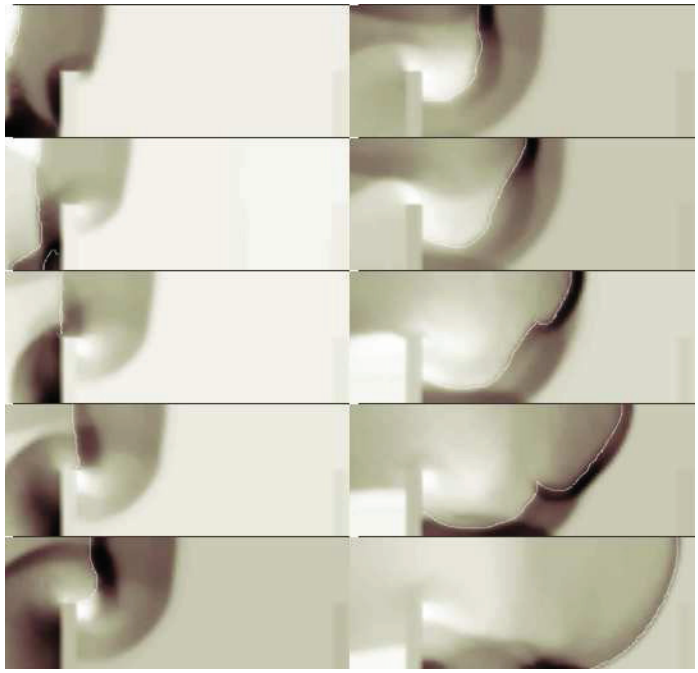

Figure 5.14: Simulated density gradients of shock-flame-obstacle interactions for the 40mm channel with repeated obstacles with 1 mm mesh. The images shows the DDT process. Stoichiometric hydrogen-air at 293 K and 1 atm.

5.2.3 Conclusion

A key element in these cases is that the leading shock becomes strong enough for all cases to ignite the gas in the shock focusing between the bottom wall and obstacle. The local explosion accelerates the flame and for the 40 mm and the 80 mm case cause transition to detonation. In the 40 mm case the detonation will not propagate as a stable CJ detonation but fails repeatedly. For the 40 mm channel the DDT occurs as this shock i reflected on the top wall but for the 80 mm channel the shock causes DDT as it diffracts over the obstacle but fails, it then re-initiates at the reflection at the top wall. The simulation of the experiments by [*Teodorczyk, 2007*] shows that the choking regime, quasi detonation regime and detonation are controlled by the interaction of a shock wave and the flame from the product side for this case. For the 20 mm channel the shock interacts with the flame and increase the flame speed and compress the reactants but is not strong enough to sufficiently heat the reactants to initiate a detonation. The simulated flame speeds for the 20 mm channel can be interpreted as the choking regime with average flame speed of 900-1000 m/s. For the 40 mm channel the shock is strong enough to cause transition but the detonation fails when it passes an obstacle. The process of DDT and failure to propagate is repeated until the end of the channel and is the mechanism of the quasi detonation regime with average flame speed of 1400 m/s. For the 80 mm channel the flame experiences DDT and propagate as a detonation. The simulation of these cases on an under-resolved

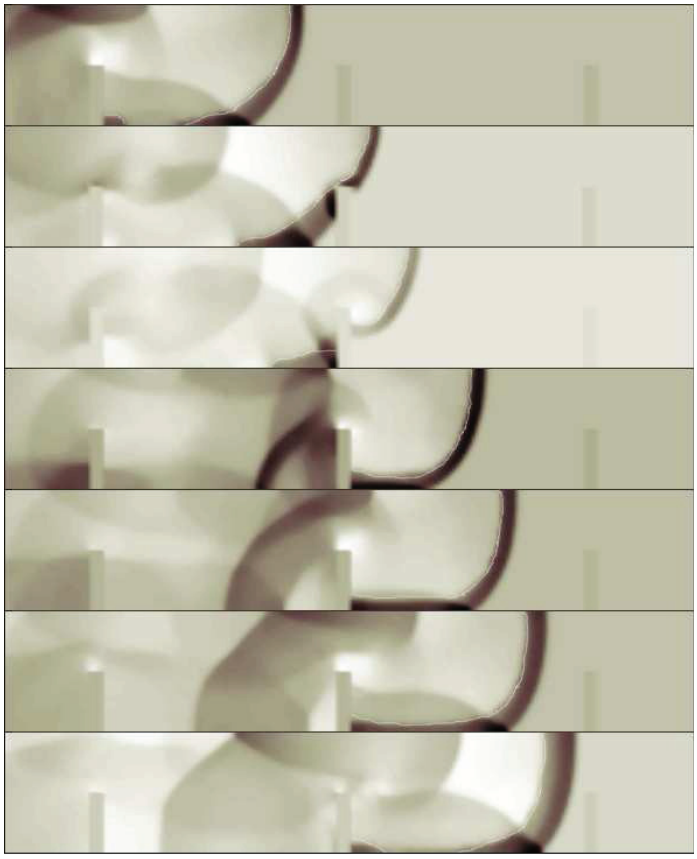

Figure 5.15: Simulated density gradients of shock-flame-obstacle interactions for the 40mm channel with repeated obstacles. The images shows the failure of detonation. Stoichiometric hydrogen-air at 293 K and 1 atm.

mesh show that it was possible to reproduce the different propagation regimes seen in the experiments of [*Lee et. al., 1985*,*Chan, 1995*,*Dorofeev, 2000*,*Teodorczyk, 2007*] and may suggest that the process of DDT in a channel with repeated obstacles are controlled by large scale effects like the ignition of reactants in the corners between the obstacles and bottom channel wall. The grid test did not show too large deviance between two different mesh sizes for the 40 mm case.

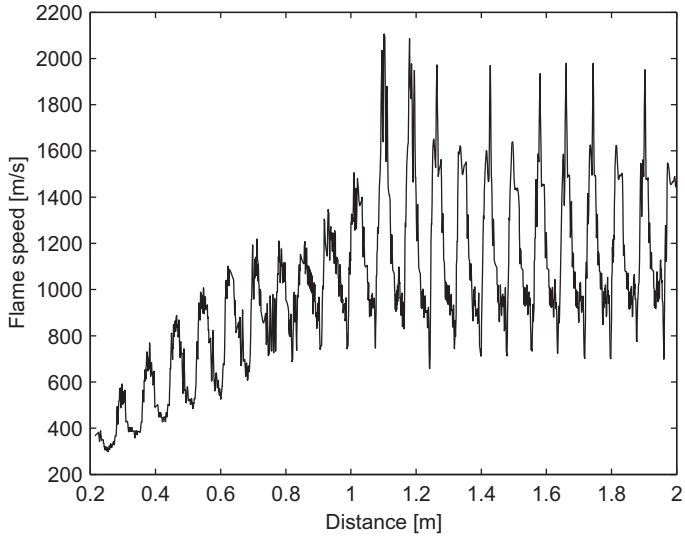

Figure 5.16: Simulated flame speed as a function of time for the 40 mm channel with repeated obstacles with 1 mm mesh. Stoichiometric hydrogen-air.

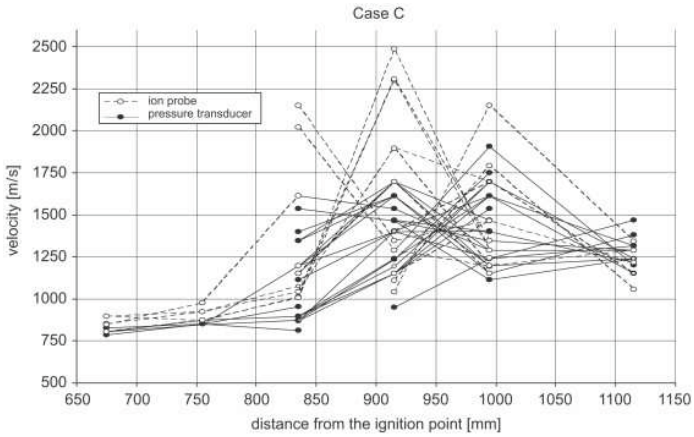

Figure 5.17: Experimental flame speeds for several experiments in the 40 mm channel with repeated obstacles. Stoichiometric hydrogen-air at 293 K and 1 atm. [*Teodorczyk, 2007*].

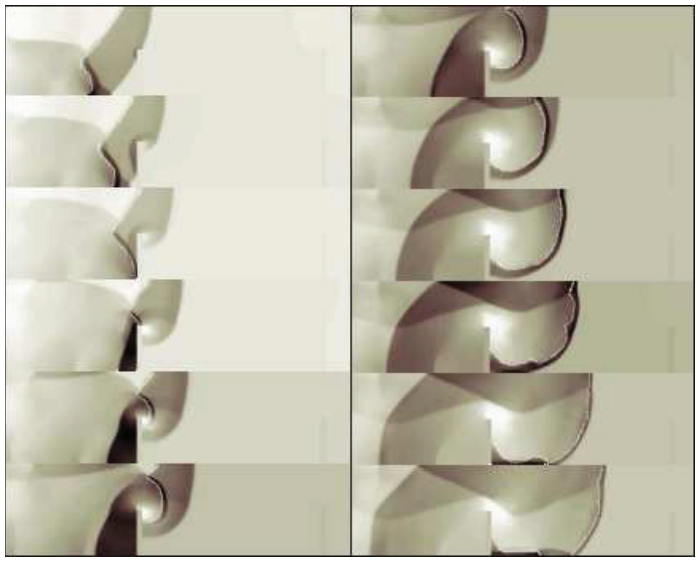

Figure 5.18: Simulated density gradients of shock-flame-obstacle interactions for the 80mm channel with repeated obstacles with 1 mm mesh. The images shows the DDT process. Stoichiometric hydrogen-air at 293 K and 1 atm.

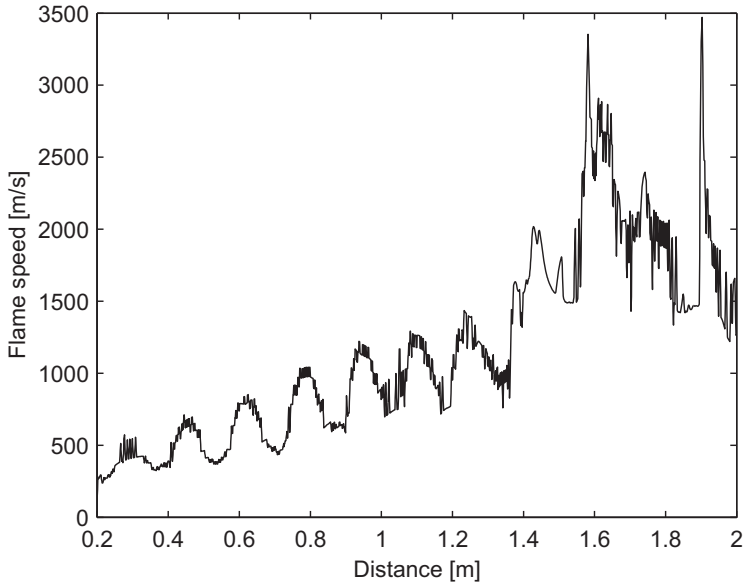

Figure 5.19: Simulated flame speed as a function of time for the 80 mm channel with repeated obstacles with 1 mm mesh. Stoichiometric hydrogen-air at 293 K and 1 atm with 1 mm mesh.

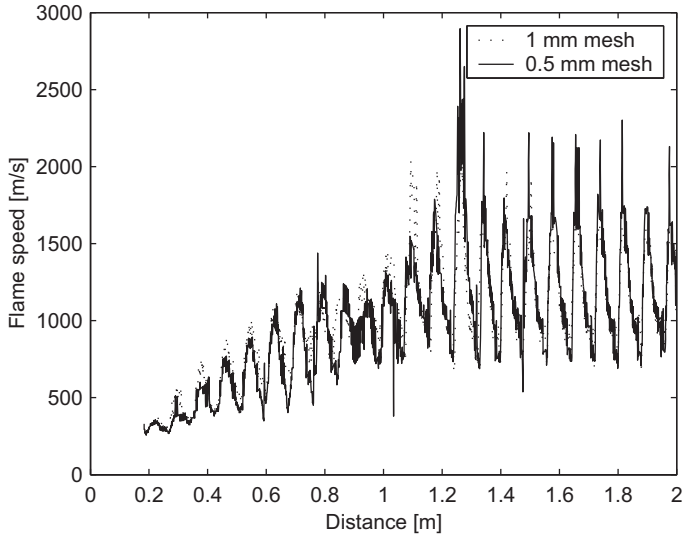

Figure 5.20: Grid sensitivity for the 40 mm channel with repeated obstacles for 1 mm mesh and 0.5 mm mesh. Stoichiometric hydrogen-air at 293 K and 1 atm.

5.3 3D simulation of channel with several obstructions

This section presents results of 3D simulation of hydrogen-air explosion in a channel with several obstructions. The case is the same as presented in section 5.2.1 with 40 mm channel height.

5.3.1 Geometry and setup

The simulation domain is 2 m long channel, 40 mm in height and 55 mm wide when assumed axis symmetry along the center of the channel. The simulation mesh is a Cartesian grid with constant length of 1 mm.

5.3.2 Results and discussion

Figure 5.21 shows the simulated flame speed along the channel. Figures 5.22, 5.23 and 5.24 show the experimental pressure histories at 795 mm, 875 mm and 955 mm from ignition and a simulated pressure three obstacle spacings farther down the channel. The experimental pressure records are extracted from the image files in the paper by [*Teodorczyk, 2007*] by a simple code and the accuracy of the extraction is not validated but it should reproduce the same curves as in the paper. The simulated time is set to match the strong pressure peak in figure 5.22 because this peak is thought to be due to initiation of the detonation.

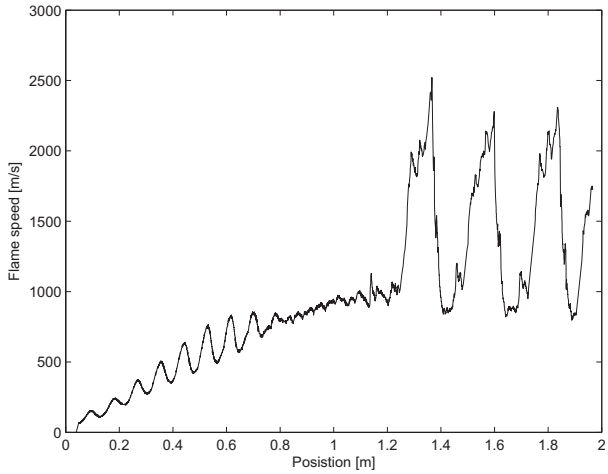

Figure 5.21: 3D simulation with 1 mm mesh of the flame speed along the center of the channel top wall for the 40 mm channel with repeated obstacles. Stoichiometric hydrogen-air at 293 K and 1 atm.

The pressure histories from the simulation is at a transducer-position three obstacle spacings farther from ignition. Since there is a significant scattering in the experiments

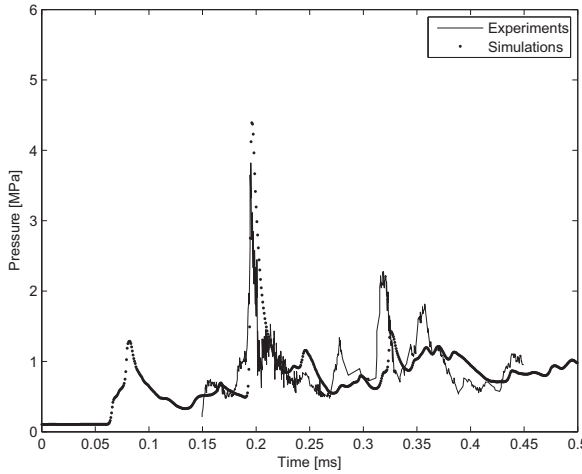

Figure 5.22: Experimental and simulated pressure history in the 40 mm channel with repeated obstacles and stoichiometric hydrogen-air at 293 K and 1 atm. The pressure transducer is 795 mm from ignition, the transducer in the simulation is placed three obstacle spacings farther from ignition.

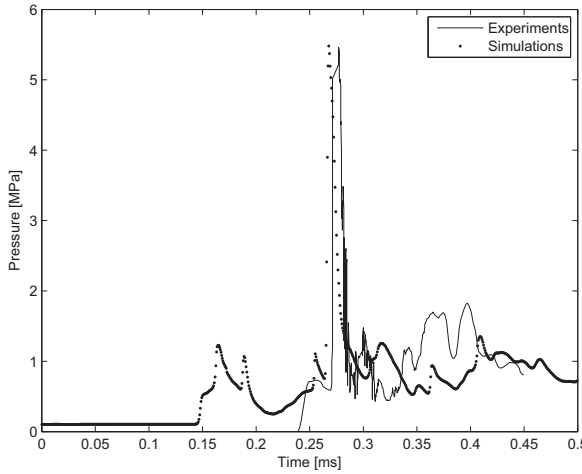

Figure 5.23: Experimental and simulated pressure history in the 40 mm channel with repeated obstacles and stoichiometric hydrogen-air at 293 K and 1 atm. The pressure transducer is 875 mm from ignition, the transducer in the simulation is placed three obstacle spacings farther from ignition.

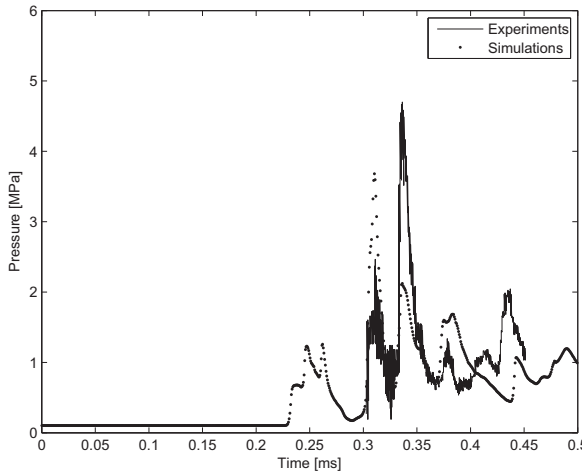

Figure 5.24: Experimental and simulated pressure history in the 40 mm channel with repeated obstacles and stoichiometric hydrogen-air at 293 K and 1 atm. The pressure transducer is 955 mm from ignition, the transducer in the simulation is placed three obstacle spacings farther from ignition.

the position of the first DDT is difficult to match with the experimental pressure data. The distance between first pressure rise and the shock from the initiation of the detonation is longer in the simulations than in the experiments. Since the simulated pressure is shifted three obstacle spacings the leading shock has propagated farther from the flame. The coarse resolution of the mesh does not capture all hot-spots and might smoothen small areas of high temperature to a lower temperature where the hot-spots may ”go off” and lead to detonation in the experiments. Compared with the 2D simulation the 3D simulation predicted the first DDT one obstacle later. This might be because of any strong shock produced from focusing may propagate in three directions compared with two for the 2D case and a simulated hot-spot in 2D may lead to transition while in 3D it weakens faster and may not cause transition. Another reason might be that in 2D the gas is ignited in the entire width of the channel and the flame propagates cylindrically and not spherically which might move the position where a sufficiently strong shock wave is formed. The 3D simulation does not show the same frequency of the pressure oscillations as the 2D simulation. The flame propagates with the detonation velocity for lengths of three obstacles compared with only one for the 2D simulation. The shock diffraction is not as critical for the the 3D simulation since the propagating detonation front is not plane. As the detonation passes the obstacle parts of the detonation fails and cause transverse waves that keep the detonation going as a CJ-detonation.

5.3.3 Conclusion

The 3D simulation showed similar behavior as the 2D simulation where DDT occurs and the flame propagates in the quasi-detonation regime. The simulated initiation and failure of detonation shows that this geometry with a point ignition behaves three dimensional and the details are handled differently for 2D and 3D. The coarse mesh might be the reason for the difference between simulations and experiments since the coarse mesh averages the flame over a few millimeters the details in formation of hot spots and diffraction of the front is not captured. The experiments show significant scattering in the position of the DDT and comparison between experiments and simulations is difficult.

5.4 Flame acceleration and DDT in methane-air mixtures

This section presents simulations of explosions in methane-air mixtures. The simulations are compared with experiments by [*Kuznetsov et. al., 2002*] where pre-mixed methane-air is filled in a pipe with repeated obstacles. In the experiments the flame position is recorded by photo-diodes to calculate the flame speed along the pipe. The model for the laminar burning velocity for stoichiometric methane-air is seen in equation 5.2 and was determined experimentally by [*Stone et. al., 1998*]. A one step and a two step reaction kinetic model are compared with the simulations shown in this section. The one step model is presented by [*Hanamura et. al., 1993*] and is seen in equation 5.3.

$$S_L = 0.366 \left(T/T_0\right)^{1.42} \left(p/p_0\right)^{-0.297} \tag{5.2}$$

$$\frac{d\beta}{dt} = -0.87 \cdot 10^8 \beta exp\left(-\frac{15636}{T(K)}\right) \tag{5.3}$$

The induction time for the two-step kinetics simulation was presented by [*Cheng and Oppenheim, 1984*] and is seen in equation 5.4. The second step in the two-step simulation is the same as the second step in the hydrogen-air simulations which is a simplification but it is assumed that the exothermal reactions of radicals are of similar rate and that the initial branching reactions are the limiting rates.

$$\tau = 1.19 \cdot 10^{-18} \left[CH_4\right]^{0.48} \left[O_2\right]^{-1.94} \cdot exp\left(\frac{23316}{T(K)}\right) \tag{5.4}$$

Comparison of the ZND-profile for the two reaction rate models is shown in figures 5.25 and 5.26. In figure 5.25 the reaction progress variable is plotted along the detonation front for both one- and two-step reaction kinetics. The induction zone thickness which is easily seen in the curve for the two-step rate is about 1.2 cm in length. For the one-step rate there is no typical induction zone with isothermal reactions but the highest reaction rate is at about 1.5 cm. These lengths correspond to ignition delay times reported by [*Spadaccini and Colket III, 1994*].

Figure 5.26 shows the temperature in the reaction zone for a ZND wave for one- and two-step kinetics. For the two-step kinetics the induction zone has a long region with low constant temperature. It is possible to resolve this region on a coarse simulation

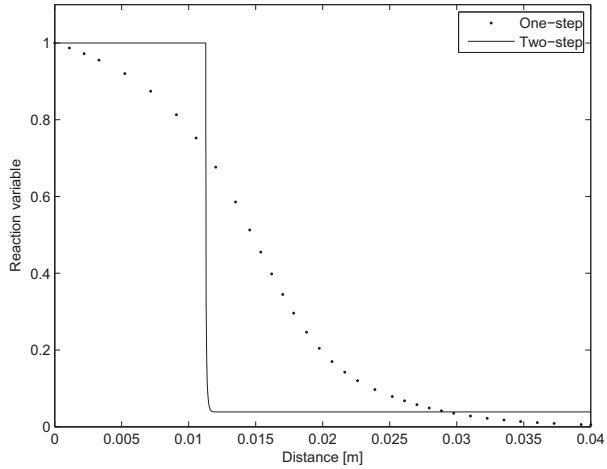

Figure 5.25: Profile of β along the detonation front for one- and two-step reaction kinetics for stoichiometric methane-air at 293 K and 1 atm.

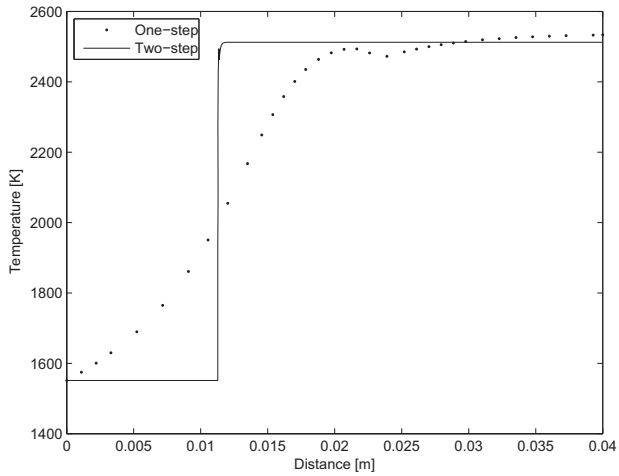

Figure 5.26: Temperature profile along the detonation front for one- and two-step reaction kinetics for stoichiometric methane-air at 293 K and 1 atm.

mesh while for the one-step method a coarse mesh will smoothen the details in the zone and more information is lost. Figure 5.27 shows the calculated induction time behind a shock wave as a function of the incident shock Mach number for the one- and two-step kinetics and the more detailed reaction set GRI mechanism 3.0. The GRI mechanism set is solved by Cantera [Cantera, n.d.] and the Shock and Detonation toolbox by [*Explosion*

Dynamics Laboratory, n.d.]. The induction time for the one-step model and the GRI-mech is the time from the gas is heated by the shock to the time of the highest reaction rate for a constant volume process. For the two-step model the induction time is the first step of the reaction in equation 5.4. When calculating failure of a detonation as it diffracts behind an obstacle the front thickness and local Mach number is important. A CJ-detonation in stoichiometric methane-air at normal conditions has a front shock Mach number of about 5. When a detonation diffracts the front shock is weakened and the local Mach number decreases. For the two-step kinetics and the GRI-mech the induction time is significantly increased as the Mach number decreases to 4. For the one-step kinetics this increase in induction time is not as dramatic and the failure or an initiation of a detonation will not be as sensitive to the front Mach number. For DDT simulations the gradient in induction time discussed in chapter 2.2 is formed differently for the one-step model and the other two methods. The different gradients may result in a constant volume explosion from shock reflections and focusing and no coherent energy release. As discussed earlier in the SWACER-mechanism the coherent energy release is critical for an initiation of a detonation.

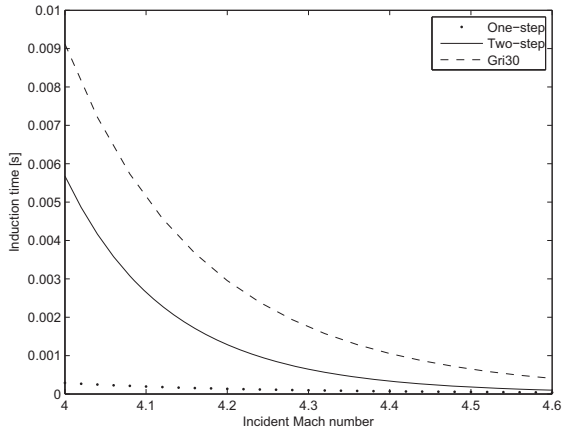

Figure 5.27: Calculated induction time for one- and two-step kinetics as a function of incident Mach number.

5.4.1 Geometry and setup

Figure 5.28 shows the repeated obstacle geometry. In this thesis the experiments in the 174 mm diameter pipe is simulated. This does not produce a CJ-detonation in the experiments since the pipe diameter is smaller than the smallest detonation cell size for methane-air at atmospheric pressure and 293 K which is about 300 mm.

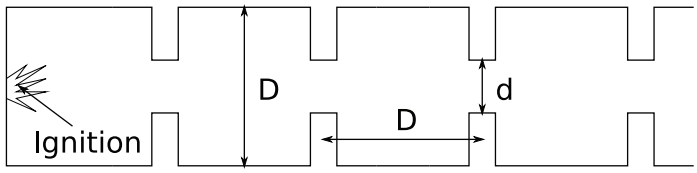

Figure 5.28: Geometry of the pipe with repeated obstacles. The pipe diameter is 174 mm and the obstacle diameter is given by the blockage ratio, $BR = 1 - \left(\frac{d}{D}\right)^2$. The blockage ratio in the tests shown here is 0.3 and 0.6.

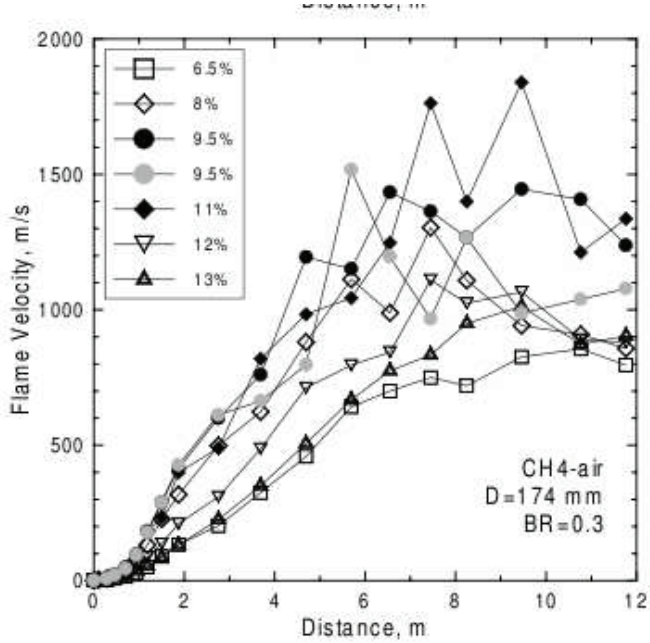

Figure 5.29: Flame speed for blockage ratio 0.3 for different methane concentrations, [*Kuznetsov et. al., 2002*].

5.4.2 Results and discussion

Figures 5.29 and 5.30 are the experimental results from [*Kuznetsov et. al., 2002*] for flame speed along the pipe for BR = 0.3 and 0.6. The experiments show that in the pipe with BR = 0.3 the flame reach speeds around 1400 m/s while in the pipe with BR = 0.6 the flame speeds reach only 700 m/s. This suggests that the flame in the BR = 0.3 pipe propagates as a quasi detonation where it experiences DDT but fails to propagate as a detonation while for the BR = 0.6 the flame propagates as a fast deflagration. Figure 5.31 shows the simulated flame speed along the center of the pipe for the two-step kinetics model. The results show clearly two different propagation regimes like in the experiments. The simulated flame speed for BR = 0.3 oscillates for each time the flame passes an

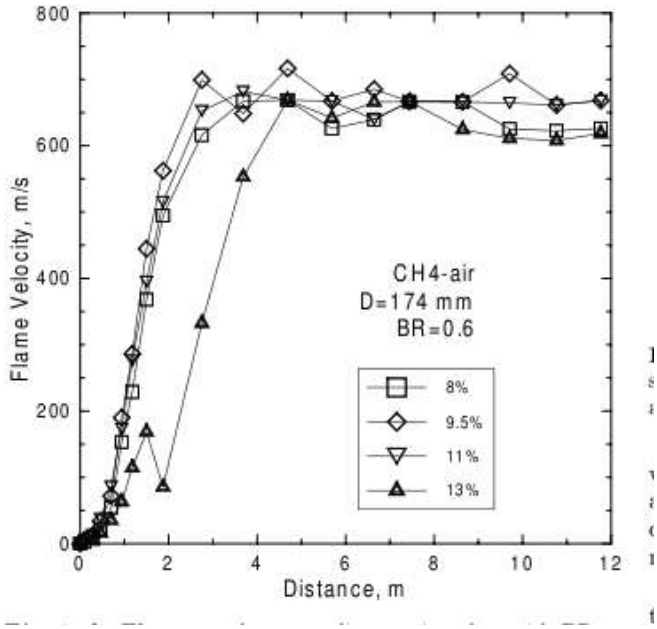

Figure 5.30: Flame speed for blockage ratio 0.6 for different methane concentrations, [*Kuznetsov et. al., 2002*].

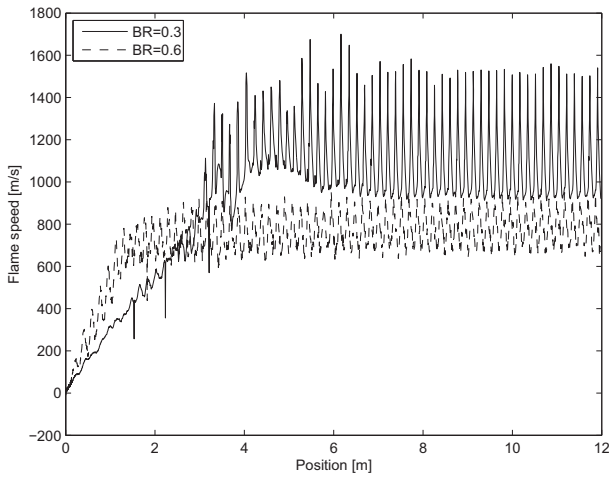

Figure 5.31: Simulated flame speed of the 174 mm pipe for blockage ratio 0.3 and 0.6. Stoichiometric methane-air and two-step kinetics model.

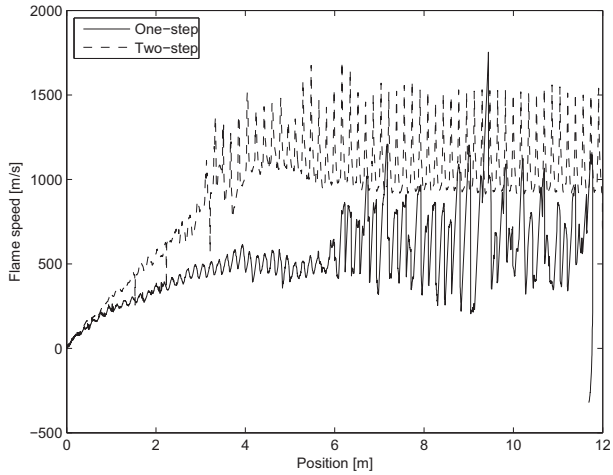

Figure 5.32: Simulated flame speed of the 174 mm pipe for blockage ratio 0.3 for both one- and two-step kinetics and stoichiometric methane-air.

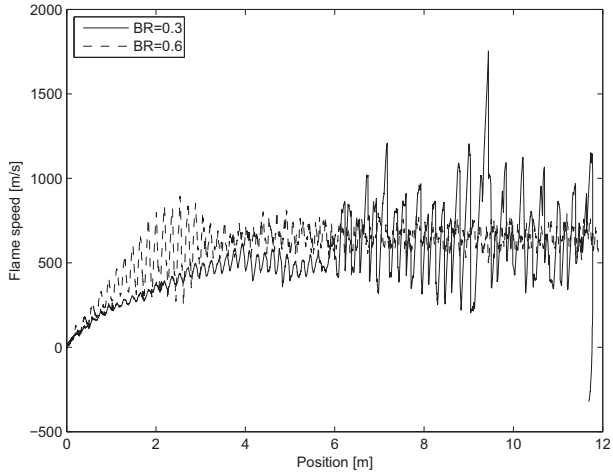

Figure 5.33: Simulated flame speed of the 174 mm pipe for blockage ratios 0.3 and 0.6 for one-step kinetics and stoichiometric methane-air.

obstacle. These spikes in the flame speed indicate strong local explosions that are possible DDTs which fail to propagate as detonations. The mechanisms of DDT in channels with repeated obstacles are discussed earlier in this thesis. Figure 5.32 shows the simulated flame speeds along the channel with BR = 0.3 for one- and two-step kinetics. The one-step kinetic simulation is unable to produce the same level of flame speed as the two-

step model even though the induction time is not as dependent on temperature as shown above. An explanation is that the one-step kinetic simulation does not produce gradients in induction time and the reflected and focused shock waves produce hot spots that only lead to constant volume explosions. Simulations with the one-step kinetics produce the same quasi-steady flame speed for both blockage ratios as seen in figure 5.33. The flame speed in the choking regime is controlled by the pressure gradient across an obstacle. When the pressure drop is large enough the flow becomes choked and the flame reach the speed of sound of the products.

5.4.3 Conclusion

The flame speeds for the two blockage ratios show clearly different propagation regimes which are seen in simulations with two-step kinetics. The method is able to capture the different regimes of flame acceleration and DDT in methane-air in obstructed channels but the choice of reduced chemical kinetic models are critical for a reasonable simulation. The one-step chemical kinetic rate used here is incapable of reproducing the same effects as the two-step model but it might be one-step models that can behave more like a detailed reaction model. For better accuracy it is suggested that more detailed reaction models are used.

Chapter 6

Conclusion

6.1 Conclusion

This thesis presents the work on creating a simulation method for modelling gas explosions and blast. The method was created for pre-mixed homogeneous mixtures and solves the Favre-averaged conservation equations of mass, momentum, energy and species with the FLIC-scheme and fractional step method. An one-equation turbulence model account for small scale effects. The method can be applied with a coarse computational mesh for simulations of real sized cases but small scale effects from instabilities and gas dynamics might not be seen in the simulations.

Some important points that can be concluded:

- A reaction rate model for simulating deflagrations and detonations is presented. The model combines a turbulent burning velocity model and an Arrhenius rate. This combination makes it possible for the method to handle deflagrations and detonations.
- Simulations of deflagrations and detonations with the reaction model shows that this method can simulate explosions in gas mixtures from a weak ignition to fast deflagration and transition to detonation. The flame acceleration is dominated by instabilities such as turbulence, Kelvin-Helmholz, Rayleigh-Taylor, Richtmyer-Meshkov and Landau-Darrieus. Flame-vortex interactions and shock-reflections and focusing becomes more important as the total flame speed increases and pressure waves are formed. These effects are shown by simulations with the presented method. A summary of the presented simulations are shown in table 6.1.
- Fast deflagration, quasi-detonation and CJ-detonations are flame propagation regimes in channels with repeated obstacles. The mechanism of these regimes are shown by simulations and is similar to the mechanisms seen in experiments by other researchers. The chemical kinetic term in the reaction rate model becomes dominant in these explosions and the choice of simplified model can strongly influence the results.
- The method simulates the details in a detonation front. The Arrhenius rates makes it possible to use very fine mesh that can resolve a detonation front and simulate

the details in the front. For a structured detonation front the detonation cells become regular and the triple point collisions occur at a constant single frequency. Unstructured detonation fronts show an irregular triple point pattern and pockets of unreacted gas is formed and can be seen far behind the shock front.

- The JWL equation of state is implemented in the code for simulations of high explosive products. Simulated blast from high explosives produce similar pressures and impulses as experiments. The secondary shocks, specially from free field experiments, are not reproduced in detail by the method. Numerical diffusion artificially produce entropy in the low pressure region in the over expanded products and the effect of the secondary shock is lost.

- A turbulence model is implemented in the code to handle small scale effects of turbulence on the flame front. Turbulence increase flame surface area and increase transport of heat and mass in the flame brush. The effect of the turbulence model is not thoroughly investigated in this thesis.

- The effect of the ideal gas law for simulating gas explosions is discussed. The presented method uses a heat capacity ratio for the reactants and one for the products. For some gas mixtures where there are high temperatures in the reactants or low temperature in the products the ideal gas law might be a coarse assumption.

Table 6.1: Summary of simulations and comments on the results.

Description of experiment	Reference	Comments on simulation results
Various standard tests of numerical schemes for hyperbolic equations with analytical conditions.	[*Toro, 1999*] and [*Liska and Wendroff, 2003*]	The simulation results show that the numerical scheme simulates the three wave families but numerical diffusion smooths discontinuities and regions of low pressure and density where the scheme produces entropy.
1D detonation simulation with one and two step reaction rate.	[*Erpenbeck, 1969*], [*Bourlioux and Majda, 1992*]	The coarse mesh of 2 control volumes pr. reaction length is not able to produce an oscillating detonation. The medium resolution of 5 volumes shows the oscillating peak pressure but the peaks are under predicted. Introducing an induction zone increases the total reaction zone length and the effective resolution increases producing similar peak values for 5 and 10 control volumes pr. exothermal reaction length.
2D detonation simulation with one step global reaction rate.	[*Gamezo et. al., 1999*], [*Bourlioux and Majda, 1992*]	The detonation simulation with relative activation energy of 0.8 shows a regular cellular front and the RMI and KHI is seen clearly. In the simulation with relative activation energy of 7.4 the detonation front becomes unstructured where the triple point collisions produced pockets of unreacted gas. The simulation results are in accordance with results shown by other researchers.

Turbulent shear layer with convective Mach-number 0.51	[*Samimy and Elliot, 1990*]	The simulations with mesh size 0.25 and 0.5 mm show results similar to the experimental results for the mean velocity and spreading rate. The simulation with 1 mm mesh diffused the shear layer and produced too large spreading rate. For this statistically steady shear layer the turbulence model produced satisfactory results.
Full scale high explosive free field test with 2 L C4	[*Langberg et. al., 2004*]	The simulation is able to reproduce the incident shock wave from the high explosive detonation. The secondary shock which is an effect of the over expansion of the products is under-predicted. The effect of numerical diffusion in areas with low pressure and low density is shown earlier and the artificial diffusion produce entropy in this region.
Small scale high explosive inside building with 0.5 g of PETN.	[*Reichenbach and Neuwald, 1997*]	As the 2D free field case but the secondary shock is not formed in the same way because of the small room in which the high explosive is placed. The simulation results show similar pressure values and durations as the experiments.

Gas explosion in tube with one obstacle, hydrogen-air in 4 m long 107 mm ID tube.	[*Knudsen et. al., 2005a*, *Knudsen et. al., 2005b*]	The simulations show that a gas explosion in a closed or partly closed pipe produce pressure waves that propagates back and forth in the pipe interacting with the flame. The RMI causes large distortions of the flame shape and flame area. A transition to detonation is simulated behind the obstacle close to the wall and is seen in both experiments and in other literature. The two mesh sizes produced almost the same pressures in the section ahead of the obstacle which is similar to the experimental data.
Gas explosion in channel with repeated obstacles, hydrogen air in a 2.0 m long 20, 40 and 80 mm high channel with obstacles of BR = 0.5.	[*Teodorczyk, 2007*]	Three different flame propagation regimes are seen in both experiments and simulations. The flame in the 20 mm channel propagates in the choking regime, in the 40 mm channel the flame propagates as quasi-detonation and in the 80 mm channel the flame reaches CJ detonation for a short distance. The mechanisms of DDT is shown by the simulations and are similar as the mechanisms shown with experiments by other researchers. The 3D simulation of the 40 mm channel show that the details in the explosion is three dimensional.

Gas explosion in pipe with repeated obstacles, methane-air in 12 m long 174 mm ID tube with BR = 0.3 and 0.6.	[*Kuznetsov et. al., 2002*]	Simulations of methane-air explosions in a pipe with repeated obstacle shows two different propagation regimes as the experiments. The higher BR produce flame speeds of the order of the product sound speed and can be classified as chocking regime. The lower BR produce higher flame speeds but not CJ detonation.

6.2 Further work

Some suggestions for improving the performance of the presented method:

- Adaptive mesh refining for increasing the local mesh resolution in the flame front. A finer mesh increases accuracy and may even remove the need for a turbulence model while refining the whole computational domain is not needed and is computationally expensive.
- More complex turbulence modelling to handle transition to turbulence and rapidly changing strain rates. If the method is going to be used for averaged equations the modelled turbulence need to be simulated with high accuracy. This is specially difficult in highly transient cases as gas explosions where a stagnant gas is suddenly accelerated by a pressure wave. Both compressible effects and transient effects makes this difficult and need to be addressed in further work.
- More detailed chemical kinetics to simulate the reaction rate in the many thermodynamic states that occur in gas explosions. Simplified kinetics usually has a validity region for pressure and temperature.
- Real gas equations of state for calculating internal energy. The ideal gas law does not take into account temperature dependency of the heat capacities which might be important for the accuracy in calculating shock waves and detonations.
- Include more detailed transport mechanisms to account for different Lewis numbers.

Bibliography

[*Austin, 2003]* J. M. Austin, *The role of instability in gaseous detonation*, PhD. Thesis, 2003, California Institute of Technology, Pasadena, California.

[*Austin et. al., 2005]* J. M. Austin, F. Pintgen, J. E. Shepherd, *Reaction Zones in Highly Unstable Detonations*, Proceedings of the Combustion Institute 30, 2005, 2:1849-1857

[*Van den Berg, 1985]* A.C. Van den Berg, *The Multi-Energy Method, a framework for vapour cloud explosion blast prediction, Journal of Hazardous Materials*, Volume 12, 1985, 1-10.

[*Bourlioux and Majda, 1992]* A. Bourlioux, A. Majda, *Theoretical and numerical structures for unstable two-dimensional detonations*, Combustion and Flame 90, 1992, 211–229.

[Buncefield report Vol. 1, 2008] *The Buncefield incident 11 December 2005*, The final report of the Major Incident Investigation Board, Vol. 1, 2008.

[*Campbell and Woodhead, 1927]* C. Campbell, D. W. Woodhead, *The Ignition of Gases by an Explosion Wave. Part I. Carbon Monoxide and Hydrogen Mixtures*, Journal of the Chemical Society, 1927, pp 1572-1578

[Cantera, n.d.] *Cantera project home page*, Google code, http://code.google.com/p/cantera/

[*Chan and Greig, 1988]* C. K. Chan, D. R. Greig, *The structure of fast deflagrations and quasi-detonations* Proceedings of the Combustion Institute 22, 1988, 1733–1739.

[*Chan, 1995]* C. K. Chan, *Collision of a shock wave with obstacles in a combustible mixture*, Combustion and Flame 100 ,1995, 341–348.

[*Chao and Lee, 2003]* J. Chao, J. H. S. Lee, *The propagation mechanism of high speed turbulent deflagrations*, Shock waves 12, 2003, 277-289

[*Chapman, 1899]* D. L. Chapman, *On the rate of shock waves for an arbitrary equation of state*, Philosophical Magazine (1899) 47:90-104

[*Cheng and Oppenheim, 1984]* R. K. Cheng, A. K. Oppenheim, *Autoignition in methane-hydrogen mixtures*, Combustion and Flame 58, 1984, 125–139.

[*Chomiak, 2000]* J. Chomiak, *Turbulent reacting flows*, 3rd edition, 2000, Graduate course book, Chalmers University of Technology.

[*Chou, 1945]* P. Y. Chou, *On the velocity correlations and the solution of the equations of turbulent fluctuation*, Quart. Appl. Math. 3, 1945, 38.

[*Ciccarelli and Dorofeev, 2008]* G. Ciccarelli, S. Dorofeev, *Flame acceleration and transition to detonation in ducts* Progress in Energy and Combustion Science Volume 34, Issue 4 499-550 (2008).

[*CSB Don Holmstrom, 2010]* D. Holmstrom, *Statemant of CSB investigations supervisor Don Holmstrom updating the public on the CSB's investigation of the catastrophic accident at Kleen Energy, Middletown, Connecticut*, CSB February 25, 2010, http://www.csb.gov/assets/news/document/CSB_statement_2_25_2010.pdf (06.02.10)

[*Darrieus, 1938]* G. Darrieus, *Propagation d'un front de flamme*, La Technique Moderne (Paris) 1938 and Le Congres de Mecanique Appliquee (Paris) 1945.

[*Densiov and Troshkin, 1959]* Yu. N. Denisov, Ya. K. Troshin, *Pulsating and Spinning Detonation of Gaseous Mixtures in Tubes*, Dokl. Akad. Nauk SSSR (Phys.-Chem. Sec) 1959 125 No.1, 110-113.

[*Dorofeev et. al., 1996]* S. B. Dorofeev, A. S. Kochurko, V. P. Sidorov, A. V. Bezmelnitsin, W. M. Breitung, *Experimental and numerical studies of the pressure field generated by DDT events*, Shock Waves Volume 5, 1996, 375–379.

[*Dorofeev, 2000]* S. B. Dorofeev, V. P. Sidorov, M. S. Kuznetsov, I. D. Matsukov, V. I. Alekseev, *Effect of scale on the onset of detonations, Shock Waves* ,10 (2000) 137–149.

[*Dorofeev et. al., 2001]* S. B. Dorofeev, M. S. Kuznetsov, V. I. Alekseev, A. A. Efinmenko, W. Breitung, *Evaluation of limits for effective flame acceleration in hydrogen mixtures, Journal of Loss Prevention in the Process Industries* , 14 (2001) 583–589.

[*Döring, 1943]* W. Döring, *Uber den detonations vorgang in gasen*, Ann. phys. (1943) 43 6:421-436

[*Erpenbeck, 1969]* J. J. Erpenbeck, *Theory of detonation stability*, Internation Symposium on Combustion, 12(1), 1969, 711-721.

[*Explosion Dynamics Laboratory, n.d.] Explosion Dynamics Laboratory web-site*, CalTech, http://www.galcit.caltech.edu/EDL/index.html, Pasadena, California.

[*Fickett and Wood, 1966]* W. Fickett, W. W. Wood, *Flow calculations for pulsating one-dimansional calculations*, Phys. Fluids 9, 1966, 903

[*Fickett and Davies, 1979]* W. Fickett, W. C. Davies, *Detonation theory and experiment*, University of California Press, 1979.

[*FLACS web cite, n.d.]* CMR, FLACS overview, http://www.gexcon.com, http://www.gexcon.com/index.cfm?id=268677 (04.16.10)

[*Flohr and Pitsch, 2000]* P. Flohr, H. Pitsch, *Centre for Turbulent Research Proceedings of the Summer Program* , (2000).

[*Gamezo et. al., 1999]* V. N. Gamezo, D. Desbordes, E. S. Oran, *Two-dimensional reactive flow dynamics in cellular detonation waves*, Shock Waves Volume 9, 1999, 11–17.

[*Gamezo et. al., 2007]* V. N. Gamezo, T. Ogawa, E. S. Oran, *Numerical simulations of flame propagation and DDT in obstructed channels filled with hydrogen-air mixures, Proceedings of the Combustion Institute* 31 (2007) 2463–2471.

[*Gamezo et. al., 2008]* V. N. Gamezo, T. Ogawa, E. S. Oran, *Flame acceleration and DDT in channels with obstacles: Effect of obstacle spacing* Combustion and Flame 155, 2008, 302–315.

[*Gaathaug, 2008]* A. V. Gaathaug, *Flame propagation in a atransparent pipe with a single obstruction.* Master thesis, 2008, Telemark University College.

[*Gaathaug et. al., 2009]* A. V. Gaathaug, D. Bjerketvedt, K. Vaagsaether, *Experiments with flame propagation in a channel with one obstacle and premixed H_2-air*, 22nd ICDERS, 2009, Minsk, Belarus.

[*Hanamura et. al., 1993]* K. Hanamura, R. Echigo, S. A. Zhdanok, *Superadiabatic combustion in a porous medium*, Int. J. Heat and Mass Transfer 36(13), 1993, 3201–3209.

[*Hawley and Zabusky, 1989]* J. F. Hawley, N. J. Zabusky, *Vortex paradigm for Shock-accelerated density-stratified interfaces*, Physical Review Letters, 63 (12), 1989, 1241–1244.

[*He, 2000]* L. He, *A scaling analysis of the critical conditions for a deflagration-to-detonation transition*, Comb. Theory and Modelling 4, 2000, 107–122.

[*von Helmholtz, 1868]* H. L. F. von Helmholtz, *"On the discontinuous movements of fluids*, Monthly Reports of the Royal Prussian Academy of Philosophy in Berlin Volume 23, 1868, 215.

[*Helzel, 2000]* C. Helzel, *Numerical approximation of conservation laws with stiff source term for the modelling of detonation waves*, PhD Thesis, Otto-von-Guericke-Universität Magdeburg, 2000.

[*Iijima and Takeno, 1984]* T. Iijima, T. Takeno, *Effects of temperature and pressure on burning velocity*, Proc. Faculty of Engineering, Tokai Univ. Vol. X, 1984, 53–67.

[*Jouguet, 1917]* E. Jouguet, *Mechanique des exlosifs* Octave Doin Paris (1917)

[*Lord Kelvin, 1871]* Lord Kelvin, *Hydrokinetic solutions and observations*, Philosophical Magazine Volume 42, 1871, 362–377.

[*Khoklov and Oran, 1999]* A. M. Khoklov, E. S. Oran, Numerical simulation of detonation initiation in a flame brush: the role of hot spots, Combustion and Flame (1999) 119:400-416.

[*Knudsen et. al., 2005a]* V. Knudsen, K. Vaagsaether, D. Bjerketvedt, *An experimental study of hydrogen-air gas explosions in a single obstructed pipe*, Proc. of the First Baltic Combustion Meeting, 2005.

[*Knudsen et. al., 2005b]* V. Knudsen, K. Vaagsaether, D. Bjerketvedt, *Experiments with hydrogen-air explosions in a closed pipe with a single obstacle*, Proc. of the European Combustion Meeting, 2005.

[*Korobeinikov et. al., 1972]* V. P. Korobeinikov, V. A. Levin, V. V. Markov, G. G. Chernyi, *Propagation of blast in a combustible gas*, Astronautica Acta 17, 1972, 529–537.

[*Kuznetsov et. al., 2000]* M. S. Kuznetsov, V. I. Alekseev, S. B. Dorofeev, *Comparison of critical conditions for DDT in regular and irregular cellular detonation systems, Shock Waves* 10 (2000) 217–223.

[*Kuznetsov et. al., 2002]* M. Kuznetsov, G. Ciccarelli, S. Dorofeev, V. Alekseev, Yu. Yankin, T. H. Kim, *DDT in methane-air mixtures*, Shock Waves, 12, 2002, 215–220.

[*Kuznetsov et. al., 2005]* M. Kuznetsov, V. Alekseev, I. Matsukov, S. Dorofeev, *DDT in a smooth tube filled with hydrogen-oxygen mixture*, Shock waves 14(3), 2005:205-215

[*Landau, 1944]* L. Landau, *On the theory of slow combustion*, Acta Physicochimica U.S.S.R. 19(1), 1944, 77–85.

[*Langberg et. al., 2004]* H. Langberg, S. O. Christensen, S. Skudal, *Test program with small concrete "kasun" houses*, Norwegian Defence Estates Agency, FoU report 24/2004.

[*Lee et. al., 1968]* E.L. Lee, H. C. Hornig, J. W. Kury, *Adiabatic expansion of high explosive detonation products* Lawrence Radiation Laboratory report UCRL-50422 (1968).

[*Lee and Moen, 1980]* J. H. S. Lee and I. O. Moen, *The mechanism of transition from deflagration to detonation in vapor cloud explosions.* Prog Energy Combustion Sci, 6 (1980) 359–389.

[*Lee et. al., 1985]* J. H. Lee, R. Knystautas, C. K. Chan, *Turbulent flame propagation in obstacle filled tubes, Proc. Combust. Inst.* 20 (1985) pp. 1663-1672

[*Lee, 2008]* J. H. S. Lee, *The Detonation Phenomenon*, Cambridge University Press New York (2008).

[*LeVeque, 2002]* R. J. LeVeque, *Finite volume methods for hyperbolic problems*, Cambridge University Press, 2002.

[*Liñàn and Williams, 1993]* A. Liñàn, F. A. Williams, *Fundamental aspects of combustion*, Oxford University Press, 1993.

[*Liska and Wendroff, 2003]* R. Liska, B. Wendroff, *Comparrison of several difference schemes on 1D and 2D test problems for the Euler equations.*, SIAM J. Sci. Comput. 2003 Vol. 25, No.3, pp. 995-1075.

[*Markstein, 1957]* G. H. Markstein, *A shock-tube study of flame front-pressure wave interaction, 6th International Symposium of Combustion* pp. 387-398, Reinhold, London (1957).

[*The MathWorks, n. d.] Mathworks home page*, The MathWorks, http://www.mathworks.com/

[*Meshkov, 1969]* E. E. Meshkov, *Instability of the interface of two gases accelerated by a shock wave*, Soviet Fluid Dynamics, Volume 4, 1969, 101–104.

[*von Neumann, 1942]* J. von Neumann, *Theory of detonation waves*, Office of Research and Development (1942) Report No. 549

[Noh, 1987] W. F. Noh, *Errors for calculations of strong shocks using an artificial viscosity and artificial heat flux*, J. Comput. Phys. 72, 1987, 78–120.

[*Oran and Gamezo, 2007*] E. S. Oran, V. N. Gamezo, *Origins of the deflagration-to-detonation transition in gas-phase combustion* Combustion and Flame Volume 148, Issue 1-2 (2007) 4-47.

[*Pande and Tonheim, 2001]* J. O. Pande, J. Tonheim, *Ammonia plant NII: Explosions hydrogen in a pipeline for CO2*, Process Safety Progress 20(1), 2001, 37–40.

[*Poisont and Veynante, 2001]* T. Poisont, D. Veynante, *Theoretical and numerical combustion*, Edwards, 2001, Philadelphia, USA.

[*Pintgen, 2004]* F. Pintgen, *Detonation diffraction in mixtures with various degrees of instability*, PhD. Thesis, 2004, California Institute of Technology, Pasadena, California.

[*Prandtl, 1925]* L. Prandtl, *Bericht uber Untersuchungen zur ausgebildeten Turbulenz*, ZAMM 5, 1925, 136.

[*Lord Rayleigh, 1882]* Lord Rayleigh, *Investigation of the character of the equilibrium of an incompressible heavy fluid of variable density* Proceedings of the London mathematical society Vol. 14, (1882) 170–177.

[*Reichenbach and Neuwald, 1997]* H. Reichenbach, P. Neuwald, *Small Scale Detonations in a Generic Single-Story System*, The 15th International Symposium on Military Aspects of Blast and Shock (MABS15), 1997, Banff, Alberta, Canada

[*Richtmyer, 1954]* R. D. Richtmyer, *Taylor instability in shock acceleration of compressible fluids*, Los Alamos Scientific Laboratory report 1914, 1954.

[*Samimy and Elliot, 1990]* M. Samimy, G. S. Elliot, *Effects of compressibility on the characteristisa of free shear layers*, AIAA J. 28, 1990, 439–445.

[*Samtaney and Zabusky, 1994]* R. Samtaney, N. J. Zabusky, *Circulation deposition on shockaccelerated planar and curved density-stratified interfaces: Models and scaling laws*, Journal of fluid Mechanics, Volume 269, 1994, 45–78.

[*Schultz and Shepherd, 2000]* K. Schultz, J. Shepherd, *Validation of Detailed Reaction Mechanisms for Detonation Simulation* Explosion Dynamics Laboratory Report FM99-5, 2000.

[*Shepherd and Lee, 1992]* J. E. Shepherd and J. H. S. Lee, *On the transition from deflagration to detonation In: M. Y. Hussaini, A. Kumar and R. G. Voigt, Editors, Major research topics in Combustion*

[*Shepherd, 2008]* J. E. Shepherd, *Detonation in gases*, Proceedings of the Combustion Institute, 32(1), (2008), 83-98.

[*Strehlow, 1991]* R. Strehlow, *Chapter 6 in Fossil fuel combustion, a source book*, W. Bartok and A.F. Sarofim. Wiley Interscience. 1991, John Wiley and Sons, Inc.

[*Sichel et. al., 2002]* M. Sichel, N. A.Tonello, E. S.Oran, D. A.Jones, *Proc. R. Soc. Lond. A*, 458, (2002), 49–82.

[*SOAR, 2000]* Flame Acceleration and Deflagration to Detonation Transition In Nuclear Safety, State-of-the-Art Report by a Group of Experts. OECD Nuclear Energy Agency. NEA/CSNI/R(2000)7. August 2000.

[*Spadaccini and Colket III, 1994]* L. J. Spadaccini, M. B. Colket III, *Ignition delay characteristics of methane fuels*, Prog. Energy Combust. Sci. 20, 1994, 431–460.

[*Stone et. al., 1998]* R. Stone, A. Clarke, P. Beckwidth, *Correlations for the laminar-burning velocity of methane/diluent/air mixtures obtained in free-fall experiments*, Combustion and Flame 114(3-4), 1998, 546–555.

[*Taki and Fujiwara, 1978]* S. Taki, T. Fujiwara, *Numerical analysis of two-dimensional non-steady detonations*, AIAA, (1978), 16(1):73–77.

[*Taylor, 1950]* G. I. Taylor, *The instability of liquid surfaces when accelerated in a adirection perpendicular to their planes.* Proceedings of the royal society London. Series A, Mathematical and Physical Science, 201(1065), (1950), 192–196.

[*Teerling et. al., 2005]* O. J. Teerling, A. C. McIntosh, J. Brindley, V. H. Y. Tam, *Premixed flame response to oscillatory pressure waves*, Proc. Comb. Inst. 30, 2005, 1733–1740.

[*Teodorczyk et. al., 1988]* A. Teodorczyk, J. H. S. Lee, R. Knystautas, *Propagation Mechanism of Quasi-Detonations*, Proceedings of the Combustion Institute 22, 1988, 1723–1731.

[*Teodorczyk, 2007]* A. Teodorczyk, *Scale effects on hydrogen-air fast deflagrations and detonations in small obstructed channels, Journal of Loss Prevention in the Process Industries* doi:10.1016/j.jlp.2007.06.017 (2007).

[*Thomas and Bambrey, 2002]* G. O. Thomas, R. Bambrey, *Observations of the emergence of detonation from a turbulent flame brush*, Proc. Combust. Inst. Volume 29, Issue 2, (2002), 2809-2815.

[*Thomas et. al., 2002]* G. O. Thomas, S. M. Ward, R. L. I. Williams, R. J. Bambrey, *On critical conditions for detonation initiation by shock reflection from obstacles*, Shock Waves 12(2), (2002), 111–119.

[*Thomas et. al., 2001]* G. O. Thomas, R. Bambrey, C. Brown, *Experimental observations of flame acceleration and transition to detonation following shock-flame interaction, Combustion theory and modelling* Volume 5, Issue 4 (2001) 573-594.

[*Toro, 1999]* E. F.Toro, *Riemann solvers and Numerical methods for fluid dynamics.* Springer-Verlag Berlin Heidelberg, (ISBN 3-540-65966-8), (1999).

[*Townsend, 1976]* A. A. Townsend, *The structure of turbulent shear flow*, 2nd ed., 1976, Cambridge University Press, New York, USA.

[Urtiew and Oppenheim, 1966] P. A. Urtiew, A. K. Oppenheim, *Experimental observations of the transition to detonation in an explosive gas*, Proc. Royal Society of London, A8 vol. 295, 1966, 13–28.

[*Vermeer et. al., 1972]* D. J. Vermeer, J. W. Meyer, A. K. Oppenheim, *Auto-ignition of hydrocarbon behind reflected shock-waves* , Vol. 18 3:327:336(1972)

[*Versteeg and Malalasekera, 2007]* H. K. Versteeg, W. Malalasekera, *An introduction to computational fluid dynamics, the finite volume method, second edition*, Pearson Education Limited 2007.

[*Vaagsaether and Bjerketvedt, 2005]* K. Vaagsaether, D. Bjerketvedt, *Fourth International Conference on Computational Fluid Dynamics in the Oil and Gas, Metallurgical & Process Industries* Trondheim SINTIF/NTNU Norway 2005.

[*Vaagsaether et. al., 2007]* K. Vaagsaether, V. Knudsen, D. Bjerketvedt, *Simulation of flame acceleration and DDT in H2-air mixture with a flux limiter centered method, International Journal of Hydrogen Energy* , 32, (2007), 2186–2191.

[*Vaagsaether and Bjerketvedt, 2007]* K. Vaagsaether, D. Bjerketvedt, *Simulation of flame acceleration in an obstructed tube with LES* 21st ICDERS, 2007, Poitiers, France.

[*Vaagsaether and Bjerketvedt, 2009]* K. Vaagsaether, D. Bjerketvedt, *Simulation of FA and DDT in a channel with repeated obstacles with an under-resolved mesh*, 22nd ICDERS, 2009, Minsk, Belarus.

[*Warnatz et. al., 1999]* J. Warnatz, U. Maas, R. W. Dibble, *Combustion, Physical and chemical fundamentals, Modeling and simulation, Experiments, Pollutant formation*, 2nd edition, Springer-Verlag Berlin Heidelberg, 1999.

[*Wilcox, 1993]* D. C. Wilcox, *Turbulence modeling for CFD*, 1993, DCW industries, La Canada, California, USA.

[*Williams, 1985]* F. A. Williams, *Combustion theory*, 2nd ed. 1985, Addison-Wesley Publishing Company, Redwood City, USA.

[*Zel'dovich, 1940]* Ya. B. Zel'Dovich, *On the theory of the propagation of detonations in gaseous systems*, Journal of Experimental and Theoretical Physica (1940) Vol.10 542-568

[*Zel'dovich and Kompaneets, 1960]* Ya. B. Zel'dovich, A. S. Kompaneets, *Theory of detonations* pp. 185-191. Academic Press (1960).

[*Zeldovich, 1970]* Ya. B. Zeldovich, V. B. Librovich, G. M Makhviladze,G. I Sivashinsky, *On the development of detonation in a non-uniformly preheated gas. Astronautica Acta* (1970) 15:313321.

List of Figures

List of Tables

Appendix A

Papers

Paper 1 K. Vaagsaether, S. O. Christensen and D. Bjerketvedt: *Modeling and image analysis of FAE*, MABS 20, 2008.

Paper 2 K. Vaagsaether, V. Knudsen and D. Bjerketvedt: *Simulation of flame acceleration and DDT in H_2-air mixtures with a flux limiter centered method*, International Journal of Hydrogen Energy 32, 2007, 2186–2191.

A.1 Modeling and image analysis of FAE

(13 pages)

Modeling and image analysis of FAE

K. Vaagsaether[1], S. O. Christensen[2], D. Bjerketvedt[1]

[1] Telemark University College
56 Kjolnes Ring, 3918 Porsgrunn, Norway
[2] The Norwegian Defence Estates Agency (NDEA)
P.O. Box 405 Sentrum, 0103 Oslo, Norway

Introduction

Fuel-air explosives (FAE) are typically liquid fuel dispersed in air by a high explosive charge to make a fuel-air cloud that is detonated. Modeling the FAE detonation wave and the subsequent shock propagation in air can be handled by different methods. In [1] the detonation properties are imposed on a front that propagates with the detonation velocity. A simpler method is to assume constant volume combustion. In this paper an alternative method for simulating detonations in fuel-air mixtures is presented. This method is based on a temperature dependant reaction rate and it was developed for simulation of deflagration and detonation in gas-air mixtures [2]. There are different numerical schemes for handling nearly discontinuous solutions. In this paper a centered total variation diminishing (TVD) scheme is used. These numerical schemes are simpler and faster than upwind TVD schemes, but may introduce more numerical diffusion. For validation of these methods for large scale explosions results from simulations are compared with experiments, both free field and in complex geometries. Free field experimental results are taken from the propylene-oxide tests in the Elk Velvet 2,

3 and 4 trials performed at DRDC at Suffield, Canada in 2005, 2006 and 2007 [3],[4],[5]. The tests with a complex geometry are taken from the Elk Velvet 4 trials. Simulation results are also compared with pressure records and extracted pressure data from the high speed films of the explosions. This technique gives an almost continuous pressure-distance relationship for the shock wave. The objective of this work is to test the numerical scheme with the reaction rate model and compare the simulated pressure and impulses with experimental results of the Elk Velvet FAE trials.

Reaction Models

There are three species in the system, reactants, products and air. A reaction progress variable describes the reaction of propylene-oxide and air and the transport of reactants and products, equations 1 and 2. A passive variable is transported to include air as the third component.

$$\frac{\partial \rho\beta}{\partial t} + \nabla \cdot (\rho\vec{u}\beta) = -\rho\dot{\omega} \tag{1}$$

The reaction rate is described by an Arrhenius type reaction term.

$$\dot{\omega} = A\rho^{0.5}\beta^{1.5} exp\left(-T_a/T\right) \tag{2}$$

Here β is a reaction progress variable, ρ is the mass density, the vector u is the velocity vector, A is a pre-exponential factor, Ta is an activation temperature and T is the gas temperature. The pre-exponential factor A = 4.107 m1.5/(kg0.5s) and activation temperature Ta = 15000 K where chosen to give the detonation velocity and the CJ-state with a 1D detonation of propylene-oxide and air. A different and simpler way of calculating the source is to assume the whole cloud is burned as a constant volume process. The initial conditions are the products of a constant volume process with a constant pressure, calculated from equation 3, and a heat capacity ratio for the products set in the cloud volume.

$$p_{CV} = (\gamma_{CV} - 1)\left(q + \frac{p_0}{\gamma_0 - 1}\right) \tag{3}$$

Here q is the released heat pr. unit volume, p_{CV} is the constant volume combustion pressure, γ_{CV} is the heat capacity ratio of the products burned by a constant volume reaction, p_0 is the ambient pressure and γ_0 is the heat capacity ratio of the cloud.

Pressure Records

The pressure sensors used in the experiments are all piezoresistive sensors from Kulite. The free field transducers are placed in a 0.4 m X 0.4 m aluminum plates. The logging speed was 65.536 kHz/channel. More detail from the Elk Velvet 3 trials can be seen in [7].

Image Analysis

The image analysis of the high-speed film of the experiments are based on background oriented schlieren (BOS). This method is described in more detail by Sommersel et. al. [8]. The principle can be seen in Figure 1, where an unperturbed image is subtracted from a perturbed image to produce an image where the shock wave is seen more clearly. The position of the shock wave can then be extracted and with a logarithmic transformation and curve fitting the shock Mach-number can be found. The curve fitting of the position is done with the Matlab polyfit script. The shock pressure can be calculated from the normal shock relations as shown in equation 4.

$$\frac{\Delta p}{p_0} = \frac{2\gamma}{\gamma + 1}\left(M^2 - 1\right) \tag{4}$$

Figure 1: The principle of the BOS-technique, the first image is a frame from the high speed movie with an vaguely visible shock, the second image is an unperturbed image and the third image is the difference of the two first images with a clearly seen shock wave.

Numerical and experimental set-up

Explosions in two different geometries has been simulated. One geometry is two-dimensional (2D) axis symmetric sylindrical shown in Figure 2. This

is for comparison with free field measured pressures. The other geometry is a three-dimensional (3D) Cartesian with a structure shown in Figure 3 and computational domain shown in Figure 4. Initial pressure and temperature in the experiments was 92.2 kPa and 281 K for all experiments. The detonation was initiated by a high explosive charge placed approximately 1 m above ground, this is simulated by a high pressure and temperature region. The two explosive sizes of 55 kg and 166 kg of propylene-oxide gives different cloud sizes, the approximate size of the clouds is taken from the film of the experiments. The size of the cloud is also the basis for the calculation of the released energy pr. mass. The cloud is assumed to be pancake-shaped. For the case with 55 kg of fuel the radius of the cloud is 6.8 m and height of the cloud is 2.8 m. For the 166 kg cloud the radius is 9.8 m and the height is 3.9 m. The thermodynamic package SuperSTATE is used to calculate the heat release, q and thermodynamic properties of the species, for the average homogeneous stoichiometry of the cloud.

Free Field

Results from simulations with 2D axis symmetry are compared with free field pressures. Figure 2 shows the computational domain, with the two simulation directions radial, r and axial, z. The radial axis, at z = 0 is the ground. Two different mesh sizes is used to test the grid dependency of the method, 5 cm in r and z direction and 10 cm in both directions. These tests are done with a fuel mass of 55 kg.

Container Observation Post (COP)

The computational domain with the initial FAE cloud is shown in Figure 3. The center of the gas cloud is placed 20 m from the center of the Container Observation Post (COP). The figure shows the domain in the horizontal plane with outer boundaries. The two boundaries normal to X-Y directions are the bottom and top boundaries. The bottom boundary is a wall (ground) and the top is set to a zero gradient boundary. Length X is 28 m, width Y is 40 m and height Z, normal to the X-Y is 20 m. The spacing of the computational mesh for the cases with COP is 0.2 m in all directions. Experiments and simulations are done with both 55 kg and 166 kg of fuel. In Figure 4 the geometry of the structure and the position of the pressure transducers is shown. This is how the geometry is in the simulations however there are some small differences from the real structure. Figure 5 shows an image of the geometry.

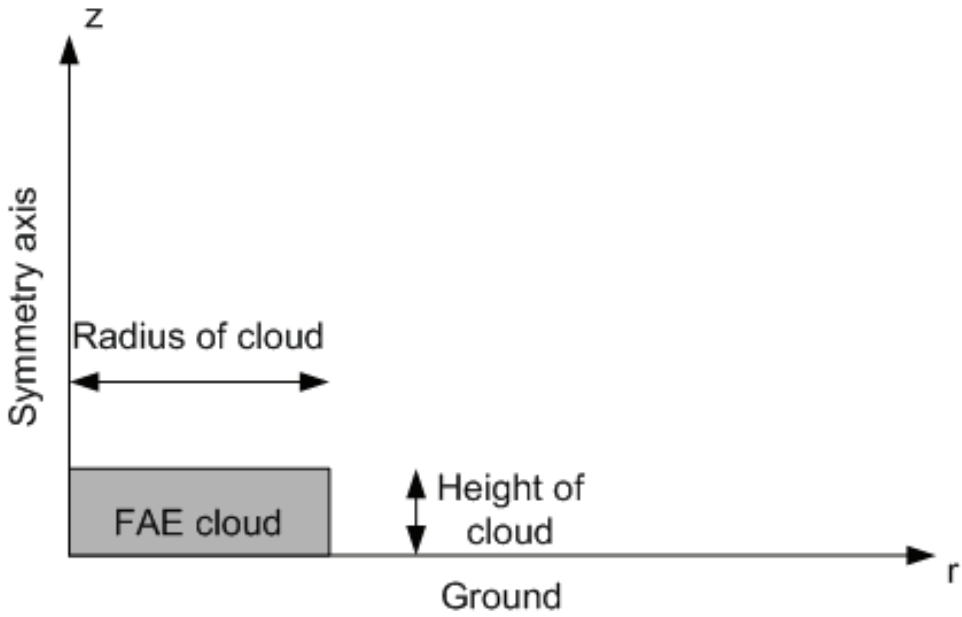

Figure 2: Computational domain for two dimensional axis symmetric calculations.

Results

Free Field

The results from the free field simulations are presented as shock pressure and positive impulse as a function of a reduced length. The reduced length is distance from the center of the cloud divided by the cubed root of the ratio of theoretical released energy, E0 and ambient pressure, p0. The released energy is the product of the heat of combustion and the mass of propylene-oxide, E0 = Hc.mfuel. Where Hc is 30 MJ/kg and mfuel is 55 kg or 166 kg. This scaling is the same as for the TNO multi-energy method [9]. The Simulation 5 cm mesh, 55 kg is simulation results of 55 kg of propylene-oxide with 5 cm mesh spacing. The same notation is used for the other cases. The Constant Volume graph is the constant volume combustion products initial conditions with 5 cm mesh spacing. The experimental results shown in Figure 6 and Figure 7 are experiments with 55 kg and 166 kg of mass. Figure 6 displays the shock front pressure and Figure 7 shows the maximum impulse.

Figure 8 shows results of the free field experiments together with a 2D

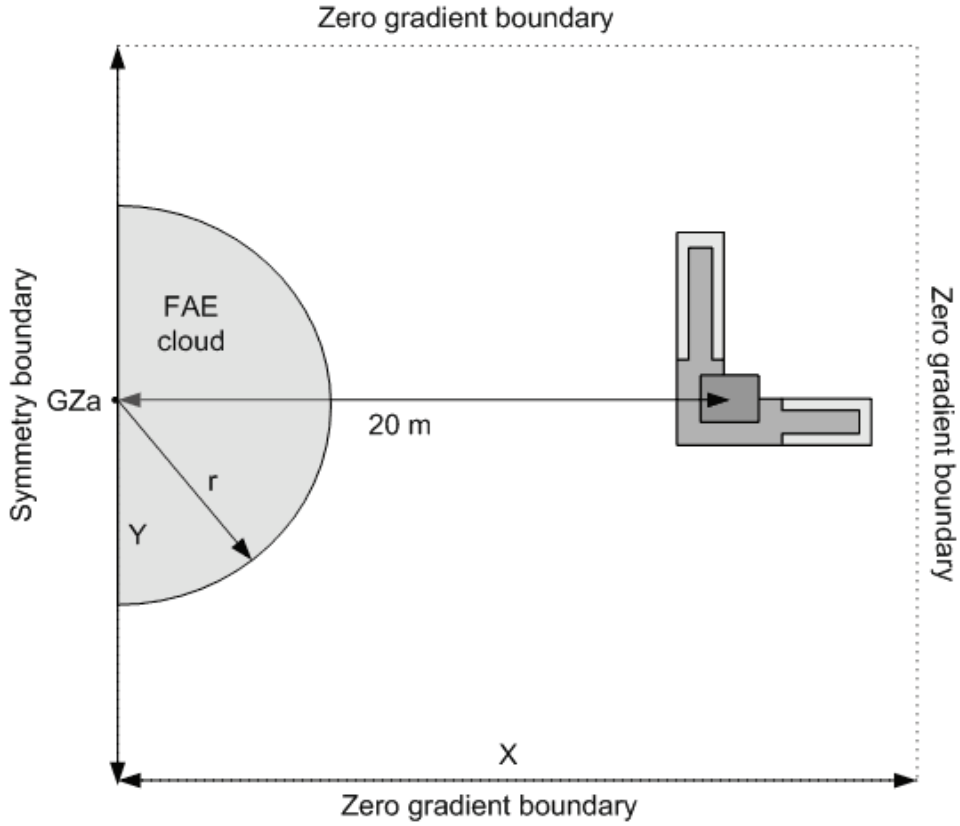

Figure 3: Horizontal plane of the computational domain for the 3D geometry with boundary conditions.

simulation of 55 kg fuel and the predicted pressure from the image analysis method. The 2. order and 3. order curves are for 2. and 3. order interpolation of the Mach-number based on shock positions from the high-speed movies. The 2. and 3. order interpolation of the 55 kg experiment are indistinguishable. For the experiments with 166 kg, the front of the COP started at a reduced distance of approximately 0.65. The shock interacts with the COP at this distance and will contribute to the discrepancies between the 2. order and 3. order interpolation of the position and between the 166 kg and 55 kg cases.

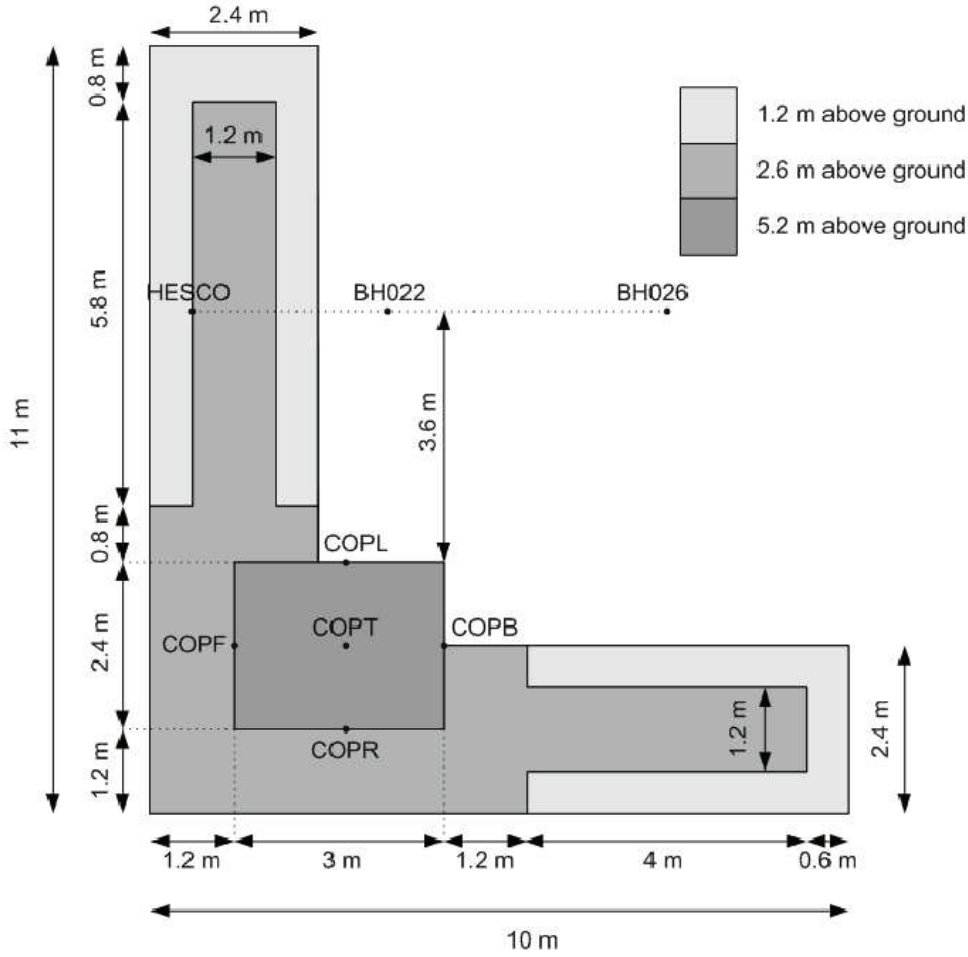

Figure 4: The COP geometry with positions for pressure transducers.

COP

Figure 9 and Figure 10 shows experimental and 3D simulated pressure and impulse as a function of time at the COPF pressure transducer, see Figure 4 for details.

For comparison of experiments and simulations Table 1 and Table 2 displays the maximum pressure and impulse for all pressure transducers. Table 1 is for 55 kg of fuel and Table 2 is for 166 kg of fuel, see Figure 4 for details on the positions of the transducers.

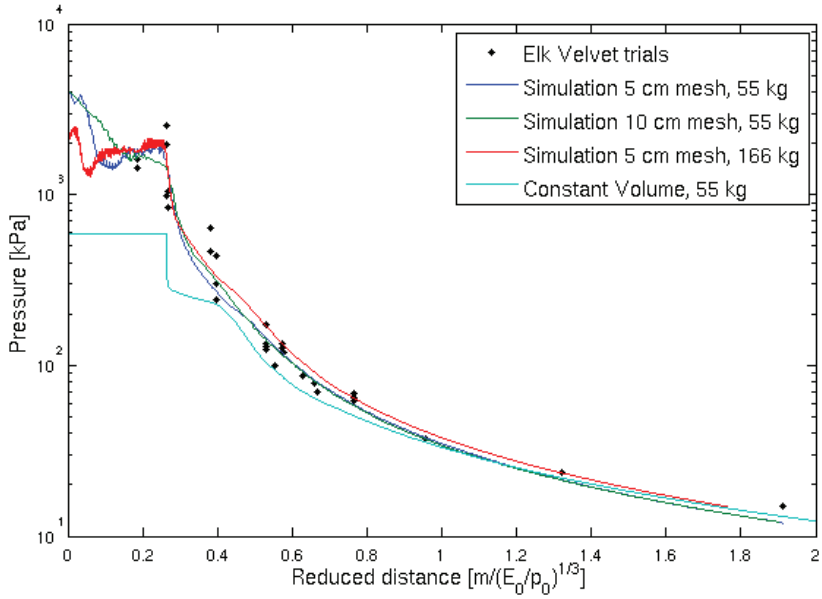

Figure 5: Simulated (2D) and experimental shock pressure along the reduced distance, scaled by energy. The Elk Velvet trials and are either 55 kg or 166 kg of propylene-oxide.

Table 1: Maximum pressure and impulse from experiments and simulations with 55 kg propylene-oxide.

Pressure Transducer	Pressure experiments [kPa]	Pressure simulations [kPa]	Impulse experiments [kPa · ms]	Impulse simulations [kPa · ms]
HESCO	160	163	776	772
BH022	30	25	327	302
BH026	28	28	315	307
COPF	170	154	723	693
COPL	53	49	230	262
COPR	52	50	323	342
COPB	29	24	315	267
COPT	42	44	328	334

Discussion

The free field 2D simulations in Figure 6 and Figure 7 show good agreement with the experiments. The simulated shock pressure is lower than the exper-

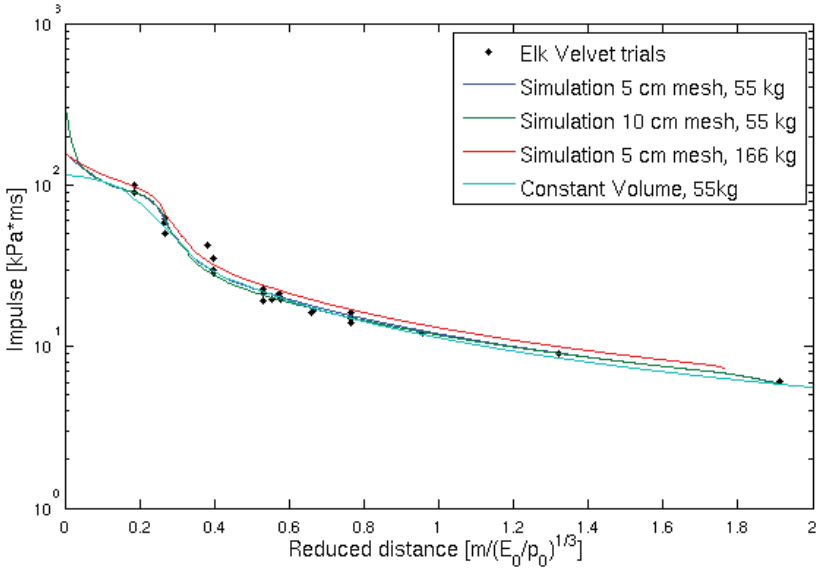

Figure 6: Simulated (2D) and experimental maximum impulse along the reduced distance, scaled by energy. The Elk Velvet trials and are either 55 kg or 166 kg of propylene-oxide.

Table 2: Maximum pressure and impulse from experiments and simulations with 166 kg propylene-oxide.

Pressure Transducer	Pressure experiments [kPa]	Pressure simulations [kPa]	Impulse experiments [kPa · ms]	Impulse simulations [kPa · ms]
HESCO	536	466	1820	1768
BH022	64	52	609	543
BH026	72	61	593	572
COPF	404	394	1524	1484
COPL	115	98	603	579
COPR	122	99	371	403
COPB	57	39	589	477
COPT	95	82	605	536

imental pressure far away from the source. This is likely due to numerical diffusion as the pressure peak is smoothed over a few control volumes. This effect is not seen in the impulse, as the energy is not dissipated due to the

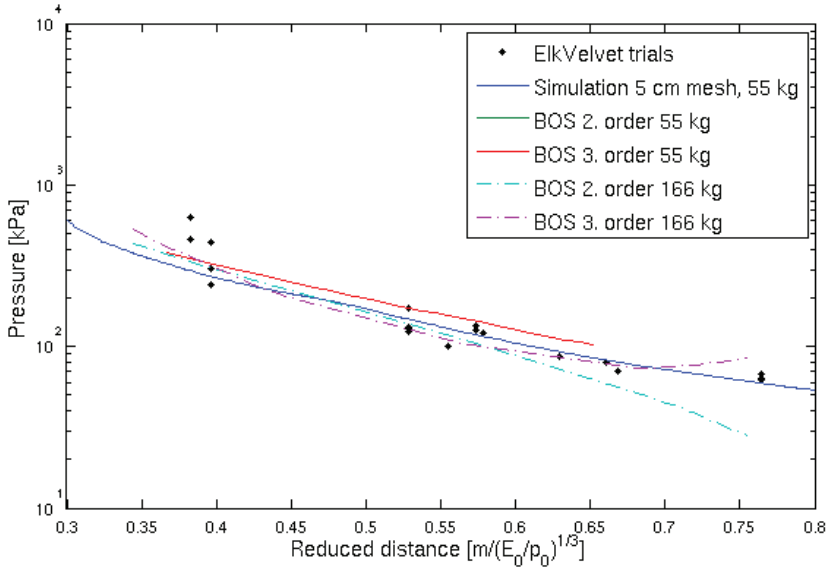

Figure 7: Free field experimental data together with simulations of a 55 kg FAE and results from the image analkysis. The 2. and 3. order interpolation for 55 kg are equal and can not be distinguished.

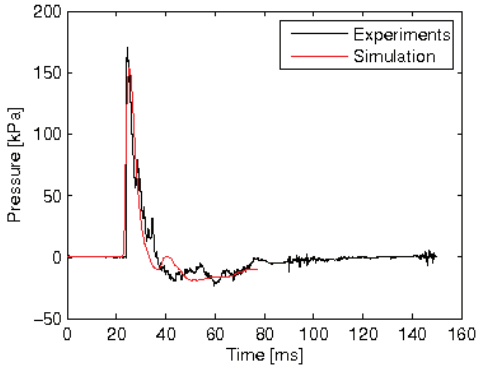

Figure 8: Experimental and simulated pressure history at pressure sensor COPF for 55 kg of propylene-oxide.

numerical diffusion. The mesh size does not seem to effect the performance too much for the 2D axis symmetric simulation. The 166 kg cloud produce stronger shock, based on the cloud sizes this cloud is richer than the 55 kg

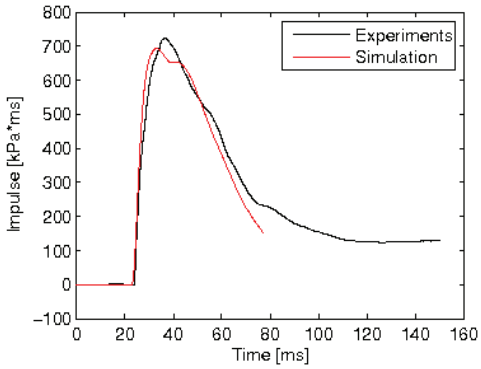

Figure 9: Experimental and simulated impulse history at pressure sensor COPF for 55 kg of propylene-oxide.

cloud, and the mixture is closer to the CO stoichiometric concentration on average. The released energy pr. unit volume is therefore higher for the 166 kg cloud than for the 55 kg cloud. By setting the same initial FAE cloud volume as a constant volume combustion products state the results are quite good compared with the experimental results. The pressures are in some degree under-predicted near the cloud but the impulse is equally good as for the reaction rate. For a system like this where there are no structures within the FAE cloud, the constant volume method might be as good a method as a reaction rate model. The reaction rate model may handle shock reflections and more complicated wave structures in the cloud but this may not be important in many cases. The image analysis is taken from high speed films of the shock close to the COP, for the 166 kg FAE the shock was above the walls of the COP and the results after a reduced length of 0.65 is not comparable to the free field data as presented in Figure 8. The extracted shock pressure from the high speed films are in good agreement with simulation data and experimental pressure records. For the three dimensional simulations the pressure and impulse show a good agreement with experiments. Figure 9 and Figure 10 and Table 1 and Table 2 shows the results for these experiments and simulations. The strength, time of arrival and the duration of the blast wave is reproduced in the simulations, with some discrepancies in the pressure history. The secondary shock is predicted later than in the experiments and is then seen in the negative phase. This might be a numerical diffusion problem and in this case the mesh is coarse. Since the predicted impulse follows the experimental impulse quite well this is probably not too important for the analysis.

Conclusion

The 2D and 3D simulation methods described in this paper can reproduce the loading from blast waves from FAE. The predicted pressures and impulses are in good agreement with the experimental results both for the free field experiments and for the tests with a COP. Some effects from numerical diffusion are seen in the far field pressures, but the impulse is not affected by this. The constant volume combustion source gives reasonable results for the impulse but the pressure is under-predicted near the cloud. The image analysis based on BOS is also able to reproduce experimental pressures from a high speed film of a shock wave and may also be helpful in validating CFD methods. We conclude that the FLIC scheme with the reaction rate model can produce pressure and impulses that agrees quite well with experimental results of fuel-air explosives.

Bibliography

[1] Murray, S. B., Gerrard, K. B., 1996, On the detonability and blast from propylene-oxide and nitromethane droplet-air clouds, The Second International Specialist Meeting on Fuel-Air Explosions, Bergen, Norway

[2] Vaagsaether, K., Bjerketvedt, D., 2007, Simulation of flame acceleration in an obstructed tube with LES, 21. ICDERS, Poitiers, France

[3] Christensen, S. O. and Skudal, S., 2005, Blast testing of Norwegian observation posts, Elk Velvet 2.5 and 2.6, Forsvarsbygg / Norwegian Defence Estates Agency, Oslo, Norway, LIMITED DISTRIBUTION

[4] Christensen, S. O. and Skudal, S, 2006, Elk Velvet 3: Blast testing of Container Observation Post and Tent, Forsvarsbygg / Norwegian Defence Estates Agency, Oslo, Norway, RESTRICTED

[5] Skudal, S. and Christensen, S. O., 2007, Elk Velvet 4: Blast and fragment testing of Container Observation Post, Forsvarsbygg / Norwegian Defence Estates Agency, Oslo, Norway, RESTRICTED

[6] Toro, E. F., 1999, Riemann Solvers and Numerical Methods for Fluid Dynamics: A Practical Introduction, Berlin, Heidelberg, Germany, Springer-Verlag

[7] Christensen, S. O. and Skudal, S., 2006, Blast vulnerability of personnel in a container based observation, MABS 19, Calgary, Canada.

[8] Sommersel, O. K., Bjerketvedt, D., Christensen, S. O., Krest, O., Vaagsaether, K. 2008, Application of background oriented schlieren for quantitative measurements of shock waves from explosions, Shock Waves, DOI 10.1007/s00193-008-0142-1

[9] van den Berg, A. C. 1985, The multi-energy method A framework for vapour cloud explosion blast prediction, Journal of Hazardous Materials, Volume 12 Issue 1, 1-10.

A.2 Simulation of flame acceleration and DDT in H_2-air mixtures with a flux limiter centered method

(19 pages)

SIMULATION OF FLAME ACCELERATION AND DDT IN H_2-AIR MIXTURE WITH A FLUX LIMITER CENTRED METHOD

Vaagsaether, K.[1], Knudsen, V.[1] and Bjerketvedt, D.[1]

[1]Department of Technology, Telemark University College, Kjolnes Ring 56, Porsgrunn, NO-3918, Norway

Abstract

Flame acceleration and deflagration to detonation transition (DDT) is simulated with a numerical code based on a flux limiter centered method for hyperbolic differential equations [1]. The energy source term is calculated by a Riemann solver for the inhomogeneous Euler equations for the turbulent combustion and a two-step reaction model for hydrogen-air. The transport equations are filtered for large eddy simulation (LES) and the sub-filter turbulence is modelled by a transport equation for the turbulent kinetic energy [2]. The flame tracking is handled by the G-equation for turbulent flames [3]. Numerical results are compared to pressure histories from physical experiments. These experiments are performed in a closed, circular, 4 m long tube with inner diameter of 0.107 m. The tube is filled with hydrogen-air mixture at 1 atm, which is at rest when ignited. The ignition is located at one end of the tube. The tube is fitted with an obstruction with circular opening 1 m down the tube from the ignition point. The obstruction has a blockage ratio of 0.92 and a thickness of 0.01 m. The obstruction creates high pressures in the ignition end of the tube and very high gas velocities in and behind the obstruction opening. The flame experiences a detonation to deflagration transition (DDT) in the supersonic jet created by the obstruction. Pressure build-up in the ignition end of the tube is simulated with some discrepancies. The DDT in the supersonic jet is simulated, but there is a discrepancy in the time of the simulated DDT.

NOMENCLATURE

C_S	Smagorinsky constant
C_ε	destruction of turbulence constant
E	energy per volume
F	flux of conserved variables
k	turbulent kinetic energy
p	pressure
q	heat released per mass
r	slope strength
S	strain rate tensor
S_T	turbulent burning velocity
t	time variable
T	temperature
u	velocity component
u	velocity vector
U	conserved variable
v_f	particle velocity in front of flame
x	spatial variable
z	reaction variable
α	radical reaction variable
Δ	filter length scale
κ	thermal diffusivity

ν kinematic viskosity

ν_t turbulent kinematic viscosity

ρ density

σ_t turbulent Prandtl number

τ turbulent shear stress

ϕ flux limiter

1.0 INTRODUCTION

A numerical code for 1D, 2D and 3D simulations of combustion processes, including detonations and deflagration to detonation transition (DDT), is proposed. The code is based on a 2^{nd} order accurate total variation diminishing (TVD), flux limiter centered scheme. The goal of this project is to create a code that can simulate the propagation of a combustion wave from a weak ignition to detonation. Since the detonation wave is a shock wave, and the flame creates shock waves, a TVD method must be used as the numerical scheme. The TVD scheme ensures capturing of discontinuities in the solution. A 2^{nd} order centered scheme is chosen because of its simplicity and computational speed, but it may smoothen shocks over more computational cells than a upwind scheme. Khokhlov and Oran [4] have done numerical experiments with DDT from a flame brush, but with direct numerical simulation (DNS). Vaagsaether and Bjerketvedt have tested the ability of the scheme to simulate turbulence in compressible, supersonic flow [5]. Numerical experiments are compared with physical experiments by Knudsen et.al. [6] that are executed in a 4 m long circular tube that is closed in both ends. The tube is fitted with an obstruction to create turbulence and high gas velocities. The codes ability to simulate non-reactive flow have been

validated with theoretical and physical experiments, as well. The physical experiments are tests with high explosives in complex geometries. These tests will not be presented in this paper.

2.0 NUMERICAL SCHEME AND MODELS

The codes solution process is first to solve the hyperbolic part of the differential equations in one direction with the FLIC scheme. Then the other terms of the equations are solved with the time dependent term. The numerical scheme is explained in detail in chapter 2.1. The turbulence model is explained in chapter 2.2 and the combustion models are explained in chapter 2.3.

2.1 Numerical Scheme

TVD schemes for convective transport are constructed for hyperbolic PDEs, such as the Euler equations shown in equations 1 and 2. The equations are discretised on a LES grid, and are filtered with a box filter or top-hat filter in physical space. The numerical scheme is created for one space dimension.

$$\frac{\partial \mathrm{U}}{\partial t} + \frac{\partial \mathrm{F(U)}}{\partial x} = 0 \tag{1}$$

$$\mathrm{U} = \begin{bmatrix} \overline{\rho} \\ \overline{\rho}\widetilde{u} \\ \widetilde{E} \end{bmatrix} \quad \mathrm{F} = \begin{bmatrix} \overline{\rho}\widetilde{u} \\ \overline{\rho}\widetilde{u}^{\,2} + \widetilde{p} \\ \widetilde{u}\left(\widetilde{E} + \widetilde{p}\right) \end{bmatrix} \tag{2}$$

The FLIC scheme is a 2nd order accurate centred flux-limiter scheme that combines the 1st order accurate FORCE scheme and the 2nd order Richtmyer version of the Lax-Wendroff scheme. The FORCE flux is a deterministic version of the Random Choice Method, where the stochastic steps of the RCM are replaced by integral averages of the Riemann problem solutions. One outcome of this is that the FORCE flux is the

arithmetic mean of the Richtmyer flux and the Lax-Friedrich flux. The 1st order Lax-Friedrich flux is defined in equation 3.

$$F^{LF}_{i+\frac{1}{2}} = \frac{1}{2}\left[F(U_L) + F(U_R)\right] + \frac{1}{2}\frac{\delta x}{\delta t}\left[U_L - U_R\right] \tag{3}$$

Subscript L and R denotes the left and right cell of an inter cell boundary. The 2nd order Richtmyer flux is defined by the intermediate states of the conserved variables as shown in equation 4.

$$U^{RI}_{i+\frac{1}{2}} = \frac{1}{2}\left[U_L + U_R\right] + \frac{1}{2}\frac{\delta t}{\delta x}\left[F(U_L) - F(U_R)\right] \tag{4}$$

$$F^{RI}_{i+\frac{1}{2}} = F(U^{RI}_{i+\frac{1}{2}}) \tag{5}$$

And the FORCE flux

$$F^{FORCE}_{i+\frac{1}{2}} = \frac{1}{2}\left[F^{LF}_{i+\frac{1}{2}} + F^{RI}_{i+\frac{1}{2}}\right] \tag{6}$$

The flux limiters control the order of the scheme. For areas where the solution is smooth, the scheme is 2nd order accurate or close to 2nd order. For areas with discontinuous solutions the scheme is 1st order accurate. A measure of the smoothness of the solution is needed to construct the flux limiter. Since the total energy includes all wave families, it is a good choice for the defining variable of the flux limiter. The slope r is defined for the left and right inter cell boundary

$$r^{L}_{i+\frac{1}{2}} = \frac{\delta E_{i-\frac{1}{2}}}{\delta E_{i+\frac{1}{2}}} \quad r^{R}_{i+\frac{1}{2}} = \frac{\delta E_{i+\frac{3}{2}}}{\delta E_{i+\frac{1}{2}}} \tag{7}$$

The different flux limiters are displayed in figure 1 graphically. These limiters are constructed based on the TVD region bounded by the SUPERBEE and MINBEE limiters. The SUPERBEE limiter is the least diffusive limiter possible and may induce small oscillations around strong gradients. MINBEE is the most diffusive limiter. In this study the MC-limiter [7] is used for all simulations.

The flux limiter for the inter cell boundary i+1/2 is chosen as the smallest limiter value of the left and right slopes.

$$\phi_{i+\frac{1}{2}} = \min\left(\phi(r^{L}_{i+\frac{1}{2}}), \phi(r^{R}_{i+\frac{1}{2}})\right) \tag{8}$$

The FLIC scheme is then written as

$$\mathrm{F}^{FLIC}_{i+\frac{1}{2}} = \mathrm{F}^{FORCE}_{i+\frac{1}{2}} + \phi_{i+\frac{1}{2}}\left[\mathrm{F}^{RI}_{i+\frac{1}{2}} - \mathrm{F}^{FORCE}_{i+\frac{1}{2}}\right] \tag{9}$$

The diffusion terms are solved by time splitting. First the Euler equations are solved by the TVD scheme, then a set of parabolic PDEs, as equation 10, are solved with the initial condition given by the solutions of the Euler equations.

$$\frac{\partial \mathrm{U}}{\partial t} = \frac{\partial}{\partial x}\left(\mathbf{\Gamma}\frac{\partial \mathrm{H}}{\partial x}\right) \tag{10}$$

2.2 Turbulence Model

To model the sub-grid scale turbulence, the code uses a model proposed by Menon et. al. [8]. The model is a conservation equation of the turbulent kinetic energy, k, with a production term and a destruction term, as shown in equations 11-15.

$$\frac{\partial \overline{\rho} k}{\partial t} + \nabla \cdot \left(\overline{\rho} \widetilde{u} k \right) = \nabla \cdot \left(\frac{\nu_t}{\sigma_k} \nabla k \right) + P^{sgs} - D^{sgs} \tag{11}$$

$$P^{sgs} = -\tau_{ij} \frac{\partial \widetilde{u}_i}{\partial x_j} \tag{12}$$

$$\tau_{ij} = -2\overline{\rho} \nu_t \left(S_{ij} - \frac{1}{3} S_{kk} \delta_{ij} \right) + \frac{2}{3} \overline{\rho} k \tag{13}$$

$$\nu_t = C_s k^{\frac{1}{2}} \Delta \tag{14}$$

$$D^{sgs} = \frac{C_v \overline{\rho} k^{\frac{3}{2}}}{\Delta} \tag{15}$$

2.3 Combustion model

The code uses two different methods of solving the chemical reaction terms of the energy equation shown in equation 18. The first method is used if the reaction wave is a laminar or turbulent combustion wave. This method is a Riemann solver based on the solver presented by Teng et. al. [9] that assumes an infinitely thin flame. The reaction variable z is either 0 or 1 depending whether the state is burnt or unburned. The model for the turbulent burning velocity, S_T, eq. 16, is presented by Flohr and Pitsch [8], and is originally for industrial burners.

$$\mathrm{S_T} = \mathrm{S_L} \left(1 + \mathrm{A} \left(\mathrm{Re}_\Delta \, \mathrm{Pr} \right)^{\frac{1}{2}} \mathrm{Da}_\Delta^{-\frac{1}{4}} \right) \tag{16}$$

Where S_L is the laminar burning velocity and:

$$\mathrm{Re}_{\Delta} = \frac{\sqrt{k}\Delta}{\nu}, \quad \mathrm{Da}_{\Delta} = \frac{\Delta}{\sqrt{k}\tau_c}, \quad \tau_c = \frac{\kappa}{S_L^2}$$

This model is filter dependant, which is reasonable since it models the burning velocity influenced by the sub filter turbulence. The model assumes that the flame front is thinner than the filter size, or $Da_{\Delta}>1$. For high levels of turbulence this assumption may not be correct.

$$\frac{\partial G}{\partial t} + v_f \nabla G = S_T |\nabla G| \tag{17}$$

To track the flame, the G-equation for turbulent flames [3], is used, eq. 17. It assumes that the variable G is a smooth function which is positive in burned gas and negative in the unburned gas. The flame front is set as G equals zero. By placing the flame front as a set value of a smooth function the discontinuous nature of the infinitely thin flame can be handled.

$$\frac{\partial\left(\tilde{E} + \bar{\rho}q\tilde{z}\right)}{\partial t} + \nabla \cdot \left(\tilde{u}\left(\tilde{E} + \bar{\rho}q\tilde{z} + \tilde{p}\right)\right) = 0 \tag{18}$$

A second reaction variable, α, which describes the concentration of radicals, is solved as a conserved variable, shown in equation 19. The reaction source term is an Arrhenius function. In the burnt state α is 1 and initially α is 0 in the unburned gas. If the value of α reaches 1 in the unburned gas, the mixture ignites and a second model for the rate of z is used.

$$\frac{\partial \bar{\rho}\tilde{\alpha}}{\partial t} + \nabla \cdot \left(\bar{\rho}\tilde{u}\tilde{\alpha}\right) = r_{\alpha} \tag{19}$$

Equation 20 describes the rate of change of z due to the chemical reactions. The reaction rate model was presented by Korobeinikov et.al. [10].

$$\frac{d\tilde{z}}{dt} = -k_2 \tilde{p}^{n_2} \bar{\rho}^{l_2} \tilde{z}^{m_1} \exp\left(-\frac{E_2}{R\tilde{T}}\right) + k_3 \tilde{p}^{n_3} \bar{\rho}^{l_3} (1-\tilde{z})^{m_2} \exp\left(-\frac{(E_2+Q)}{R\tilde{T}}\right) \quad (20)$$

For the experiments with stoichiometric hydrogen-air in this paper the constants in equation 20 are set as

$l_2=l_3=0$, $n_2=n_3=2$, $m_1=m_2=2$, $k_2=k_3=3.9\cdot10^{-7}$, $E_2=2000$ J/kg, $Q=3.6\cdot10^6$ J/kg

The values of the pre-exponential factors differ in some degree from the Korobeinikov paper. These values are set so the detonation velocity of a 1D detonation matches the CJ-velocity.

3.0 EXPERIMENTS

The numerical experiment is as similar to the physical experiment as possible. The temperature and pressure of both experiments are assumed to be 20^{o}C and 1 atm. In chapters 3.1 and 3.2 the set-up of both types of experiments are explained.

3.1 Experimental setup

The experiment is performed in a 4 m long circular steel tube with inner diameter of 0.107 m. The pipe is closed in both ends and has a spark ignition source in one end. An obstacle with circular opening is fitted 1 m from the ignition source, see figure 2. The opening of the obstacle is 30 mm, which is a blockage ratio of 0.92. This obstacle causes DDT in experiments with stoichiometric hydrogen. The hydrogen-air mixture is filled into the tube at the ignition end at 1 atm and at room temperature. To measure the pressure, six transducers are mounted on the tube. Transducer P0 is mounted at the ignition point. The other transducers are mounted at 0.5 m intervals behind the obstruction, starting at 0.5 m from the obstacle. P0, P1 and P3 are Kistler 7001 type transducers and P2, P4 and P5 are Kistler 603B transducers. The logging speed is 500000 points pr. second. Figure 3 shows the pressure records of the experiment described. The speed of the detonation wave is approximately 2000 m/s. P0 show a slow increase in the

pressure in the ignition end of the tube. The obstacle creates turbulence and reflected waves which influence the flame propagation and reaction rate. The obstacle also creates a jet behind it which is supersonic when the flame passes. The DDT occurs in or at the edge of that jet. Figure 3 shows the experimental pressure records of the described experiment.

3.2 Numerical setup

The geometry of the numerical setup is an approximation of the physical experiments with cylinder coordinates. This is a rough assumption, since the equations are filtered for LES, and the largest length scales of the turbulence are directly simulated. The velocity gradients are strongest in the radial and axial direction because of the geometry, so omitting the tangential direction should not influence the production of turbulence too much. The ignition is approximated by a few computational cells that are set as burnt, this will start the combustion wave. In these numerical experiments the grid resolutions are 2 mm. The number of cells is 2000 in the x-direction and 25 in radial direction. The CFL number is 0.9 for all time steps. For the Smagorinsky model, see for example [11], the Smagorinsky constant is 0.17, according to Lilly [12]. This gives good results for this model for these simulations as well. The value presented by Menon et. al. is 0.067. The constant in the turbulent destruction term in the turbulence model is 0.916, as presented in the paper by Menon et. al. No heat transfer between the gas and the tube wall is modeled in these simulations.

4.0 RESULTS

The simulated pressure matches the pressure from the experiment at ignition end of the tube to some degree, as shown in figure 4. As the flame gets closer to the obstacle, the difference between the numerical results and the experimental results becomes more evident. The sharp pressure peak at around 19 ms in the physical experiment, resulting from the DDT, is simulated at a later time than in the experiment. This is

because the simulated DDT occurs later than in the experiment. This discrepancy may be a result of many factors. The interaction of the flame with the obstacle may not be handled correctly. The boundary conditions for the variable G is not well defined at walls and the flame may not be propagated correctly through the obstacle. The modeled turbulence and burning velocity are also important factors that may contribute to the discrepancies. The assumption of $Da_{\Delta} > 1$ is satisfied throughout the simulation and the flame thickness is thus smaller than the grid size. Another likely factor that may create discrepancies is that the grid size may be too large, so that a possibly simulated hot spot may be averaged to a too low temperature that will not produce a DDT. There may also be effects from the tangential direction. DDT may be a strictly 3D phenomena and reflected and focused shocks should then be simulated in 3D as, of course, the turbulence. The flow has a simulated Mach-number of about 2.2 in the jet before the flame passes the obstacle, as shown in figure 5. This creates oblique shocks and expansion waves. Figures 6 and 7 show the pressure histories at sensor P2 and P5, where it can be seen that the pressure level and propagation speed of the detonation wave is simulated accurately. There is an offset of just over 2 ms between the simulated and the experimental detonation front both at transducer P2 and P5. This indicates that the constants in the reaction rate model used for reaction variable z is good enough to predict the reaction of a stoichiometric mixture of hydrogen-air in a detonation wave, and that the reaction rate for variable α, which calculates the induction time, is good enough as well. The higher simulated pressures in the detonation front may be due to the sample rate and rise time in the pressure sensors. The pressure is logged every 2 s for the physical experiments and about every 0.5 s for the simulation.

5.0 CONCLUSION

The code shows promising results for simulating laminar- and turbulent combustion waves, DDT and detonation waves, but more validation is still needed. The simulation results are showing some errors compared with the physical experiment with this set-up. It is impossible to say if the position of the DDT

is simulated correctly with these results, but it seems that the DDT is simulated too far behind the obstacle, since it occurs later than in the experiment. This may be a result of a too coarse grid or the boundary conditions in the flame propagation model. The assumption of 2D is also a probable reason for the errors in the simulation of DDT. The detonation wave is simulated nearly correctly, which indicates that the two-step model is working satisfactory with the constants presented here for stoichiometric hydrogen-air. The grid resolution is too coarse to resolve any instabilities in the detonation front. The simulation result shows only a planar detonation front. In the experiments this will probably be an unstable detonation with cell width of about 1 cm. The most important future work with this code is to improve the implementation of the G-equation, specifically the boundary conditions at walls. This equation controls the flame propagation and is very important for the simulation of the turbulent combustion waves. Adaptive mesh refinement may also produce better results, because it is then possible to use a finer mesh around the reaction front and shock fronts and a coarse mesh away from the fronts to save computing time.

REFERENCES

1. Toro, E.F., Riemann Solvers and Numerical Methods for Fluid Dynamics, A Practical Introduction, 1999, Springer-Verlag Berlin Heidelberg.
2. Menon, S., Sankaran, V., Stone, C., Subgrid Combustion Modelling for the Next Generation National Combustion Code, 2003, NASA Glenn Research Center NASA/CR-2003-212202.
3. Peters, N., Turbulent Combustion, 2000, Cambridge University Press, United Kingdom.
4. Khokhlov, A. M. and Oran, E. S., Numerical Simulation of Detonation Initiation in a Flame Brush: The Role of Hot Spots, 1999, Combustion and Flame 119:400-416.

5. Vaagsaether, K., Bjerketvedt, D., Simulation of Supersonic Shear Layers with High Resolution TVD Methods, Fourth International Conference on CFD in the Oil and Gas, Metallurgical & Process Industries, 6-8 June 2005, Trondheim, Accepted.
6. Knudsen, V., Vaagsaether, K., Bjerketvedt, D., Experiments with hydrogen-air explosions in a closed pipe with a single obstacle, Proceedings of the European Combustion Meeting, 3-6 April, 2005, Louvain-la-Neuve.
7. Leveque, R., Finite Volume Methods for Hyperbolic Problems, 2002, Cambridge University Press, United Kingdom.
8. Teng, T.H., Chorin, A.J., Liu, T.P., Riemann Problems for Reacting Gas, with Applications to Transition, 1982, SIAM J. Appl. Math. Vol. 42 No. 5, pp. 964-981.
9. Flohr, P., Pitsch, H., A Turbulent Flame Speed Closure Model for LES of Industrial Burner Flows, 2000, Center for Turbulence Research, Proceedings of the Summer Program
10. Korobeinikov, V. P., Levin, V. A., Markov, V. V., Chernyi, G. G., Propagation of Blast in a Combustible Gas, 1972, Astronautica Acta. Vol. 17, pp. 529-537.
11. Poinsot, T. and Veynante, D., Theoretical and Numerical Combustion, 2001, R. T. Edwards, USA
12. Lilly, D. K., The Representation of Small-Scale Turbulence in Numerical Simulation Experiments, 1967, In. Proc. IBM Scientific Computing Symp. Environ. Sci., pp. 195.

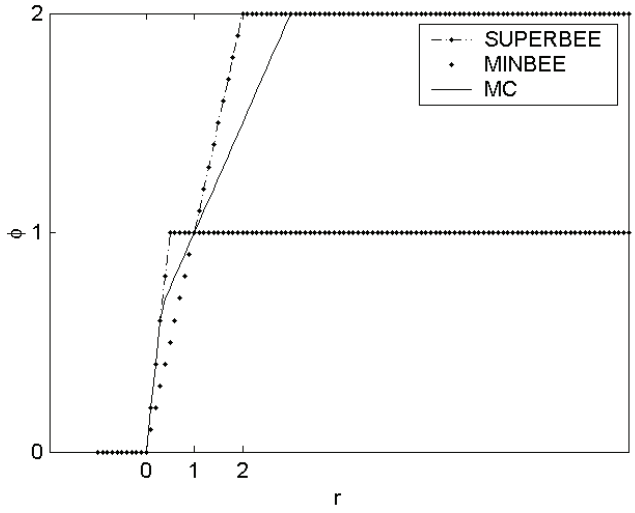

Figure 1. Flux limiters as function of r.

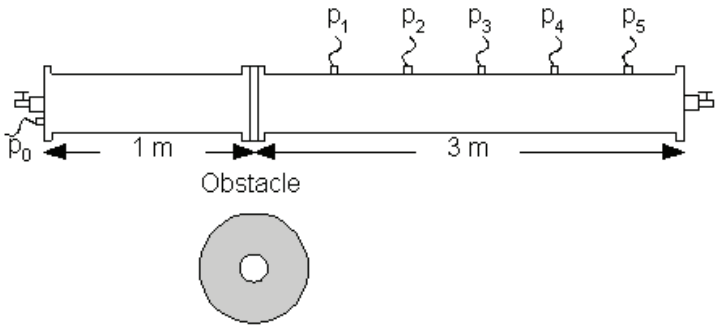

Figure 2. Experimental tube and pressure transducer configuration.

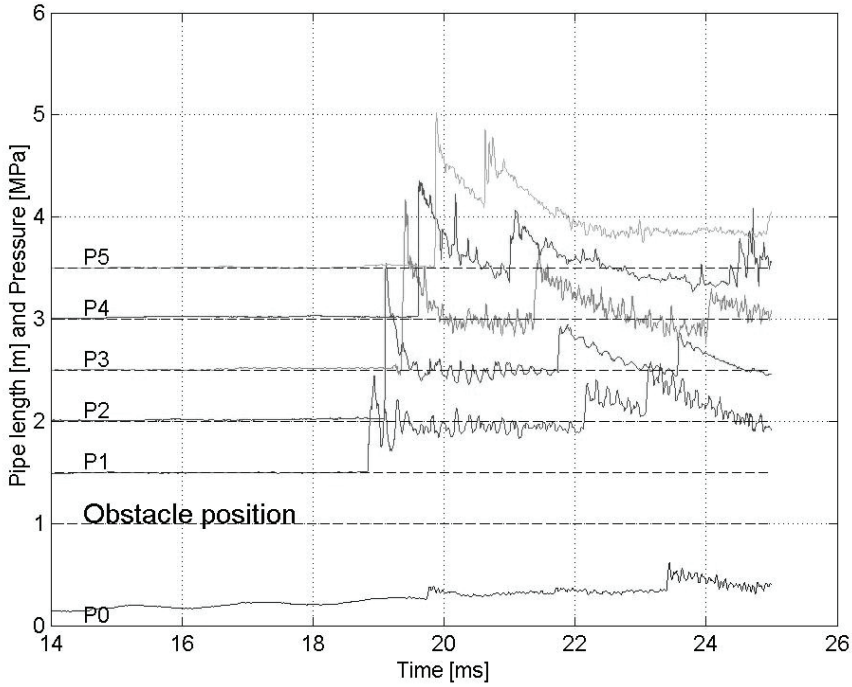

Figure 3. Pressure record from the physical experiment.

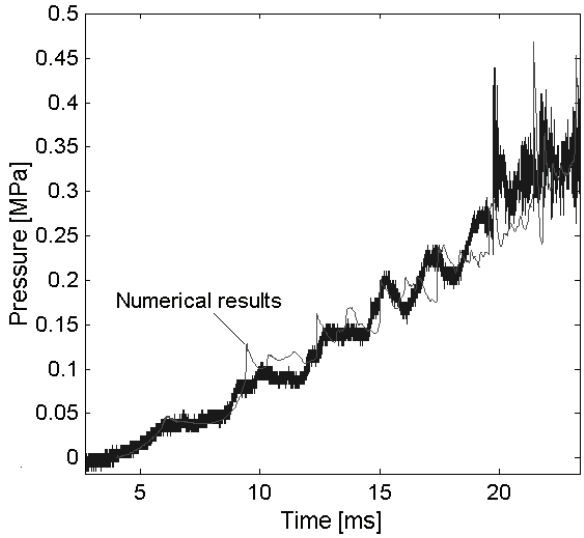

Figure 4. Pressure histories from numerical and physical experiment at transducer P0.

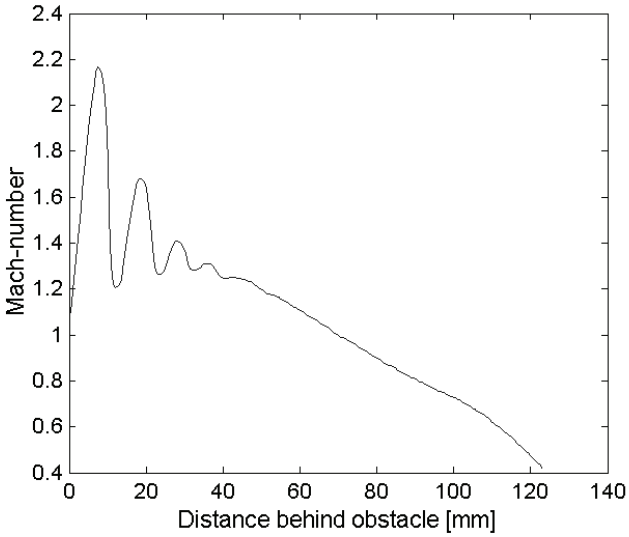

Figure 5. Simulated Mach-number behind obstacle at central axis. The flame is 20 mm in front of the obstacle.

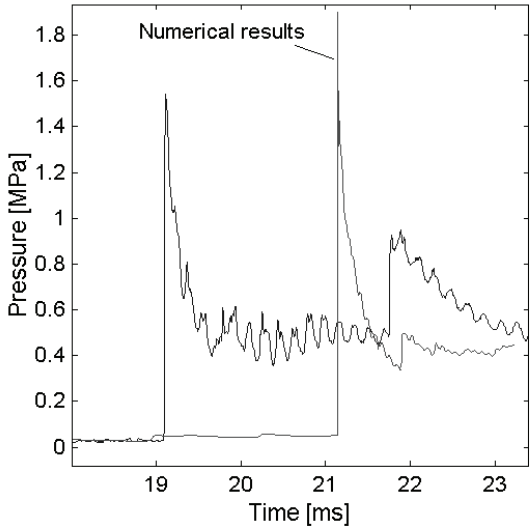

Figure 6. Pressure histories from numerical and physical experiment at transducer P2.

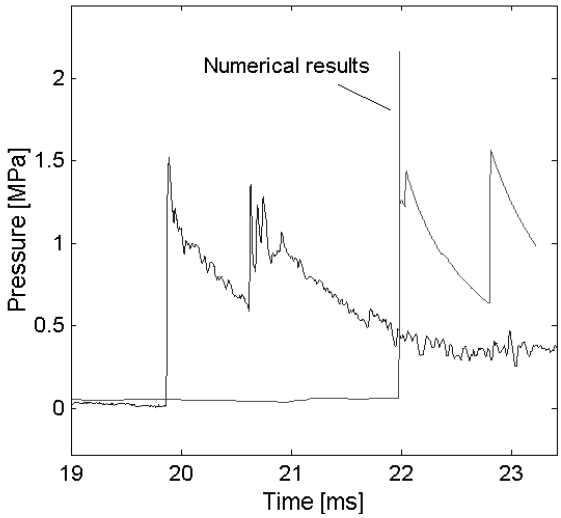

Figure 7. Pressure histories from numerical and physical experiments at transducer P5.

Appendix B

Riemann solver for combustion waves

Riemann solver for combustion waves

Thin flame RH exact Riemann solver

This Riemann solver for combustion waves is based on the solver by Teng et.al [1]. The main difference is that two different values for γ can be used, one for the unburned state and one for the burned state. This solver needs a known burning velocity and it does not allow combustion fronts faster than CJ-deflagrations. Figure 1 shows the characteristics of the wave structures with a combustion wave. A Riemann solver relates the states behind the waves, here U_0 and U_I, to the known right and left states U_R and U_L. These states are connected by the eigenvectors and eigenvalues of the system. From the general Riemann solver a right wave connects the U_0 and U_R states if:

$$\psi(p_0; p_R, \rho_R) = \begin{cases} (p_0 - p_R)\sqrt{\frac{A_R}{p_0 - B_R}} & for \quad p_0 > p_R \\ \frac{2c_R}{\gamma_R - 1}\left(\frac{p_0}{p_R}\right)^{\left(\frac{\gamma_R - 1}{2\gamma} - 1\right)} & for \quad p_0 \leq p_R \end{cases} \tag{1}$$

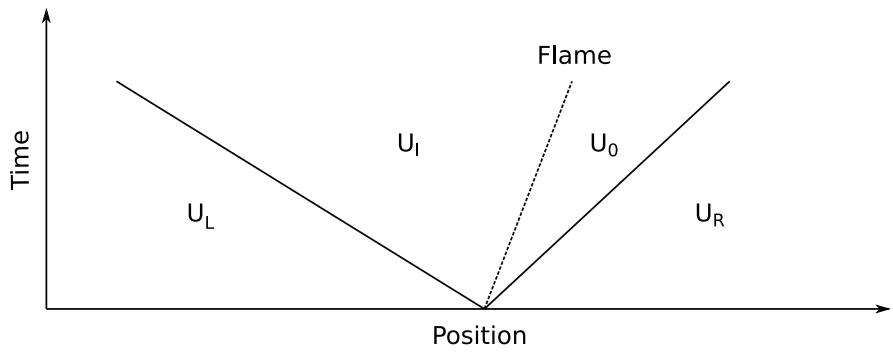

Figure 1:

$A_R = \frac{2}{\rho_R(\gamma_R+1)}$
$B_R = p_R\frac{\gamma_R-1}{\gamma_R+1}$
The U_L and U_I states are connected by left wave if

$$\psi(p_I; p_L, \rho_L) = \begin{cases} (p_I - p_L)\sqrt{\frac{A_L}{p_I - B_L}} & for \quad p_I > p_L \\ \frac{2c_L}{\gamma_L - 1}\left(\frac{p_I}{pL}\right)^{\left(\frac{\gamma_L-1}{2\gamma}-1\right)} & for \quad p_I \leq p_L \end{cases} \tag{2}$$

where
$A_L = \frac{2}{\rho_L(\gamma_L+1)}$
$B_L = p_L\frac{\gamma_L-1}{\gamma_L+1}$
For a deflagration wave U_I and U_0 are connected by the deflagration solution in the Rankine-Hugoniot relations. Conservation of mass, momentum and energy equations 3, 4 and 5 express the relations between the two states. Either by expressing U_I as a function of U_0 or U_0 as a function of U_I and solving for U_0 or U_I respectively, the solution is obtained. The process of solving the exact general Riemann problem is described in detail in many text books, for example Toro [2].

$$\rho_I u_I = \rho_0 S \tag{3}$$

$$\rho_I u_I^2 + p_I = \rho_0 u_0^2 + p_0 \tag{4}$$

$$\frac{\gamma_I}{\gamma_I - 1}\frac{p_I}{\rho_I} + \frac{1}{2}u_I^2 = \frac{\gamma_0}{\gamma_0 - 1}\frac{p_0}{\rho_0} + \frac{1}{2}u_0^2 + q \tag{5}$$

Comments on the thin flame Riemann solver by Teng et.al.

In this chapter the Riemann solver for reactive gas by Teng et.al [1] will be discussed with corrections. The discussion of the wave patterns in the phase plane in turbulent combustion in Teng et.al. is further discussed here as the waves in the deflagration solution is calculated incorrectly. The paper reports that this model might produce two or zero solutions. The derivation of the Riemann solver is written here for this discussion. The stationary conservation equations of mass, momentum and energy are basis for the Riemann solver, the reaction zone is assumed to be infinitely thin and all the heat from the reaction is released instantaneously. If we let V be the flame speed, the velocity of the reaction zone relative to a fixed referance frame, then

$$w_0 = u_0 - V, \quad w_1 = u_1 - V \tag{6}$$

Where subscript 0 referes to the unburned state and 1 to the burned state. Conservation of mass and momentum is then expressed as

$$\rho_1 w_1 = \rho_0 w_0 = -M \tag{7}$$

$$\rho_1 w_1^2 + p_1 = \rho_0 w_0^2 + p_0 \tag{8}$$

For simplicity the heat capacity ratio γ is assumed identical for the burned and unburned gas and the energy conservation equation is expressed by

$$p_0(\tau_0 - \mu^2\tau_1) - p_1(\tau_1 - \mu^2\tau_0) - 2\mu^2\Delta = 0 \tag{9}$$

$$\tau = \frac{1}{\rho} \tag{10}$$

$$\mu = \frac{\gamma - 1}{\gamma + 1} \tag{11}$$

Δ is the specific energy released by the reaction and is defined with a negative value for an exothermal reaction. From the conservation equations of mass and momentum we can derive the pressure-velocity relations

$$M = \frac{p_1 - p_0}{u_1 - u_0}, \quad M^2 = \frac{p_0 - p_1}{\tau_1 - \tau_0} \tag{12}$$

With the energy equation and the two pressure-velocity relations we can eliminate the mass flow and the density of the burned gas.

$$\frac{p_1 - p_0}{u_1 - u_0} = \sqrt{\frac{p_0\rho_0\left(\frac{\gamma-1}{2} + \frac{(\gamma+1)p_1}{2p_0}\right)}{1 + \frac{(\gamma-1)\rho_0\Delta}{p_1 - p_0}}} \tag{13}$$

An expression for the velocity in the burned state as a function of only the unburned state and the pressure in the burned state can be derived.

$$u_1 = u_0 + (p_1 - p_0)\sqrt{\frac{(1-\mu^2)\tau_0 - \frac{2\mu^2\Delta}{p_0 - p_1}}{\mu^2 p_0 + p_1}} \tag{14}$$

Chapman-Jouguet waves

A CJ-wave moves with the speed of sound with respect to the burned gas. With this information a pressure/density relation for the states on both sides of the CJ wave can be derived.

$$-(\rho_1 c_1)^2 = \frac{p_1 - p_0}{\tau_1 - \tau_0} \tag{15}$$

the soundspeed is defined as $c_1 = \sqrt{\gamma \frac{p_1}{\rho_1}}$

$$\frac{p_1 - p_0}{\tau_1 - \tau_0} = -\rho_1 \gamma \frac{p_1}{\rho_1} = -\frac{\gamma p_1}{\rho_1} \tag{16}$$

or, by solving for τ_1

$$\tau_1 = \frac{\gamma \tau_0 p_1}{p_1(1+\gamma) - p_0} \tag{17}$$

Changing the subscript 1 to CJ we get an expression for p_{CJ} from the energy equation and the expression for τ_{CJ}

$$p_{CJ}^2 + 2ap_{CJ} + b = 0 \tag{18}$$

$$a = -p_0 + \Delta(\gamma - 1)\rho_0 \tag{19}$$

$$b = p_0^2 - 2\mu^2 \rho_0 p_0 \Delta \tag{20}$$

solving this second order equation yields

$$p_{CJ} = p_0 - (\gamma - 1)\rho_0 \Delta \left(1 \pm \sqrt{1 - \frac{2\gamma p_0}{(\gamma^2 - 1)\rho_0 \Delta}}\right) \tag{21}$$

the pluss sign corresponds to the CJ-detonation and the minus sign corresponds to the CJ-deflagration.

$$u_{CJ} = u_0 + (p_{CJ} - p_0)\sqrt{\frac{(1-\mu^2)\tau_0 - \frac{2\mu^2 \Delta}{p_0 - p_{CJ}}}{\mu^2 p_0 + p_{CJ}}} \tag{22}$$

$$\tau_{CJ} = \frac{\gamma \tau_0 p_{CJ}}{p_{CJ}(1+\gamma) - p_0} \tag{23}$$

The speed of the CJ-wave is determined from the conservation of mass and the equations for the CJ state.

$$V_{CJ} = u_0 + \frac{c_0^2}{\sqrt{-\frac{(\gamma^2-1)\Delta}{2} + c_0^2} \pm \sqrt{-\frac{(\gamma^2-1)\Delta}{2}}} \tag{24}$$

Here the pluss sign corresponds to the deflagration state and the minus sign corresponds to the detonation state.

Deflagrations

If we look at the deflagration wave and use a model for the flame speed

$$V = u_0 + K\left(\frac{p_0}{\rho_0}\right)^Q, \quad K, Q \ \textit{constants} \tag{25}$$

Q=$\frac{1}{2}$ for the laminar burning velocity and Q>$\frac{1}{2}$ for turbulent burning velocity. The burning velocity $(V - u_0)$ must be less than or equal to the CJ-deflagration velocity.

$$K\left(\frac{p_0}{\rho_0}\right)^Q \leq \frac{c_0^2}{\sqrt{-\frac{(\gamma^2-1)\Delta}{2} + c_0^2} + \sqrt{-\frac{(\gamma^2-1)\Delta}{2}}} \tag{26}$$

The speed, w of the unburned state 0 is then written as

$$w_0 = -K\left(\frac{p_0}{\rho_0}\right)^Q \tag{27}$$

From the general Riemann solver the U_0 and U_R states are connected by a right wave if

$$\phi(p_0; p_R, \rho_R) = \begin{cases} (p_0 - p_R)\sqrt{\frac{(1-\mu^2)\tau_R}{p_0+\mu^2 p_R}} & p_0 \geq p_R \\ \frac{\sqrt{(1-\mu^2)\tau_R p_R}}{\mu^2}\left(p_0^{\frac{\gamma-1}{2\gamma}} - p_R^{\frac{\gamma-1}{2\gamma}}\right) & p_0 < p_R \end{cases} \tag{28}$$

$$u_0 = u_R + \phi(p_0; p_R, \rho_R) \tag{29}$$

We now need an expression that connect unburned and the burned state by a deflagration wave, eleminating w_1 and ρ_1 form the conservation equations we get an expression for massflow.

$$\rho_0 w_0 = -\sqrt{\frac{\mu^2 p_0 + p_1}{(1-\mu^2)\tau_0 - \frac{2\mu^2\Delta}{p_0 - p_1}}} \tag{30}$$

solving for p_1 with $M_0 = -\frac{w_0}{c_0} = \frac{K\left(\frac{p_0}{\rho_0}\right)^Q}{\left(\gamma\frac{p_0}{\rho_0}\right)^{0.5}} = \frac{K}{\gamma^{0.5}}\left(\frac{p_0}{\rho_0}\right)^{Q-0.5}$ being the Mach number of the reaction zone relative to the unburned state.

$$p_1 = p_0\left(\frac{1}{2}(1-\mu^2)(1+\gamma M_0^2) + \frac{1}{2}\sqrt{(1+\mu^2)(1-M_0^2) + 8\mu^2\gamma^2 M_0^2\frac{\Delta}{c_0^2}}\right) \tag{31}$$

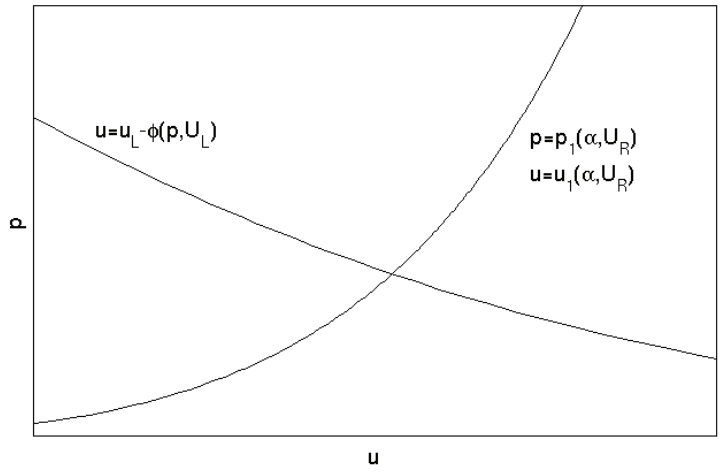

Figure 2: Hugoniot locus with Q=2.

The states U_L and U_1 are connected by a left wave in the same manner as U_0 and U_R. The intersection of the curves $U = U(U_L)$ and $U = U(U_R)$ in state space, called a Hugoniot locus, is the solution of the Riemann problem. Figure 2 shows the Hugoniot locus with an example of a turbulent flame with Q=2.

One way of getting several solutions, or none, is to use a positve Δ in the CJ deflagration velocity expression. The Mach number of the flame with respect to the unburned gas will then become imaginary while the square of the Mach number becomes real. This can be the reason for the non monotonic behaviour of the waves in the p,u plane presented in the article. An example of a solution in state space with turbulent deflagration and a positive Δ is shown in figure 3. When the CJ deflagration velocity is reached, the curve becomes non-monotonic and two solutions are obtained.

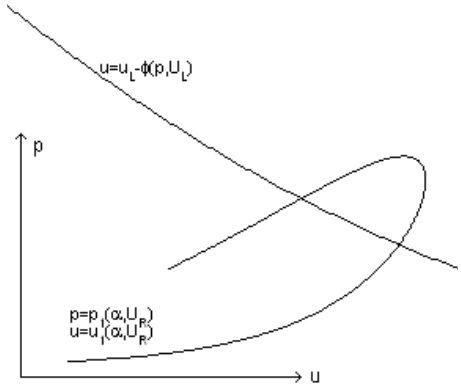

Figure 3: Hugoniot locus with Q=2 and Δ is positive.

Bibliography

[1] Teng, T. H., Chorin, A. J., Liu, T. P. *Riemann problems for reacting gas, with applications to transition* SIAM J. Appl. Math. 42 (5), 1982.

[2] Toro, E. F., *Riemann Solvers and Numerical Methods for Fluid Dynamics: A Practical Introduction, Berlin, Heidelberg, Germany, Springer-Verlag, 1999.*

Appendix C

List of papers

Papers with Knut Vaagsaether as first author and co-author.

For all papers with K. Vaagsaether as first author Knut Vaagsaether did all of the model development and solver implementation.

- K. Vaagsaether, D. Bjerketvedt, *Simulation of supersonic shear layers with high resolution TVD methods*, Fourth International Conference on Computational Fluid Dynamics in the Oil and Gas, Metallurgical & Process Industries, Trondheim SINTIF/NTNU Norway 2005.
  Knut Vaagsaether did all simulations and wrote the paper.

- K. Vaagsaether, D. Bjerketvedt, *Gas explosion simulation with Flux Limiter Centred method*, 20nd ICDERS, 2005, Montreal, Canada.
  Knut Vaagsaether did all simulations and wrote the paper, in addition did the experiments with V. Knudsen.

- K. Vaagsaether, V. Knudsen and D. Bjerketvedt, *Simulation of flame acceleration and DDT in H_2-air mixtures with a flux limiter centered method*, First International Conference on Hydrogen Safety, 2005, Pisa, Italy.
  Knut Vaagsaether did all simulations and wrote the paper, in addition did the experiments with V. Knudsen.

- K. Vaagsaether, V. Knudsen, D. Bjerketvedt, *Simulation of flame acceleration and DDT in H2-air mixture with a flux limiter centered method*, International Journal of Hydrogen Energy 32, (2007), 2186–2191. Knut Vaagsaether did all simulations and wrote the paper, in addition did the experiments with V. Knudsen.

- K. Vaagsaether, D. Bjerketvedt, *Simulation of flame acceleration in an obstructed tube with LES*, 21st ICDERS, 2007, Poitiers, France.
  Knut Vaagsaether did all simulations and wrote the paper, in addition did the experiments with V. Knudsen.

- K. Vaagsaether, S. O. Christensen, D. Bjerketvedt, *Modeling and image analysis of FAE*, MABS 20, 2008, Oslo, Norway.
  Knut Vaagsaether did all simulations and wrote the paper.

- K. Vaagsaether, D. Bjerketvedt, *Simulation of FA and DDT in a channel with repeated obstacles with an under-resolved mesh*, 22nd ICDERS, 2009, Minsk, Belarus.
  Knut Vaagsaether did all simulations and wrote the paper.

- K. Kristoffersen, K. Vaagsaether, D. Bjerketvedt, G. O. Thomas, *Propane-air pipe explosion experiments. Data for estimation of 1-D burning velocity in slow regimes*, Experimental Thermal and Fluid Science, 28 (7), 2004, 723-728.
  Knut Vaagsaether did the experiments with Kjetil Kristoffersen.

- D. Bjerketvedt, K. Kristoffersen, K. Vaagsaether, A. Mjaavatten , G. O. Thomas, *A method for estimating the burning velocity in a tube by using experimental pressure records and the one-dimensional RCMLab code*, Combustion Science and Technology, 176 (10), 2004, 1725-1734.
  Knut Vaagsaether did the experiments with Kjetil Kristoffersen, and was part of the discussion on the methodology.

- V. Knudsen, K. Vaagsaether and D. Bjerketvedt, *Experiments with hydrogen-air explosions in a closed pipe with a single obstacle*, Proc. of the European Combustion Meeting, 2005.
  Knut Vaagsaether did the experiments with Vegeir Knudsen.

- V. Knudsen, K. Vaagsaether and D. Bjerketvedt, *An experimental study of hydrogen-air gas explosions in a single obstructed pipe*, Proc. of the First Baltic Combustion Meeting, 2005.
  Knut Vaagsaether did the experiments with Vegeir Knudsen.

- O. K. Sommersel, D. Bjerketvedt, S. O. Christensen, O. Krest, K. Vaagsaether, *Application of background oriented schlieren (BOS) for quantitative measurements of shock waves from explosions*, , 21st ICDERS,

2007, Poitiers, France.
Knut Vaagsaether was part of the discussion on the technique used in the paper.

- O. K. Sommersel, D. Bjerketvedt, K. Vaagsaether, T. K. Fannelop, *Experiments with release and ignition of hydrogen gas in a 3 m long channel*, International Journal of Hydrogen Energy, 34(14),2009, 5869–5874.
  Knut Vaagsaether was part of the discussion on the scaling laws.